

JUSTUS-LIEBIG-UNIVERSITÄT GIESSEN

**Investigation of the Collective Behavior of  
Nuclei Around Mass 70 Towards the Proton  
Drip-line**



**Tuğba Arıcı**

Fachbereich 07 - Mathematik und Informatik, Physik, Geographie

II. Physikalisches Institut Justus-Liebig-Universität Gießen

Gießen 2017



**JUSTUS-LIEBIG-UNIVERSITÄT GIESSEN**

# **Investigation of the Collective Behaviour of Nuclei Around Mass 70 Towards the Proton Drip-line**

Inauguraldissertation zur Erlangung des Doktorgrades der  
Naturwissenschaftlichen Fakultät der Justus-Liebig-Universität Gießen

vorgelegt von

**Tuğba Arıcı**

geboren am 01 November 1988  
in Fethiye, Türkei

Fachbereich 07 - Mathematik und Informatik, Physik, Geographie

II. Physikalisches Institut Justus-Liebig-Universität Gießen

Gießen 2017



## Selbstständigkeitserklärung

Ich erkläre: Ich habe die vorgelegte Dissertation selbständig und ohne unerlaubte fremde Hilfe und nur mit den Hilfen angefertigt, die ich in der Dissertation angegeben habe. Alle Textstellen, die wörtlich oder sinngemäß aus veröffentlichten Schriften entnommen sind, und alle Angaben, die auf mündlichen Auskünften beruhen, sind als solche kenntlich gemacht. Bei den von mir durchgeführten und in der Dissertation erwähnten Untersuchungen habe ich die Grundsätze guter wissenschaftlicher Praxis, wie sie in der „Satzung der Justus-Liebig-Universität Gießen zur Sicherung guter wissenschaftlicher Praxis“ niedergelegt sind, eingehalten.

---

Datum

---

Tugba Arici



**Erstgutachter:** Prof. Dr. Christoph Scheidenberger

**Zweitgutachter:** Prof. Dr. Dr h.c. Hans Geissel

**Prüfer:** Prof. Dr. Horst Lenske

**Prüfer:** Prof. Dr. Wolfram Korten



# Acknowledgment

With the end of my PhD, a very valuable phase of my life comes to a conclusion. I appreciate the time that I spent with everybody that I met in this period, since they all contributed in different ways to enrich my experiences in work and in life. Here, I would like to mention the people who generously gave me their personal or professional support, after I started my PhD.

I would like to express my gratitude to my Promoter, Prof. Dr. Christoph Scheidenberger for his constant support and advice. I really appreciate his guidance and friendly help during this period. I am also grateful to Prof. Dr. Dr. h.c. Hans Geissel for his assistance, enlightening discussions and insightful questions that makes one think in different ways.

I would like to express my gratitude to Ivan Kojouharov for giving a unique chance to work together. He shared his proficiency and knowledge, literally on everything. His practical intelligence and enthusiasm for his expertise always motivated me and helped me to increase my knowledge and technical skills in the field of detector systems and electronics.

Then, I would like to thank the second person whom I met during my studies, Dr. Jürgen Gerl, the most polite person in the world, who supervised, took care and supported me from various aspects. I appreciate the opportunity that he gave to me for my PhD and additionally I have to mention how efficient he is, always has very bright ideas about work and sharing his thoughts, regardless of how busy he is, with never ending kindness.

I owe a huge debt of gratitude to Dr. Kathrin Wimmer for her supervision during my PhD. She was there with endless help for the analysis process and provided valuable suggestions. I valued her presence, especially during the period that I was writing this thesis with her ever-honest, extremely nice and very creative comments. Her willingness to read the manuscript and give corrections while not letting it to be a tedious process is highly appreciated, she even introduced me to very nice songs that I did not hear before, even if I was living them :)

I am very grateful to Dr. Wolfram Korten for creating the opportunity to study a very interesting physics case. It was always a pleasure to have physics discussions with him and I qualify the time that I spent with him as a luxury because of all the guidance and support he gave.

I collaborated with different working groups around the world and always benefited from the exchange of ideas. Here I would like to thank the RIKEN crew for the cooperation and hospitality offered by them, especially Dr. Pieter Doornenbal who worked with a great commitment on the preparation of the experiments and also for his support during the analysis.

I am very grateful to the members of the Gamma Spectroscopy group, Cesar, Henning, Jelena, Magda, Michael, Sudipta and Tobias for all the things that we shared inside or outside the workplace. It was sometimes stressful, sometimes joyful, but it was always a very precious time that we spent together.

I am extremely thankful for the friendship and the endless support of Sivajim. Many thanks are also to many colleagues and friends in Germany. I came across and met many wonderful people during my time at GSI. Far too many people to mention individually; but my sincere gratitude to them all, especially to my physics discussion crew.

I want to offer special gratitude to Jaap, who even though occupied with his own work, was always there with unwavering patience, support, and understanding.

These acknowledgments would not be complete without thanking my family for their support throughout all these years. I thank my father Durmuş Yaşar, my mother Fatma, my sisters Aysegül, Yelda and brother Hüseyin for always standing by me. Their everlasting encouragement, love and unconditional support helped me to see it calmly through to the end.

Gießen, July 2017

# Abstract

In even-even nuclei, deformation of the nucleus is related to reduced transition probability,  $B(E2)$  values. By measuring the  $2^+$  states and corresponding  $B(E2)$  values, collectivity can be studied in a unique way. In order to obtain these values, intermediate energy exotic beams have been used as a spectroscopic tool through Coulomb excitations and nuclear inelastic scatterings. The inelastic scattering of  $^{72}\text{Kr}$ ,  $^{70}\text{Kr}$ ,  $^{70}\text{Br}$  and  $^{68}\text{Se}$  isotopes on  $^9\text{Be}$  and  $^{197}\text{Au}$  targets has been performed. Production of these very exotic nuclei, at the proton drip-line, was achieved at the Radioactive Isotope Beam Factory (RIBF), Japan [1]. A  $^{78}\text{Kr}$  primary beam with an energy of  $345\text{ MeV}/u$  was impinged on a  $^9\text{Be}$  target to produce the ions of interest as a secondary beam. The BigRIPS fragment separator was used in order to deliver the secondary beam isotopes with an energy of  $175\text{ MeV}/u$  to the secondary target. The reaction products were identified in the ZeroDegree Spectrometer (ZDS) employing the  $B\rho\text{-}\Delta E\text{-}ToF$  method. The  $\gamma$ -rays emitted due to the excitation were measured by an array of  $\gamma$ -ray detectors, DALI2, that was placed around the secondary target [2].

The experiments were performed using two different targets in order to increase the probability of Coulomb or nuclear interaction. While the exotic beam at intermediate energies scatters through the electromagnetic field of an Au target, Coulomb and nuclear forces interfere. The fraction of these two kinds of excitation was identified by scattering the same beam off a Be target and increase the relative strength of nuclear scattering. For each isotope, the experimental conditions were simulated to obtain the response functions of the transitions. Experimental results were then fitted to these response functions from the simulations in order to determine the number of emitted  $\gamma$ -rays. Then, the excitation cross-sections were deduced for both cases and used in order to determine the deformation lengths  $\delta_n$  and  $\delta_c$ , for nuclear and Coulomb excitation, respectively. These deformation lengths were obtained using ECIS-97 code [3]. Finally, using the relation between electromagnetic interaction deformation length and the deformation parameter,  $B(E2)$  values were determined.



# Zusammenfassung

Die Deformation von Atomkernen wirkt sich auf die reduzierten Übergangswahrscheinlichkeiten, die  $B(E2)$  Werte aus. Durch Messung der ersten angeregten  $2^+$  Zustände und entsprechender  $B(E2)$  Werte kann so die Kollektivität in einzigartiger Weise untersucht werden. Um diese Werte zu erhalten, wurden exotische Strahlen mittlerer Energie als spektroskopisches Werkzeug mittels Coulomb-Anregung und inelastischer Kernstreuung genutzt. Hierzu wurden  $^9\text{Be}$  und  $^{197}\text{Au}$  targets mit  $^{72}\text{Kr}$ ,  $^{70}\text{Kr}$ ,  $^{70}\text{Br}$  und  $^{68}\text{Se}$  bombardiert. Die Herstellung dieser sehr exotischen Kerne, nahe der Protonenabbruchkante, wurde an der Radioactive Isotope Beam Factory (RIBF) in RIKEN, Japan durchgeführt [1]. Ein  $^{78}\text{Kr}$  Primärstrahl mit einer Energie von  $345\text{ MeV}/u$  wurde, um die gewünschten Ionen als Sekundärstrahl zu produzieren, auf ein  $^9\text{Be}$ -Target geschossen. Der BigRIPS Fragmentseparator wurde genutzt, um die gewünschten Sekundärstrahl-Isotope mit einer Energie von  $175\text{ MeV}/u$  am Sekundär-Target zu erhalten. Die Reaktionsprodukte wurden unter Verwendung des  $B\rho$ - $\Delta E$ - $ToF$  Verfahrens im ZeroDegree Spektrometer (ZDS) identifiziert, Die nach der Sekundär-Anregung emittierten  $\gamma$ -Quanten wurden in einem um das Sekundär-Target angeordneten Aufbau von  $\gamma$ -Strahlungsdetektoren gemessen, DALI2 [2].

Bei der Wechselwirkung der beschleunigten Ionen mittlerer Energie mit den Kernen des schweren Targets überlagern sich Coulomb- und Kernkräfte. Um diese beiden Komponenten unterscheiden zu können, wurden die Experimente mit zwei verschiedenen Targets durchgeführt. Die Streuung des Strahls an einem Beryllium-Target erhöht den relativen Teil an Kernstreuung, während bei dem Gold-Target der Coulomb Anteil dominiert. Das Verhältnis dieser zwei Arten der Anregung wurde ermittelt. Für jedes Isotop wurden die experimentellen Bedingungen simuliert, um die Antwortfunktion der Übergänge zu erhalten. Experimentelle Ergebnisse wurden dann zu diesen simulierten Antwortfunktionen hinzugefügt, um die Anzahl der abgestrahlten  $\gamma$ -Quanten zu ermitteln. Dann wurde auf die Anregungswirkungsquerschnitte für beide Fälle rückgeschlossen und diese dazu verwendet, die Deformationslängen  $\delta_n$  und  $\delta_c$  zu bestimmen, für sowohl Kern- als auch Coulomb-Anregung. Diese Deformationslängen wurden unter Verwendung des ECIS-97 Codes erhalten [3]. Schließlich wurden unter Verwendung der elektromagnetischen Wechselwirkungsdeformationslänge und der Deformationsparameter die  $B(E2)$  Werte ermittelt.



# Contents

<b>1</b>	<b>Introduction</b>	<b>1</b>
1.1	Systematics in the Mass Number 70 Region . . . . .	3
1.1.1	Krypton Isotopic Chain . . . . .	3
1.1.2	T=1 Triplet at A=70 . . . . .	7
<b>2</b>	<b>Nuclear Structure</b>	<b>9</b>
2.1	Nuclear Models . . . . .	10
2.1.1	Liquid Drop Model . . . . .	11
2.1.2	Shell Model . . . . .	11
2.1.3	Nuclear Shapes and Deformation . . . . .	13
2.1.4	The Nilsson Model . . . . .	14
2.1.5	Modern Theoretical Approaches . . . . .	15
2.2	Symmetry . . . . .	16
2.2.1	Isospin . . . . .	17
2.2.2	Energy Differences in Isobaric Multiplets . . . . .	18
2.3	Experimental Technique . . . . .	19
2.3.1	Coulomb Excitation Theory . . . . .	19
2.3.2	Nuclear Inelastic Scattering . . . . .	23
2.3.3	The Optical Model . . . . .	24
2.3.4	Gamma Decay . . . . .	26
2.3.5	Collectivity Quantities . . . . .	27
<b>3</b>	<b>Experimental Setup</b>	<b>29</b>
3.1	Radioactive Ion Beams . . . . .	29
3.1.1	Production of RI Beams at RIKEN . . . . .	30
3.1.2	Separation and Identification of the RI Beams . . . . .	30
3.1.3	BigRIPS Fragment Separator . . . . .	31
3.1.4	ZeroDegree Spectrometer . . . . .	33
3.2	Beam Line Detectors . . . . .	33
3.2.1	Parallel Plate Avalanche Counters . . . . .	33
3.2.2	Plastic Scintillation Detectors . . . . .	34
3.2.3	Ionization Chamber . . . . .	35

---

3.3	Gamma Spectroscopy . . . . .	36
3.3.1	In-Beam Gamma Spectroscopy . . . . .	36
3.3.2	DALI2 Gamma Detector Array . . . . .	37
3.4	Performed Experiments . . . . .	39
3.4.1	Trigger Configuration . . . . .	41
3.5	Monte Carlo Simulations . . . . .	41
<b>4</b>	<b>Data Analysis</b>	<b>45</b>
4.1	Particle Identification . . . . .	45
4.1.1	Position Determination . . . . .	46
4.1.2	ToF Measurement . . . . .	47
4.1.3	Atomic Number Determination . . . . .	49
4.1.4	Particle IDentification (PID) of Ions . . . . .	50
4.2	Scattering Angle Determination . . . . .	55
4.3	Particle Transmission through the Spectrometer . . . . .	59
4.4	Velocity Determination of the Particles . . . . .	62
4.5	The Analysis of the Emitted Gamma-Rays . . . . .	63
4.5.1	Energy Calibration . . . . .	63
4.5.2	Full Energy Peak Efficiency . . . . .	66
4.5.3	Doppler Shift Correction . . . . .	71
4.5.4	Time Calibration of the DALI2 Array . . . . .	72
<b>5</b>	<b>Results</b>	<b>75</b>
5.1	Reaction Channels . . . . .	76
5.1.1	Observed Excited States of $^{72}\text{Kr}$ . . . . .	76
5.1.2	Observed Excited States of $^{70}\text{Kr}$ . . . . .	80
5.1.3	Observed Excited States in $^{70}\text{Br}$ . . . . .	80
5.1.4	Observed Excited States of $^{68}\text{Se}$ . . . . .	82
5.2	Measured Cross-Sections . . . . .	87
5.3	Deformation Lengths for Nuclear and Electromagnetic Contributions . . . . .	88
5.3.1	B(E2) Value Determination . . . . .	91
5.4	Discussion . . . . .	93
5.4.1	Theoretical Predictions for the Kr Isotopes . . . . .	93
5.4.2	Collectivity in the A = 70 Isobaric Triplet . . . . .	95
<b>6</b>	<b>Summary and Outlook</b>	<b>101</b>
<b>A</b>	<b>Appendix</b>	<b>105</b>
	List of Figures	107
	List of Tables	109
	References	111

# 1

# Introduction

The use of Radioactive Ion Beam (RIB) enables exploration of large areas and even the limits of the nuclear landscape. These beams provide experimental access to the properties, structure, and dynamics of exotic nuclei and enrich the development of nuclear models. Today, there are many experimental techniques to study different aspects of the nuclear structure involving a wide variety of radiation detection methods. In-beam  $\gamma$ -ray spectroscopy is one of these techniques whereby the nucleus becomes energetically excited via a chosen reaction leading to the excited states in the nucleus of interest. The  $\gamma$ -rays emitted from these excited states are used for the understanding of structure, composition and interactions between the constituents of the nucleus.

The present thesis focuses on the study of nuclei around the  $A = 70$  mass region along the  $N = Z$  line. In  $N = Z$  nuclei, neutrons and protons occupy the same orbitals. This offers an opportunity to study the effect of the nucleon sequence on deformation and shape changing effects caused by proton-neutron correlations. Moreover, in the region towards the proton drip line, nuclei experience a low binding energy which results in a shape change and in the vicinity of  $N = Z$ , around  $A = 70$  this occurs even more rapidly, where the valence nucleons occupy the  $fp$  orbitals. According to shell model calculations, the occupation of the  $fp_{9/2}$  orbital plays an important role on the increasing collectivity at this mid-shell region [4], where many nucleons may contribute to the behavior of the nucleus. In the Nilsson diagram, the sharp down-sloping part of this orbital with increasing deformation, illustrates this behavior as favoring deformed shapes by lowering the energy as shown in Figure 2.3. These intruder orbitals in the region are expected to be one of the mechanisms behind the existence of shape co-existence as well as rapid shape changes for nucleon numbers 34, 36 and 38. Within the content of this thesis, the  $^{70}\text{Kr}$ ,  $^{72}\text{Kr}$ ,  $^{70}\text{Br}$  and  $^{68}\text{Se}$  isotopes of this region were studied, where the valence protons and neutrons occupy these shells and allow to address fundamental questions of nuclear structure physics, such as the charge symmetry, independence of nuclear force and collectivity. In order to determine the collectivity, the reduced transition probabilities,  $B(E2)$  values, have to be determined. The reduced transition probability of an even-even nucleus with  $A$  and  $Z$  mass and charge numbers respectively, relates to the

magnitude of the deformation of the given nucleus via following relation:

$$\beta = \frac{4\pi}{3ZR_0^2} \sqrt{B(E2 \uparrow) / e^2} \quad (1.1)$$

where  $R_0$  has been taken as  $1.2A^{1/3} \text{ fm}$ . The  $B(E2)$  values between the ground state and excited  $2^+$  state is a good indicator to identify the collectivity as well as the type of the deformation in nuclei. These  $B(E2)$  values can be determined with techniques called Coulomb excitation, lifetime measurements or resonance fluorescence. We used the Coulomb excitation method that is particularly sensitive to charge distribution of the nucleus and is therefore very well suited for the investigation of different aspects of nuclear collectivity.

In Coulomb excitation, a nucleus gets excited to higher energy levels by interacting with the electromagnetic field of another nucleus at Coulomb barrier energies. Studies of these nuclear, excited states give information about the nature of nuclei and the cross section of the excitation is used to deduce the reduced transition probabilities. However, with current facilities, exotic nuclei close to the proton drip line such as  $^{70}\text{Kr}$  are not possible to produce at Coulomb barrier energies of a few  $\text{MeV}/u$ . Therefore, Coulomb excitation at intermediate energies (around few hundred  $\text{MeV}$ ) was performed. In order to achieve a significant cross section, the electrical potential needs to be high, such that targets with high  $Z$ , like gold or lead are preferred. These conditions are explained in section 2.3.1 in detail by indicating the difference between Coulomb excitation at low and intermediate energy.

Within the content of this thesis, the relativistic Coulomb excitation of nuclei around the  $A = 70$  mass region along the  $N = Z$  line were studied to measure the reduced transition probabilities. Due to the possible interference of nuclear and electromagnetic excitations at these energies, the nuclear inelastic scattering process was created in the same experimental conditions using a light Be target as a secondary target instead of a heavy Au target in order to increase the probability of the nuclear interaction. The fraction of these two excitation mechanisms has to be disentangled. With this additional step, the relative strength of nuclear scattering is enhanced so that the deformation length on the nuclear interaction  $\delta_n$  can be determined by using experimentally measured excitation cross-sections; this is accomplished using the coupled-channel ECIS-97 code, and the  $\delta_n$  value is then used to extract the Coulomb deformation length  $\delta_c$ . Using the relation between deformation lengths and the deformation parameter, results for the reduced transition probability  $B(E2; 0^+ \rightarrow 2^+)$  for  $^{70}\text{Kr}$  and neighboring isotopes can be calculated from equation 1.1.

The Coulomb excitation of  $^{70}\text{Kr}$  was performed for the first time, results for the reduced transition probability  $B(E2; 0^+ \rightarrow 2^+)$  for  $^{70}\text{Kr}$  and neighboring isotopes are presented. Several experiments have been attempted in the past to investigate the structure of Kr isotopes beyond the  $N = Z$  line, but no spectroscopic information was available so far for  $^{70}\text{Kr}$ . The chain for the experimental knowledge of Kr isotopes was extended with this study and compared with theoretical calculations. Additionally,  $^{72}\text{Kr}$ ,  $^{70}\text{Br}$  and  $^{68}\text{Se}$ , the

$N = Z$  isotopes in the region were studied in the same way and compared.

Furthermore, measuring  $^{70}\text{Kr}$  enabled study of the  $A = 70$   $T = 1$  triplet. Rapid shape changes and the expected strong mixing of oblate and prolate shapes are found to be an interesting territory to study isospin breaking effects as well. The  $^{70}\text{Se}$  and  $^{70}\text{Br}$  isotopes are the other two members of a triplet with  $^{70}\text{Kr}$ . Previously, observed negative tendency with increasing spin in Coulomb Energy Differences (CED) attracted an interest to study these Isobaric Analogue States (IAS). By measuring the third member of this triplet, we enabled the study of Mirror Energy Differences (MED) and Triple Energy Differences (TED) that can provide information about charge symmetry, charge independence and isospin symmetry breaking which gives important new information about the shape coexistence phenomenon (the existence of two shapes at the same excitation energies) across the  $N = Z$  line.

## 1.1 Systematics in the Mass Number 70 Region

The mass region around  $A = 70$  at the proton-rich side of the nuclear chart is interesting as it enables the study of the evolution of nuclear shapes for nuclei with a similar proton and neutron number, since adding or removing only a few nucleons may have a dramatic effect on the type of nuclear deformation. The type of the deformation is determined via  $Q$  quadrupole moments or the  $\beta$  deformation parameter.

Most of the deformed nuclei are prolate shaped ( $\beta > 0$ ,  $Q < 0$ ), while the observation of oblate ( $\beta < 0$ ,  $Q > 0$ ) shapes as ground state deformation is extremely rare. One region, where oblate deformation has been experimentally established for the ground state shape, is the  $A = 70$  region [5, 6, 7, 8]. The existence of oblate ground state deformation makes  $A = 70$  region very special to study. This unique feature can be related to the effective nuclear forces in the relevant nuclei that is not completely understood from different aspects. The energy gained by deformation can be associated with a lowering of the kinetic energy by the establishment of an isotropic momentum distribution. The states with maximum deformation in accordance with the Pauli principle, have the lowest kinetic energies. As a consequence, prolate shapes dominate over oblate shapes [9].

The measurements on  $^{70}\text{Kr}$  carries important information due to the observed and predicted shape transitions in the region. It can be studied from two different perspectives as, a member of Kr isotropic chain and the member of isobaric analog states. In the following subsections, these aspects are discussed and explained.

### 1.1.1 Krypton Isotopic Chain

It is important to review the properties and the shape transitions of Kr isotopes since we are extending the knowledge along their chain from the less to the more exotic member  $^{70}\text{Kr}$  member. As shape changes are expected in this region by adding only a few neutrons or protons along the isotonic or isotopic chains, observed and predicted shape

transitions in Kr chain have been attracting the interest of many experimental and theoretical physicist over years [10, 11, 12, 13]. The overview of some experimental results obtained up to date for the Kr chain is given this section in order to describe the features of this chain. Results are consistent with each other and also with various theoretical calculations.

The investigation of this unique behavior in the area is started with the  $^{74}\text{Kr}$  isotope and followed by  $^{76}\text{Kr}$  and  $^{72}\text{Kr}$ . The experimentally determined quadrupole moments that indicate the shape and the  $B(E2)\uparrow$  values as a measure of collectivity are given in Table 1.1 for  $^{72-78}\text{Kr}$ .

**Table 1.1:** The measured spectroscopic quadrupole moments ( $Q_s$ ) that define the shape of the nuclei ( $Q_s < 0$  prolate,  $Q_s > 0$  oblate) and the  $B(E2)\uparrow$  values as a measure of the collectivity for  $^{72,74,76,78}\text{Kr}$  isotopes are given in the table. The values are adapted from reference [5, 14, 15].

$0^+ \rightarrow 2^+$	$^{72}\text{Kr}$	$^{74}\text{Kr}$	$^{76}\text{Kr}$	$^{78}\text{Kr}$
$Q_s$ [eb]	-	-0.5(2)	-0.7(2)	-
$B(E2)$ [ $e^2b^2$ ]	0.4997(65)	0.627(31)	0.758(26)	0.634(16)

The highest collectivity in the measured chain members to date is found to be in the  $^{76}\text{Kr}$  isotope with  $0.758(26) e^2b^2$   $B(E2)\uparrow$  value and it decreases through isotopes with lower and higher neutron numbers. For  $^{74}\text{Kr}$  and  $^{76}\text{Kr}$  isotopes, the spectroscopic quadrupole moments were measured for the states in the ground-state bands and states above the shape isomer, confirming the shape coexistence scenario. The shape for the ground-state band were found to be predominantly prolate, while oblate deformation was observed for the states belonging to the excited  $0^+$  state [14]. Extrapolating the calculations for  $^{72}\text{Kr}$ , inversion of the ground state shape is expected for this  $N=Z$  nuclei. For  $^{72}\text{Kr}$ , the ground-state quadrupole moments are not measured but predicted many times to have an oblate deformation and these predictions are supported with the experimental information [16]. Additionally, the deformation parameter  $\beta_2$  was identified as 0.33(3), suggesting an oblate shape for the ground state, however the deduced size of the quadrupole deformation is model dependent [5]. The  $B(E2:0_{gs}^+ \rightarrow 2_1^+)$  value for  $^{72}\text{Kr}$  was reported as  $4997(647) e^2fm^4$  from a Coulomb excitation experiment and  $4050(150) e^2fm^4$  from a lifetime measurement [5, 7]. This value is determined also within the study of this thesis and reported in Section 5.

The experimentally constructed level scheme of the low-lying states in even-even Kr isotopes from  $A = 78$  to  $A = 72$ , from less exotic to more, is illustrated in Figure 1.1. The most important evidence for shape coexistence is the identification of low-lying excited  $0^+$  states. The transition from the excited  $0^+$  state to  $0^+$  ground-state, occur via internal conversion electron emission and were observed for all the members of this isotopic chain. The existence and the positions of these states along the isotopic chain was interpreted as evidence for a change of the ground state deformation between prolate and oblate. The  $0_1^+$  ground state of  $^{72}\text{Kr}$  isotope is predicted to have an oblate deformation

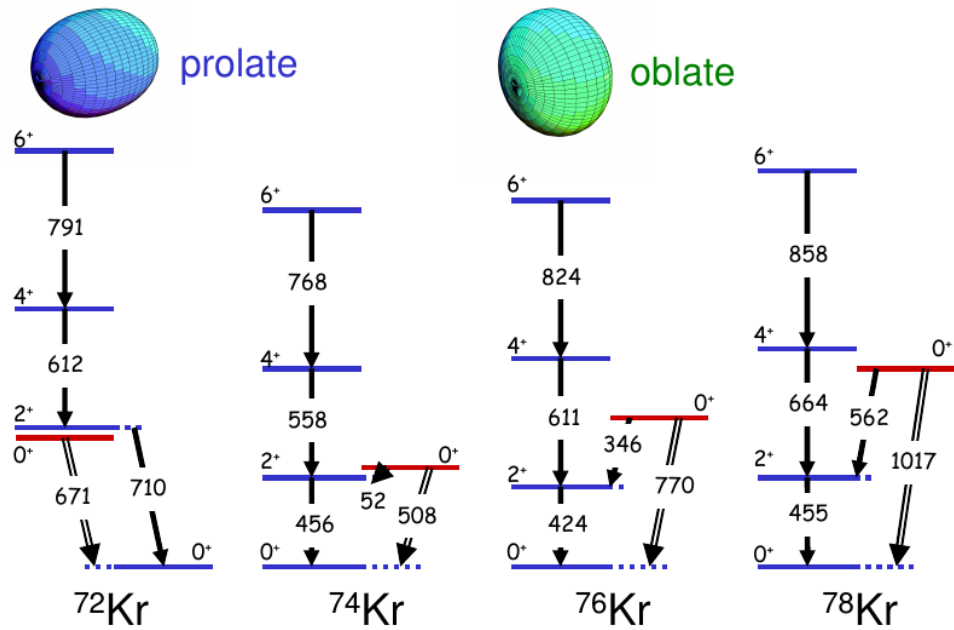


**Figure 1.1:** Systematics of low-lying states in  $^{72}\text{Kr}$ ,  $^{74}\text{Kr}$ ,  $^{76}\text{Kr}$  and  $^{78}\text{Kr}$  indicating the relative positions of  $2^+$  and excited  $0^+$  states. Transitions that occur via internal conversion or electron emission are shown with double arrows. Red lines indicate the  $0_2^+$  excited states and prolate, oblate shape indication on the figure gives their shape [17].

in different theoretical approaches [18]. The  $0_2^+$  was observed at an excitation energy of 671(2) keV and interpreted as the prolate band-head [11]. The energy of the isomeric low-lying  $0_2^+$  state is lower for  $^{74}\text{Kr}$  compared to  $^{72}\text{Kr}$  and it increases again towards the neutron-rich Kr isotopes with higher mass. This study also showed a maximum mixing of oblate and prolate configurations for the ground state of  $^{74}\text{Kr}$ , which also indicates where the predicted shape change starts to turn from oblate to prolate. In addition,  $^{72}\text{Kr}$  isotope is the only isotope in the chain where the  $0_2^+$  state belongs to the same band as the first excited  $2_1^+$  state. At this point, it is important to measure this state also for the  $^{70}\text{Kr}$  to extend the trend of  $0_2^+$  low-lying states.

As mentioned before, various theoretical calculations have been performed for the Kr isotopic chain. One of these models was studied by T. Rodriguez by considering the full chain, in detail, using the Symmetry Conserving Configuration Mixing (SCCM) method. In this model, HFB calculations are used to obtain the Potential Energy Surface (PES) diagrams and the SCCM method to go beyond the mean field and project nuclear states. A detailed description about this work can be found in reference [19]. PES diagrams from this self-consistent beyond mean field calculations are shown in Figure 1.2. A variety of different minima is observed along the chain: spherical, oblate, prolate and oblate-prolate shape-coexistence.  $^{70}\text{Kr}$  was included in this theoretical study which attracts our interest since it is comparing this isotope with other Kr isotopes in the region within the same framework. For  $^{70}\text{Kr}$ , a single minimum is predicted, while for the Kr isotopes with higher mass, two clear minima are observed in the Potential Energy Surface (PES) diagram.

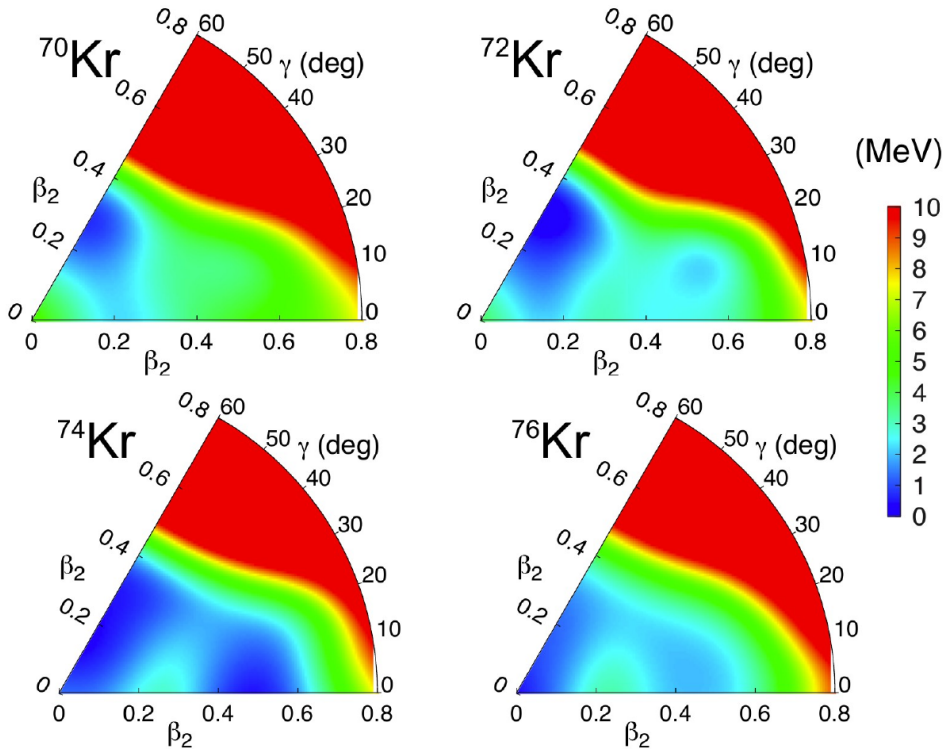


**Figure 1.2:** Potential energy surface in  $(\beta, \gamma)$  plane for  $^{70-76}\text{Kr}$  isotopes.  $\beta$  and  $\gamma$  parameters describe the shape of the nucleus.  $\gamma = 0$  corresponds to prolate deformation and  $\gamma = 60$  gives the oblate deformation [19].

The presence of coexisting states with different deformation at low excitation energy corresponds to several minima in the PES, separated by barriers. For a small barrier, considerable mixing can occur between the coexisting states. According to the PES, this model predicts a spherical and a prolate minimum for  $^{76}\text{Kr}$  and a more prolate and an oblate minimum in  $^{74}\text{Kr}$ . For  $^{72}\text{Kr}$ , the global minimum is oblate indicating a ground state with oblate-prolate transitions due to the second more shallow prolate minimum. For  $^{70}\text{Kr}$ , an oblate ground state is expected with a wave function expanding through low  $\gamma$  angles, with no shape coexistence.

Another theoretical model is the configuration mixing calculations using the Generator Coordinate Method (GCM) with Gaussian Overlap Approximation (GOA), using the Gogny effective interaction as explained in reference [20]. This model suggests shape coexistence for  $^{74,76}\text{Kr}$  isotopes, in the region with a predominantly prolate shape and a strong predominant oblate deformation for the ground state of  $^{72}\text{Kr}$ . However, the referred study does not include  $^{70}\text{Kr}$ . The calculations for this isotope was obtained by private communication and the result will be discussed in Section 5.4.2.

1.1.2  $T=1$  Triplet at  $A=70$ 

This region of the nuclear chart where the valence nucleons occupy the  $fp$ g shell is of interest due to the deformation driving effects and the large shell gaps as explained in Section 2.3 and 2.1.3.  $T=1$  triplet at  $A=70$ , occupying these shells, has attracted strong interest over the years due to the shape coexistence that is expected to be perfect mixing of oblate and prolate shapes [21].  $^{70}\text{Kr}$  is the  $T_z = -1$  member of this  $T=1$  triplet together with  $^{70}\text{Br}$  ( $T_z = 0$ ) and  $^{70}\text{Se}$  ( $T_z = 1$ ). The  $B(E2)$  and the  $E(2^+)$  values for  $^{70}\text{Br}$  and  $^{70}\text{Se}$  are known to be very similar. Therefore, no major shape change between these two nuclei is expected at low spin.

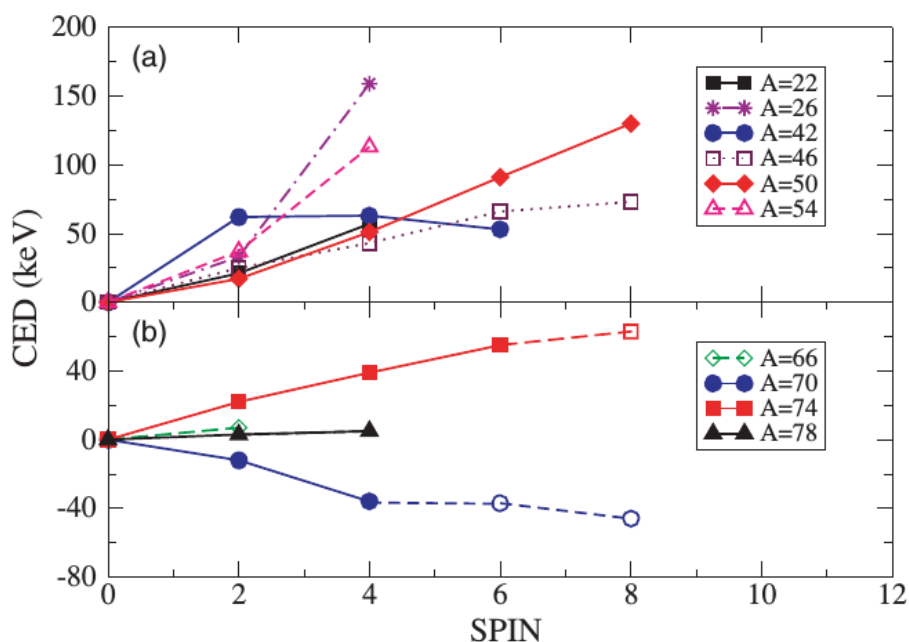


**Figure 1.3:** CED for neighboring isobaric multiplets is shown for different shell regions in (a) and (b), upper and lower plots. The negative tendency with increasing spin is seen only for the  $A=70$  case. Open symbols and dashed lines in the lower plot represent the tentatively assigned levels in the  $N=Z$  system considered [22].

The CED plot for  $^{70}\text{Br}$  and  $^{70}\text{Se}$  with neighboring multiplets is shown in Figure 1.3. These values were measured between the  $T_z = 0$  and  $T_z = 1$  members of the  $A=70$  triplet and a negative tendency with increasing spin was observed, unlike the other isobaric multiplets in the region. Unfortunately, a complete description of this phenomena is not achieved to date. This negative tendency is one motivation of our study to measure the third member of this triplet. There have been many theoretical approaches and suggestions trying to explain this negative tendency. The reason for this anomaly could be the polarization effects of the valence nucleons through the Coulomb interaction which could be a significant break down of the isospin symmetry, an influence of the electromagnetic spin-orbit interaction, the Thomas-Ehrman shift or the neutron excitation from the  $fp$  to the  $g_{9/2}$  intruder orbit in the shell model configuration [23, 22, 24]. Another

possible interpretation is the shape differences in  $^{70}\text{Br}$  and  $^{70}\text{Se}$  isobaric analogue states, indicating a large change in the deformation. The  $^{70}\text{Se}$  was measured to have an oblate ground state and the similar  $B(E2)$  and  $E(2^+)$  values were obtained for  $^{70}\text{Br}$ , quantifying a similar degree of deformation, suggesting no big shape change between these two isotopes, supported by theoretical calculations. The VAMPIR model family is one of these approaches that considers the potential effect of isospin symmetry breaking and shape coexistence on the structure of the nuclei. Considering different shape mixing as a function of spin, this model is able to reproduce the negative tendency in CED and also the ground state shape of the  $^{70}\text{Se}$ . Nevertheless, validity of the predictions in this model requires the complete experimental measurements of this isobaric triplet [25]. Measured transition energies from  $^{70}\text{Kr}$  are given in Chapter 5 and compared with the predictions of this model including the other members. Additionally, we enable the study of the MED and TED experimentally in this triplet which gives important information on the charge symmetric and charge independent nature of the nuclear force by studying the third member of this triplet,  $^{70}\text{Kr}$ .

## 2

# Nuclear Structure

The structure of the nuclei depends on the interplay between protons and neutrons which is governed by the nuclear forces. The main goal in nuclear structure physics studies is therefore to understand the effective forces between nucleons.

**Table 2.1:** *The existing forces in nature are given in the table with their effective ranges and interaction types. Interactions between nucleons are governed by the strong force but also are influenced by the weak and electromagnetic interactions.*

	Strong	Electromagnetic	Weak	Gravitational
Range	$10^{-15}$ m	$\infty$	$10^{-8}$ m	$\infty$
Carrier	Gluon	Photon	$Z, W^{\pm}$	Graviton
Relative Strength	1	1/137	$10^{-6}$	$10^{-39}$

There are four known forces in nature: strong, electromagnetic, weak and the gravitational force. Table 2.1 shows the effective ranges, carriers and the interaction types of them. The strong and electromagnetic force play a dominant role in the stability of nuclei. The charge independent strong force does not distinguish protons and neutrons as different particles, but the electromagnetic force does. The electromagnetic force acts as a repulsive force between protons due to their charge and tries to disintegrate the nucleus. When adding neutrons to the nucleus, the strong force between nucleons overcomes the repulsive Coulomb effect and keeps the nucleus together. The strong force is attractive between nucleons at distances of about  $1 fm$  from their centers, but rapidly decreases at distances beyond about  $2.5 fm$ . When the distance becomes less than  $0.7 fm$ , the nuclear force becomes repulsive. This repulsive component is responsible for the physical size of nuclei and prevents it from collapsing, since the nucleons cannot come closer than what the strong force allows.

Besides the electromagnetic and the strong force, the weak interaction is also important as it is responsible for the beta decay of nuclei. The weak force turns protons into neutrons and vice versa, so bound nuclei can decay by turning protons into neutrons and the other way around. Nevertheless, the content of this thesis does not include this type of interaction.

## 2.1 Nuclear Models

A nucleus is composed of two types of fermions bound together by the strong force including the effect of the other forces caused by the elementary particles within the atom such as quarks and electrons etc. Since the nucleus consists of a large number of constituents and the nuclear force is complex, there is still no unified theory that can explain all the nuclear properties at the same time. Different experimental techniques and theoretical approaches are necessary to understand and formalize the nature of the nuclei at least individually or for certain mass regions.

The nuclear many-body system has been studied from two different complementary aspects with microscopic and macroscopic models. The complete description can be achieved by a combination of both, starting with the macroscopic one, like the liquid-drop model (see Section 2.1.1), and complemented by microscopic models like applying shell model corrections (see Section 2.1.2) in order to explain the properties of the nucleus, such as binding energies at certain values. This approach is very successful in describing nuclear ground state properties [26].

An analytic microscopic calculation of nuclear properties requires a solution of the many-body non-relativistic Schrödinger equation. Each nucleon is considered to be an independent particle and the total constituent nucleons are bound to certain energy levels by a central potential, called the mean-field potential, created by all the nucleons. The mean field theory is widely used for the description of interacting many-body systems.

As a starting point, the Schrödinger equation is solved by considering the limited number of nucleons up to  $n$  in order to obtain the wave functions of the nuclear states.

$$H\psi(1,2,\dots,n) = E\psi(1,2,\dots,n) \quad (2.1)$$

where the Hamiltonian  $H$  is given as a sum of the kinetic-energy term and the potential. The potential is created by nucleon-nucleon two-body interactions of all nucleons. This non-relativistic Hamiltonian is written as;

$$H = \sum_{i=1}^n T_i + \frac{1}{2} \sum_{i,j=1}^n V_{i,j} \quad (2.2)$$

where  $n$  is the number of nucleons,  $T_i$  is the kinetic energy of the  $i$ th nucleon and  $V_{i,j}$  is the potential created by nucleon-nucleon interaction. The concept behind the mean field potential is that all nucleons of the nucleus move as independent particles within an average central potential  $U$ , described as:

$$U = \sum_{i=1}^n U_i \quad (2.3)$$

The existence of such an average potential stems from the Pauli exclusion principle, which leads to the fact that the mean free path of the nucleon is larger than the nuclear dimensions [27].  $H$  can then be given as two separate components, splitting up in two parts:

$$H = H_0 + H_1 = H = \sum_{i=1}^n [T_i + U_i] + \left[ \sum_{i,j=1}^n V_{i,j} - \sum_{i=1}^n U_i \right] \quad (2.4)$$

where  $H_0$  is the sum of one-body Hamiltonians and describes the nucleons as independent particles moving in an average field and the  $H_1$  is the residual interaction between valence particles and can be taken as a perturbation within a central mean-field potential generated by the nucleons themselves.

A brief description of how one can go beyond the mean-field approach with modern nuclear models is given at the end of this section.

### 2.1.1 Liquid Drop Model

This model describes the nucleus as a charged liquid drop from a macroscopic point of view. The nucleus is considered as an incompressible liquid drop with a very high density that is bound together due to the surface tension. The constant binding energy of the nucleons can be considered as analogous to the constant evaporation temperature of a liquid. This model is nicely able to explain the general features of the binding energy of a large number of nuclei, fusion and fission processes, energies of radioactive decays, however cannot explain excited states, the nuclear spin and why nuclei become more stable at a certain nucleon number [28].

### 2.1.2 Shell Model

It has been experimentally proven many times that nuclei with a certain number of protons or neutrons are more stable against radioactive decay than others. At proton and neutron numbers 2, 8, 20, 28, 50, 82, 126, an enhanced stability demonstrated that the nucleus has a shell structure, similar to that of the atomic electrons surrounding the nucleus. These are known as magic numbers and their structure is described by the shell model where the protons and neutrons separately fill quantized energy levels. A quantized energy level structure is suggested to solve the Schrödinger equation with the one-body Hamiltonian, and for convenience the mean field potential is usually approximated by a simple harmonic oscillator potential. However, the harmonic oscillator potential is only able to reproduce the first magic numbers 2, 8 and 20. It is therefore necessary to make improvements to this simple potential of the nucleus in order to correctly describe the experimentally observed magic numbers. A more realistic potential form for the nuclei is the Woods-Saxon potential, given as:

$$V_{WS}(r) = \frac{-V_0}{1 + \exp([r - R]/a)} \quad (2.5)$$

where  $V_0$  is the depth of the potential,  $r$  is the radial distance from the center of the potential,  $R$  and  $a$  are the radius and diffuseness parameters of the nucleus. This potential is an improvement on the infinite well or harmonic oscillator, but it still is not able to reproduce all of the known magic numbers. In order to accurately describe the higher magic numbers, the potential is modified by adding a spin-orbit interaction term, in analogy to the atomic case. This modified theoretical approximation is able to then reproduce certain numbers of neutrons and protons that are experimentally observed to result in a sudden drop in separation energy, associated with closing of nucleon shells.

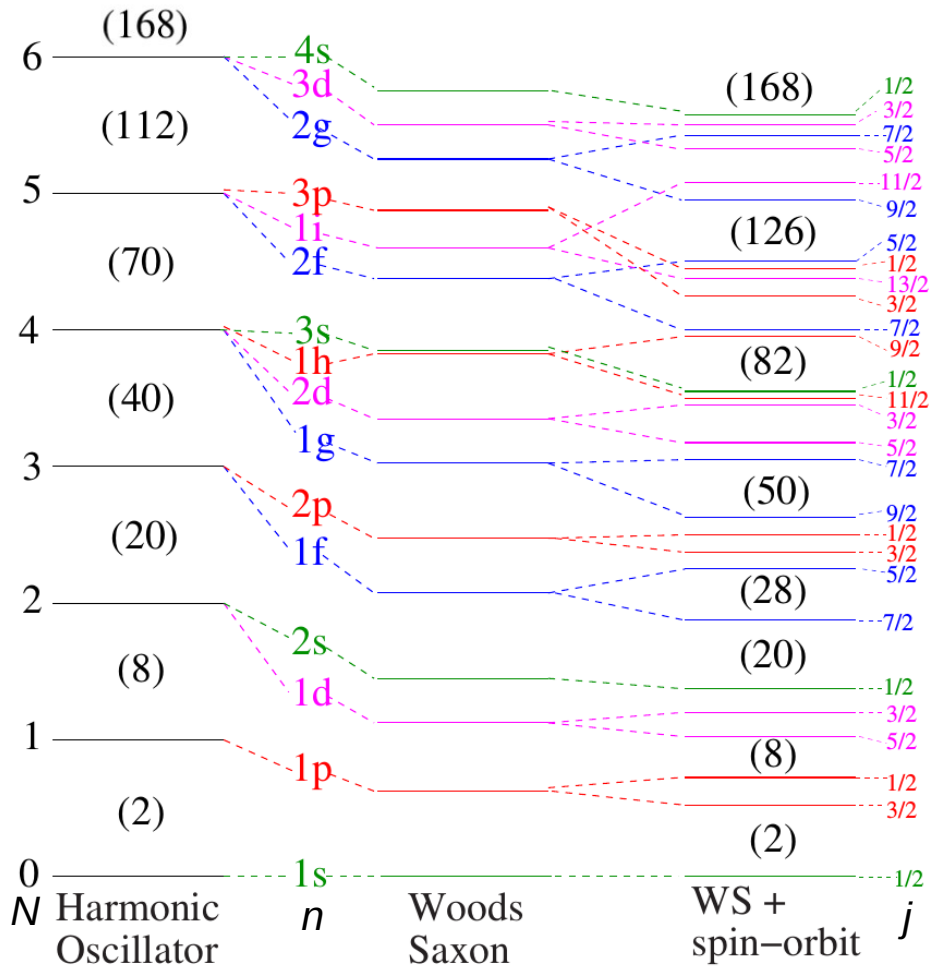


**Figure 2.1:** Evolution of the shell structure showing how the levels are created by using different central potentials in the shell model.  $N$  is the orbital number,  $n$  is the principle quantum number,  $j$  is the total angular momentum. On the left, the level order as a result of the harmonic oscillator potential is shown, the center represents the level ordering if a Woods Saxon type potential is applied. Adding a strong spin-orbit interaction to the Woods-Saxon potential, we obtain an additional degeneracy and a level ordering whereby the gaps in the levels correspond to the experimentally observed magic numbers [28].

An arrangement of these shells is shown in Figure 2.1, indicating the splittings as a result of different potentials and interactions that are considered.

In the shell model, the properties of the nucleus are given by the nucleons that are filling the levels outside of the shell closures. However, as the number of these valence nucleons increases, the model becomes computationally difficult to apply and also inaccurate to explain the underlying physics. Up to this point, the model can only describe a spherically shaped nucleus. However, as the number of valence nucleons increases, the motion of these valence particles can lead to a permanently deformed shape. In order to define equilibrium deformations of nuclei, one has to consider both macroscopic and microscopic effects together.

### 2.1.3 Nuclear Shapes and Deformation

The interactions between protons and neutrons outside closed shells drive the nucleus into non-spherical shapes. In order to minimize its potential energy and increase its stability, a deformed nucleus allows different configurations for its nucleons, relative to their wave functions. These configurations have an impact on the nuclear shape thus the shape of the nucleus depends on the potential and visa versa. This can be spherical or deformed, depending on the spatial characteristics of the nucleon wave functions. Depending on the number of nucleons, it does not only become non-spherical but even lead to different competing shapes very close together for certain proton ( $Z$ ) and neutron ( $N$ ) numbers. Since the nucleus is a quantum mechanical system, it can appear in different shapes with a certain probability. The evolution of nuclear shape with changing nucleon number gives insight into the many-body quantum systems and the underlying nuclear interactions.

For a deformed nucleus the radius  $R$  as function of  $\theta$  and  $\phi$  can be parametrized as:

$$R(\theta, \phi) = R_{av} \left[ 1 + \sum_{\lambda=2}^{\infty} \sum_{\mu=-\lambda}^{\lambda} \alpha_{\lambda\mu} Y_{\lambda\mu}(\theta, \phi) \right] \quad (2.6)$$

where  $\alpha_{\lambda\mu}$  is the expansion coefficient of the spherical harmonics  $Y_{\lambda\mu}(\theta, \phi)$  and  $R_{av}$  is the average radius of the nucleus. In this representation the nuclear volume is conserved. A nucleus can be excited with  $\lambda$  angular momentum and  $\lambda = 2$  gives the lowest order multipole, corresponding to quadrupole deformation. For instance, for axially symmetrical shapes, the radius of the nucleus in the first order is:

$$R(\theta, \phi) = R_{av} [1 + \beta_2 Y_{20}(\theta, \phi)] \quad (2.7)$$

These shapes are shown in Figure 2.2. The spherical, oblate and prolate shapes are always symmetrical around the axis. Additionally, a non-symmetric pear shape resulting from octupole deformation is observed rarely [29, 30].

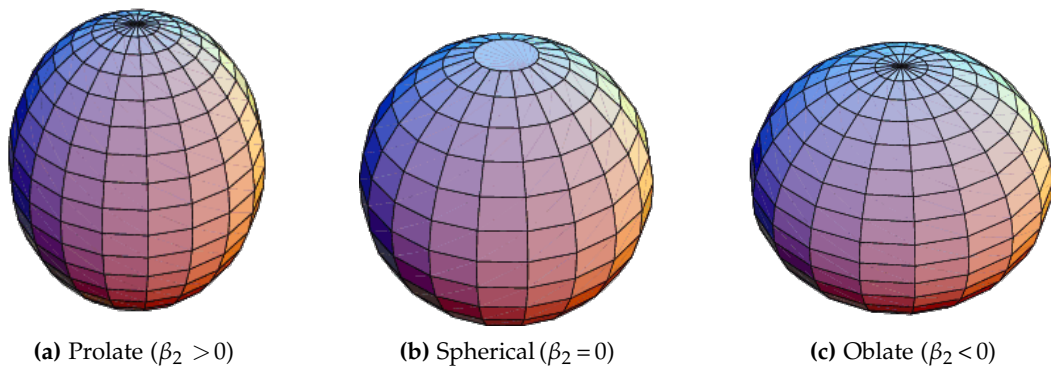


**Figure 2.2:** Three different shapes a nucleus can have, depending on the  $\beta_2$  value.

The quadrupole deformation parameter  $\beta_2(=\alpha_{20})$ , can be related to the axes of the spheroid by,

$$\beta_2 = \frac{4}{3} \sqrt{\frac{\pi}{5}} \frac{\Delta R}{R_{av}} \quad (2.8)$$

The average radius is  $R_{av} = 1.2 A^{1/3}$  and  $\Delta R$  is the difference between the major and minor axes while the total volume of the nuclei is conserved. A large  $\beta_2$  value corresponds to a strong deformation, while the positive values stand for prolate shapes and negative values indicate oblate shapes. Deformation of nuclei can be explained in different ways. One way to study the deformed shapes is using collective models where the nuclei rotate or vibrate. For a vibrating nucleus around a spherical equilibrium, the vibrational energy is quantized as a phonon. The  $\lambda = 2$  excitation is seen as a one phonon excitation carrying two units of angular momentum with units of  $\hbar$ . A two phonon excitation results in three states with angular momenta:  $0^+$ ,  $2^+$ ,  $4^+$  while a three phonon excitation results in  $0^+$ ,  $2^+$ ,  $3^+$ ,  $4^+$  and  $6^+$  states. One of the fingerprints for the applicability of the vibrational model is the energy ratio  $E(4_1^+)/E(2_1^+)$  which is 2 for pure harmonic vibration and typically 2-2.5 for experimentally measured values. In the case of a rotation, the nucleus is taken as an axially symmetric rigid rotating system along an axis perpendicular to the symmetry axis. In the case of even-even nuclei, where  $\mathbb{J}$  is the moment of inertia, the low-lying rotational energy levels are expected to have the following sequence:  $E(0^+) = 0$ ,  $E(2^+) = 6(\hbar/2\mathbb{J})$ ,  $E(4^+) = 20(\hbar/2\mathbb{J})$ ,... The  $E(4_1^+)/E(2_1^+)$  ratio is always equal to 3.33 for pure rotational nuclei.

In some cases, configurations with oblate and prolate shapes occur at low excitation energy in the same nucleus, which is called shape coexistence. A strong fingerprint of this phenomenon in even-even nuclei is the observation of low-lying  $0^+$  states with bands built on top of them. The experimental observables to determine the nuclear shape are quadrupole moments of excited states and electromagnetic transition rates between them. Another way to study the deformation of nuclei is by using the deformed shell model as an extension to the spherical shell model to explain the deformed potential.

#### 2.1.4 The Nilsson Model

The Nilsson model, also known as the deformed shell model takes the deformation of the nucleus into account when calculating nuclear properties. It is an independent particle model for non-spherical nuclei and allows the nucleons to move as independent particles in a deformed mean field potential. In this model, the  $2j+1$  degeneracy of each orbit is broken and this breaking increases with deformation. As a result of the deformation, the orbital angular momentum  $l$  and the intrinsic spin  $s$  are no longer good quantum numbers. States with different  $l$  values can mix and the energy of the states depends on the component of the angular momentum along the symmetry axis,  $\Omega$ . For each orbital with total angular momentum  $j$ , there are  $2j+1$  values of  $\Omega$ , owing to the reflection symmetry of axially symmetric degenerate nuclear levels as  $+\Omega$  and  $-\Omega$ . Using a deformation dependent Hamiltonian, the single-particle energies can be

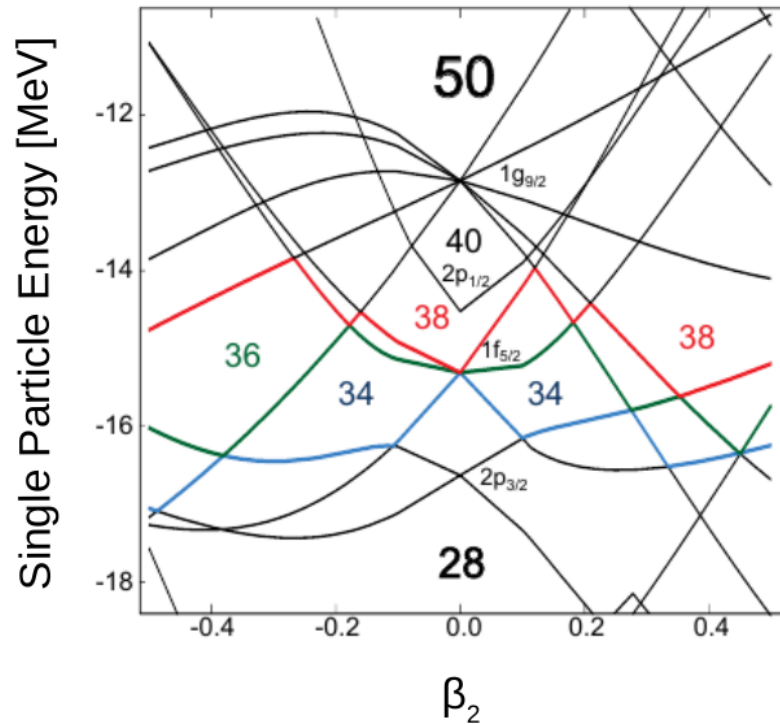


**Figure 2.3:** The Nilsson Diagram shows the evolution of the single-particle energies as a function of the nuclear deformation parameter. Positive  $\beta_2$  values correspond to prolate deformation and negative  $\beta_2$  values correspond to oblate deformation [31].

calculated as a function of the  $\beta_2$  deformation parameter. A plot of the single particle energies against deformation is known as Nilsson diagram, a schematic view of these levels is given in Figure 2.3. The Nilsson diagram shows a high level density between the magic numbers the 28 and 50, which corresponds to  $\beta_2 = 0$  (spherically shaped nucleus) on the diagram. Outside this region, oblate or prolate shapes are dominant depending on the sign, as the positive  $\beta_2$  values correspond to prolate deformation and negative  $\beta_2$  values correspond to oblate deformation with a lower level densities. The nucleus always tends to the low level density so that the energy can be minimum. Then, the nucleons fill orbitals up to the Fermi surface such that the energy is minimized, and when the nucleons are placed in these orbitals, deformation is created. As it is also the case in the spherical shell model, the energy is minimized when there is a shell gap. For instance,  $(N, Z) = 40$  gives a spherical shape, while for  $(N, Z) = 34, 36$  and  $38$  deformed shapes are preferred. The nucleon number 34 prefers both oblate and prolate deformation while 36 and 38 prefers oblate and prolate, respectively.

### 2.1.5 Modern Theoretical Approaches

Besides the macroscopic and microscopic models of nuclear structure, more elaborate models are also being studied since the many-body nature of nuclei warrant more complex potentials and the inclusion of residual interactions in order to describe the ob-

served nuclear behavior. But still, despite many advances in the field of nuclear modeling and the availability of more powerful computing systems, no single model is able to reproduce empirical observations across the enormous range of nuclei that reside in the nuclear landscape.

These modern calculations are also based on mean-field approaches, such as the Hartree-Fock (HF) method, where independent particles move in a self-consistent mean-field. In turn, it determines the best non-correlated ground state. As a starting point, the mean-field potential is governed by HF. The nucleon-nucleon interaction potential and the ground state wave function of the nucleus is calculated iteratively with an optimized HF potential, based on the minimization of the total nuclear energy. The equations are solved iteratively, in order to achieve the self consistent mean field. From here, a very commonly used approach called Random Phase Approximation (RPA) helps to include the ground-state correlation and the pairing effects. If the number of external particles increases, the deformed mean-field becomes effective. Then, this approximation can be extended including the pairing effects and becomes the Hartree-Fock-Bogolibouov (HFB) approximation [32]. This pairing effect can be also introduced by other approximations, building on HF such as HF+BCS [33]. Additionally, some other constraints can also be included during the calculations, such as deformation effects. The effective force in HF calculations is the Coulomb force, in order to study the nuclei, nuclear force has to be included. The effective force as a nuclear force is introduced to the calculations with a parametrization such as Skyrme [34] or Gogny [35]. Here, effective nucleon-nucleon interactions are parametrized to adjust them and reproduce the ground state properties of the nuclei. The Skyrme parametrization includes two and three body interaction terms and the Gogny includes a non-zero range force, better represents the pairing interaction, at the cost of requiring increased computational power. Every method has a different way to come from the fundamental nuclear field to the effective force that model is using. Solving these equations gives a Potential Energy Surface (PES) of the nucleus. The PES enables us to obtain the binding energies and different minima indicate different shapes of the nucleus (see Figure 1.2). In order to predict additional physical observables such as level energies and transition probabilities, models have to be enlarged to beyond the mean field.

## 2.2 Symmetry

Symmetries play a fundamental role in our basic understanding and in theoretical description of the nature. In this section, one of the phenomena will be described, which is based on symmetry rules as a starting point. In nuclei, the similarity of neutrons and protons is taken as symmetric and combined with the charge independence of the nuclear force, resulting in the concept of isospin symmetry. The use of the isospin formalism is explained in the next section.

### 2.2.1 Isospin

The isospin concept in nuclear physics was introduced by Heisenberg in 1932 considering the clustering of stable nuclei around the  $N=Z$  line [36]. He noted that such an effect indicates a symmetry of the strong interaction and, the neutron and the proton can be treated as two different quantum states of the same particle, called nucleon, with an internal degree of freedom: the isobaric spin or isospin. The isospin of a single nucleon is  $T=1/2$ . The projection on a quantization axis  $z$ ,  $T_z$ , in the isospin space, is defined as  $1/2$  and  $-1/2$  for neutron and for proton, respectively.

The concept of isospin is used to distinguish the Isobaric Analogue States (IAS) in nuclei with the same nucleon number  $A$ , but differing in proton and neutron numbers. These states are distinguished by the projection of total isospin vector,  $T_z$ , which for the nucleus is defined as:

$$T_z = (N - Z)/2 \quad (2.9)$$

In this case, the members of a given isospin multiplet  $T$ , for example the IAS  $^{70}\text{Kr}$ ,  $^{70}\text{Br}$  and  $^{70}\text{Se}$ , are the  $T_z = -1, 0, +1$  members of the  $A = 70$ ,  $T = 1$  triplet, respectively.

The existence of charge symmetry and charge independence cause the IAS to be identical when the Coulomb interaction between the protons is neglected. If the strong interaction conserves isospin, spectra of analogue nuclei would be identical. The Coulomb interaction of protons, of course, breaks the symmetry, however these effects can be calculated precisely.

In case of the charge symmetry, the interaction between the protons,  $V_{pp}$ , should be equal to the interaction between the neutrons,  $V_{nn}$ .

$$V_{pp} = V_{nn} \quad (2.10)$$

However, measuring the scattering lengths in nucleon-nucleon scattering experiments proved a slight asymmetry between these terms [37].

The charge independence means, in the same quantum mechanical state, the force between proton and neutron is the average of the force between two protons and two neutrons. This independence can be formalized as:

$$V_{np} = (V_{nn} + V_{pp})/2 \quad (2.11)$$

Hence, charge independence and charge symmetry combined require that the force between two protons, two neutrons and a proton and a neutron is equal. However, charge independence is also slightly broken. For the isospin  $T=1$  state, the proton-proton, neutron-proton and neutron-neutron interactions are slightly different, even after electromagnetic effects have been removed [38].

Charge symmetry and charge independence can be studied through the Coulomb Energy Differences (CED), Mirror Energy Differences (MED) and Triplet Energy Differences (TED) of the IAS.

## 2.2.2 Energy Differences in Isobaric Multiplets

Studying mirror nuclei is one of the best tools to probe isospin breaking effects as the fundamental assumption leads to an exchange symmetry between protons and neutrons. The mirror nuclei  $X$  and  $Y$  are defined as two isobaric states with the same mass number  $A$  and interchanged number of protons and neutrons. They are symbolized as  ${}^A_a X_b$  and  ${}^A_b Y_a$  where  $a+b=A$ . According to the symmetry rules, pairs of mirror nuclei should have the same spin, parity and identical shape in their ground state. Since the strong interaction is invariant for the protons and the neutrons, one can expect these mirror nuclei to have very similar binding energies, hence, potential energy surface as well. The  ${}^{70}_{36}\text{Kr}_{34}$  and  ${}^{70}_{34}\text{Se}_{36}$  nuclei are the mirror pair that is studied within this thesis. Studying such pairs of mirror nuclei, especially differences between their properties gives a direct insight into isospin symmetry breaking effects and the concept of the charge symmetry. Due to the symmetry breaking effects and existence of the Coulomb force,  ${}^{70}\text{Kr}$  is much less bound than  ${}^{70}\text{Se}$ . Additionally, the electromagnetic decay rates of mirror states can be used to decompose the multipole electromagnetic matrix elements into proton and neutron matrix elements [39], explained in detail in section 2.3.4.

The Coulomb Energy Differences (CED) in isobaric multiplets, is calculated with a following equation at each spin state,  $J$ :

$$CED_{J,T} = E_{J,T,T_z=0}^* - E_{J,T,T_z=T}^* \quad (2.12)$$

Mirror Energy Difference (MED), testing charge symmetry between two mirror nuclei or the Triple Energy Difference (TED), testing charge independence of the strong interaction in isobaric  $T=1$  triplets is also important probes of isospin symmetry breaking.

The MED is defined by the differences in the excitation energies of mirror nuclei and are taken as a measure of isospin symmetry breaking with a given equation as a function of spin  $J$ :

$$MED_{J,T} = E_{J,T,T_z=-T}^* - E_{J,T,T_z=T}^* \quad (2.13)$$

The TED, which accounts for the charge independence, is defined in a similar way as a function of the nuclear spin  $J$ :

$$TED_{J,T} = E_{J,T,T_z=-T}^* + E_{J,T,T_z=+T}^* - 2E_{J,T,T_z=0}^* \quad (2.14)$$

where  $E^*$  is the excitation energies of the states or the interested state of the same  $T$  in each nucleus.

The theoretical predictions of the MED and the TED in different mass regions are studied to probe the charge symmetry and charge independence [40, 41]. Comparisons between the isobaric analogue states are given in Section 1.1.2 to examine the evolution of the deformation when one proton or neutron is interchanged between two nuclei.

## 2.3 Experimental Technique

The aim of this experiment is to determine the  $B(E2)$  value of the first excited  $2^+$  state in order to study the collectivity around mass 70 region towards the proton drip-line. Study of exotic nuclei close to the proton drip-line in the laboratory presents a number of experimental challenges. First of all, it is important to choose an appropriate reaction that will populate the nuclei of interest with a sufficiently large cross section to make experimental measurements feasible. Following the reaction and the excitation, the nucleus decays to a lower state by emitting a  $\gamma$ -ray between initial  $|i\rangle$  and final  $|f\rangle$  states. These excitation and de-excitation processes are illustrated in Figure 2.4. To measure these  $\gamma$ -rays, a suitable detector array is needed.

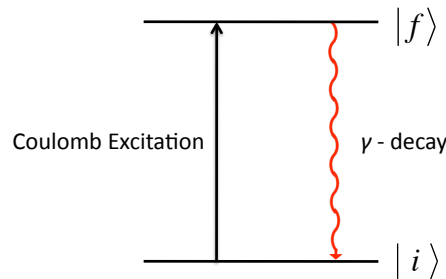


**Figure 2.4:** Schematic illustration of first-order Coulomb excitation followed by gamma-decay.

The isotopes of interest are produced in a RIB facility and are available as ion beams typically at relativistic energies of  $\sim 100 \text{ MeV}/u$ . Taking advantage of the high beam energy, a thick target [ $\sim 1 \text{ g}/\text{cm}^2$ ] can be used to increase the interaction rate and the photon yield. Despite the thick target, the energy loss of the beam is only a few percent, acceptable in terms of Doppler shift of the  $\gamma$ -rays, and in terms of the uniformity of cross-sections. The most suitable way to excite the nuclei of such a beam is through scattering on heavy target via the electromagnetic interaction. The underlying process is called Coulomb excitation, that is explained in Section 2.3.1. At such energies, above the Coulomb barrier, electromagnetic and nuclear excitations interfere. However, both processes can be distinguished by their scattering angle dependence. Another way to extract the electromagnetic excitation from this combination is by measuring the pure inelastic excitation, defining the deformation lengths of this process and use them to extract the Coulomb excitation part by using theoretical models.

### 2.3.1 Coulomb Excitation Theory

In the classical approximation of the Coulomb excitation process, the projectile can be considered as a point-like charge moving along a hyperbolic orbit in the repulsive Coulomb field of a target nucleus as shown in Figure 2.5.

When the projectile follows such a Rutherford trajectory, according to the half-distance approach, the Coulomb excitation cross section is given by:

$$\left(\frac{d\sigma}{d\Omega}\right)_{Ruth} = \left(\frac{a_0}{2}\right)^2 \sin^{-4}\left(\frac{\theta}{2}\right) \quad (2.15)$$

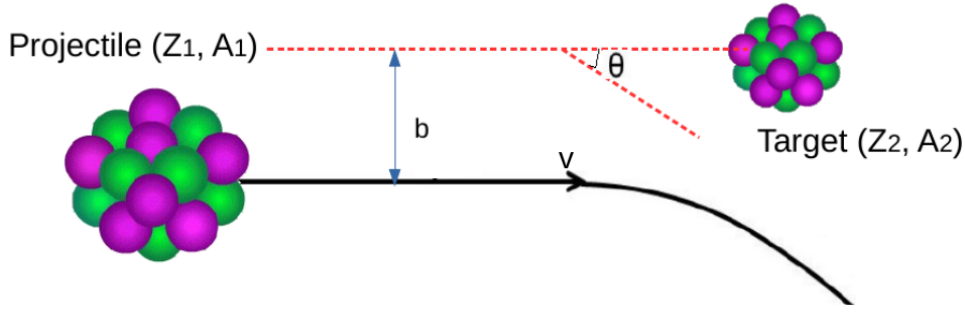


**Figure 2.5:** The projectile is scattered by an angle  $\theta$  under the electric field of the heavy target with a velocity  $v$  at an impact distance  $b$ .

$$a_0 = \frac{Z_1 Z_2 e^2}{4E} \quad (2.16)$$

where  $\theta$  is the scattering angle,  $Z_2 e$  is the charge of the target nuclei,  $Z_1 e$  is the charge of the projectile, and  $E$  is their kinetic energy in the Center of Mass (CM) system.

Under certain conditions, Coulomb excitation can be treated in a semi-classical approximation in which the classical trajectories of the elastic scattering process are used. In this method, in order to excite a state via a time dependent potential, the interaction time  $t_{int}$ , has to be shorter or at least of the same magnitude as the excitation time  $t_{exc}$  for a given excitation energy  $\Delta E$ . This relation is defined as the adiabatic parameter  $\xi$ , given as:

$$\xi = \frac{t_{int}}{t_{exc}} = \frac{b\Delta E}{2\hbar v} \leq 1 \quad (2.17)$$

As it is clear from this relation, at small velocities, excitation probability adiabatically decreases. The strength of the Coulomb interaction is defined with the Sommerfeld parameter:

$$\eta = \frac{b}{2\lambda} = \frac{Z_t Z_p e^2}{\hbar v} \gg 1 \quad (2.18)$$

where  $\lambda$  is the de Broglie wavelength of the projectile. When  $\eta \gg 1$ , the electromagnetic interaction is strong enough to ensure that the short-range nuclear interactions are not involved in the reaction, a quantum mechanical wave packet is expected to follow the classical trajectory and the semi-classical approximation can be applied to treat the excitation process. In this case, the relative motion of projectile and target is considered classically, while the excitation process is treated quantum mechanically.

An accurate, pure Coulomb excitation measurement must be free of nuclear contributions. During such a process, projectile and target only interact through the electromagnetic field. In order to achieve this requirement, the distance between the projectile and the target must not exceed the impact parameter,  $b$  for beam energies above the Coulomb barrier, and the scattering angle of the projectiles has to be limited to sufficiently small angles. At high energies above Coulomb barrier, a straight-line motion can be assumed for the projectile. It is characterized by an impact parameter, equal to

the distance of closest approach and the nuclear interaction radius [42]. The projectile deflection angle is given as:

$$\theta_{lab} = \frac{2Z_1Z_2e^2}{Ac^2\beta^2\gamma b} \quad (2.19)$$

where  $A$  is the mass of the projectile at rest,  $b$  is the closest distance between target and projectile. Limiting the scattering angle to small values, the impact parameter that will avoid the nuclear interaction contribution can be safely chosen.

In another scenario, depending on its energy and the impact parameter, the projectile may come closer to the target nucleus by overcoming its electromagnetic field. In order to ensure that the Coulomb excitation process is safe and nuclear contributions to the excitation are negligible or excluded, the scattering angle is sufficiently small to obey that, the distance of closest approach must be larger than the sum of the radii of the projectile and the target nuclei, plus an additional safety distance,  $\Delta$ :

$$b \geq R_p + R_t + \Delta \quad (2.20)$$

$\Delta$  is introduced for the range of the nuclear forces and the surface diffuseness of the nuclear density distribution and usually taken between 2 to 5  $fm$ . The distance of closest approach depends on the energy and the impact parameter. This semi-classical description is valid as long as the Coulomb field prevents the projectile from penetrating into the target nucleus which requires the wavelength of the projectile  $\lambda$  to be much smaller than the distance of closest approach  $b$ .

To summarize, at low energies, below Coulomb barrier, the charge distributions of the two nuclei cannot overlap due to the Coulomb repulsion, which allows only the electromagnetic interaction and, the contributions from the strong interaction becomes negligible. At intermediate energies, the projectile can get so close to the target that, it becomes possible for nuclear interactions to contribute to the excitation process, also exciting high-lying states. Therefore, the best and possible way to study the excitation process must be chosen. In the majority of cases, if the angular resolution of the tracking detectors allows, the scattering angle or impact parameter can be restricted and the cross section for the Coulomb excitation process is calculated in a semi-classical approximation where the cross section depends on the minimum impact parameter as a function of the scattering angle:

$$b_{min} = \left( \cot \left( \frac{\theta_{max}^{CM}}{2} \right) + \frac{\pi}{2} \right) \frac{Z_p Z_t e^2}{\gamma m_0 v^2} \quad (2.21)$$

with the maximum scattering angle in the center of mass system, the target and projectile charges, the reduced mass of the two nuclei  $m_0$ , and the velocity  $v$  of the projectile in the laboratory frame. If it is not possible to use the scattering angle information, theoretical methods are needed to be used in order to describe the Coulomb and nuclear interference for non-safe scattering angles. However, in this case the extraction of the transition matrix element becomes difficult and model dependent. Figure 2.6 represents the angular distribution of this interference of the Coulomb and nuclear interaction processes, calculated by the ECIS-97 program for  $^{72}Kr$  beam scattering off a  $^{197}Au$  target. At

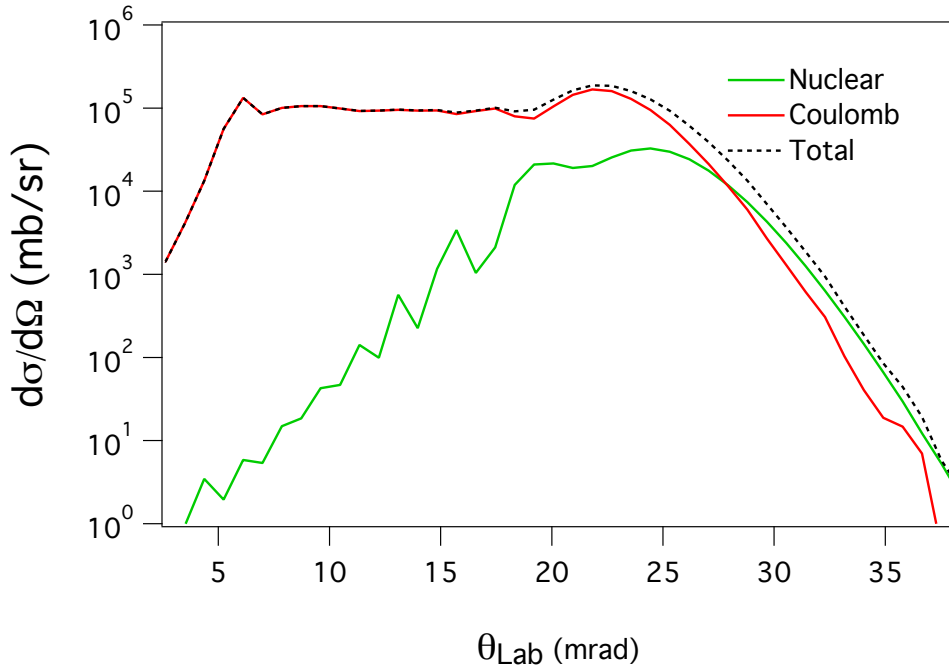


**Figure 2.6:** ECIS calculation for  $^{72}\text{Kr}$  beam scattering off a  $^{197}\text{Au}$  target at an energy of around 150 MeV/u. The figure illustrates the excitation cross section as a function of scattering angle of the interacted particles for only Coulomb excitation, only nuclear interaction and the sum of these two processes.

small angles nuclear interaction is negligible and around 27 mrad it starts to dominate. This point corresponds to the impact parameter that is explained above, where the safe angle can be chosen if the angular resolution of the tracking detector is good enough.

A quantum mechanical approach can be used where the system is described by wave functions taking into account the effective potentials caused by the Coulomb and nuclear fields. As a starting point, the motion of the projectile is described by a wave-packet and the resulting scattering process is expressed by the time-dependent Schrödinger equation:

$$i\hbar \frac{\delta}{\delta t} |\psi(t)\rangle = H |\psi(t)\rangle \quad (2.22)$$

where the Hamiltonian is:

$$H = H_0 + V(\vec{r}(t)) \quad (2.23)$$

where  $V(\vec{r}(t))$  is the electromagnetic interaction between the two nuclei. By treating this Coulomb potential as a time-dependent perturbation, the amplitude of the excitation probability is given as:

$$a_{i \rightarrow f} = \frac{1}{i\hbar} \int_{-\infty}^{\infty} dt e^{i\omega_{fi}t} \langle f | V(\vec{r}(t)) | i \rangle \quad (2.24)$$

where  $\omega_{fi} = (E_f - E_i)/\hbar$ . The excitation probability of the nucleus from initial state  $|i\rangle$  to a final state  $|f\rangle$ ,  $P_{if}$  is used to determine the Coulomb excitation probability, which is  $P_{if} \cdot (d\sigma/d\Omega)_{Ruth}$  (see equation 2.15).

The electromagnetic interaction between target and projectile can be decomposed in its multipole components. The monopole-monopole part of the electrostatic interaction causes the nuclei to scatter elastically, yielding the known Rutherford scattering process. The monopole-multipole components induce inelastic scattering, from which the nuclei are energetically excited. The time-dependent Hamilton operator  $V(\vec{r}(t))$  has to be defined in terms of a multipole expansion, considering spherical harmonics. After expanding the potential into its multipole components, giving  $\lambda$  as the multipolarity of the excitation and  $\mu$  is its projection, the Coulomb potential can be written as  $V_{\lambda\mu}(\vec{r}(t))$ . The solution of this approach leads to the Coulomb excitation cross section for an electromagnetic excitation of a state including the relation to the reduced transition probabilities as:

$$\sigma \approx \left( \frac{Ze^2}{\hbar c} \right)^2 \frac{B(E\lambda, 0 \rightarrow \lambda)}{e^2 b_{min}^{2\lambda-2}} \frac{1}{\lambda-1} \quad (2.25)$$

for multi-polarities of the transition  $\lambda \geq 2$ , and the charge of the target nucleus  $Z$  in the case of projectile excitation. More information about relativistic and low-energy Coulomb excitation can be found in the literature [43, 44].

Indeed, there is a linear relation between this Coulomb excitation cross-section and the reduced transition probability matrix element. Due to this proportionality of  $\sigma$  and  $B(E\lambda)$ , the reduced transition probabilities can be obtained from measurements of Coulomb excitation cross sections via the calculation of the cross section yields. The  $B(E\lambda, 0 \rightarrow \lambda)$  values in equation 2.25 are the reduced transition probabilities and provide a link between theoretical predictions and experimental observables. They are defined as:

$$B(L\lambda; J_i \rightarrow J_f) = \sum_{M_i M_f} |\langle \alpha_f, J_f, M_f | O(L, \lambda M) | \alpha_i, J_i M_i \rangle|^2 \quad (2.26)$$

$$= \frac{1}{2J_i + 1} |\langle \alpha_f, J_f, M_f | O(L, \lambda) | \alpha_i, J_i M_i \rangle|^2 \quad (2.27)$$

where the electromagnetic operator  $O(L, \lambda, M)$  has either an electric or magnetic character,  $\alpha_{i,f}$  represents the set of quantum numbers, describing the initial and final states,  $L$  is the orbital angular momentum and  $M$  is the magnetic quantum number. How this representation relates to the  $\gamma$ -ray decay of excited states is discussed in Section 2.3.4.

### 2.3.2 Nuclear Inelastic Scattering

When the energy of the incoming beam is higher than the Coulomb barrier and the distance criteria is not fulfilled, an inelastic scattering process governed by the strong interaction occurs. Depending on the energy and mass of the nuclei, multiple spin states can be excited. The process can be described as a valence nucleon kicked to another shell energy level or the incoming wave function is disturbed by the nuclear potential, resulting in vibrational or rotational excitations of the nucleus surface. The energy that arises from this interaction is equal to the difference between excited states. There are different theoretical approaches to study this process considering the effective potential [45, 46].

In the most general scattering theory, the total wave function is described as the sum of an incident plane wave function and an outgoing spherical scattered wave function with a certain scattering amplitude  $f(\theta, \phi)$ :

$$\Psi(\vec{k}, \vec{r})(r \rightarrow \infty) \rightarrow e^{i\vec{k}\vec{r}} + f(\theta, \phi) \frac{e^{\pm i\vec{k}\vec{r}}}{r} \quad (2.28)$$

Hence, all of the scattering information is contained within the scattering amplitude and the angular distribution is expressed by the differential cross section. The majority of the current theories start with elastic scattering and inelastic or reaction events are treated as perturbations. This leads for example to the so-called Distorted-Wave Born Approximation (DWBA), that describes the relative motion before and after an inelastic event. This approximation assumes an additional potential  $\Delta U$  on the top of main potential  $U(\vec{k}, \vec{r})$ . In this case, pure Coulomb wave functions  $\psi$  can be replaced with the ones that are distorted by an additional potential, and can be written as:

$$[\Delta^2 + \vec{k}^2 - \Delta U(\vec{r})]\chi(\vec{k}, \vec{r}) = 0 \quad (2.29)$$

where  $\chi(\vec{k}, \vec{r})$  is the superposition of the incoming plane wave function and the outgoing scattered wave functions  $\chi_f^{(-)}(\vec{k}, \vec{r})$  and  $\chi_i^{(+)}(\vec{k}, \vec{r})$ , respectively, with momentum  $\vec{k}$  and  $\vec{r}$  the relative position of two interacting particles.

If the nucleus is deformed, using equation 2.6, the perturbation potential can be written as:

$$\Delta U = R_0 \left( \frac{\delta U}{\delta R} \right)_{R_0} \frac{R}{R_0} - 1 \quad (2.30)$$

where  $R_0$  is the equilibrium radius considering the deformation. The relation between equation 2.6 and the obtained deformed potential leads to the deformation parameter,  $\beta_\lambda$ .

The transition matrix for inelastic scattering in DWBA from an initial to a final state is given by [47]:

$$T_{fi} = \int \chi_f^{(-)}(\vec{k}, \vec{r}) \langle f | \Delta U(\vec{k}, \vec{r}) | i \rangle \chi_i^{(+)} d(\vec{r}) \quad (2.31)$$

where  $\chi_{if}^{\pm}$  are the distorted wave functions for incoming and outgoing wave functions. These wave functions contain diffraction as well as absorption contributions and are described by the optical model of elastic scattering for the relevant entrance and exit channels.

### 2.3.3 The Optical Model

When the incoming wave function interacts with the target, the amplitude of the outgoing wave function decreases according to the strength of the interaction. The optical model is used to explain this process. It requires a real potential and an imaginary potential that represents the interaction with the excited channels since the parameters of the nuclear interaction is not well defined. The total potential  $U(\vec{r})$ , is described by a real  $V(\vec{r})$ , and an imaginary  $iW(\vec{r})$  parts. It contains a set of parameters which depends on

the incident projectile energy, as well as on the masses and charges of the projectile and target nuclei. Using the optical potential, the Schrödinger equation can be written as:

$$\frac{\delta^2 \psi(\vec{r})}{\delta r^2} + \left[ \frac{2\mu}{\hbar^2} (E - U(\vec{r})) \right] \psi(\vec{r}) = 0 \quad (2.32)$$

where,  $\mu$  is the reduced mass of the system,  $\psi(\vec{r})$  is the total wave function and  $(\vec{r})$  is the relative position of the two particles. Numerical solutions of this equation give the scattering matrix elements, scattering amplitude, and thus the differential cross-section. The real part of the optical potential describes the refraction of the incoming wave and the imaginary part describes the inelastic scattering through absorption. The amplitude of the imaginary potential increases with the incoming particle energy since the nuclear potential is energy dependent. Finally, the optical potential has a general form of:

$$U(r) = V_c(r) - V_v(r) + V_s(r) - i(W_v(r) + W_s(r)) \quad (2.33)$$

where the first term is the Coulomb potential, the second one is the real nuclear potential. The rest of the contributions are the imaginary potential as the sum of volume and surface parts. Occasionally, a spin-orbit potential is added for heavy-ion scattering, although the effect on the cross-section is small. The Coulomb potential of a uniformly charged sphere with radius  $R_C$  is described as:

$$V_c(r) = \frac{Z_p Z_T e^2}{2R_c} \left[ 3 - \frac{r^2}{R_c^2} \right], r \leq R_c \quad (2.34)$$

$$V_c(r) = \frac{Z_p Z_T e^2}{r}, r \geq R_c \quad (2.35)$$

Here  $A$  and  $Z$  are the nuclear mass number and charge.  $Z_P$  and  $Z_T$  refer to the projectile and target nucleus respectively.

If the radial part is taken as a Woods-Saxon potential, the real part of the nuclear potential is given by:

$$V_r(R) = V_0 \left( 1 + \exp \left( \frac{R - r_l A_T^{1/3}}{a_l} \right) \right)^{-1} \quad (2.36)$$

and the volume imaginary potential is given by:

$$W_v(R) = W_0 \left( 1 + \exp \left( \frac{R - r_r A_T^{1/3}}{a_r} \right) \right)^{-1} \quad (2.37)$$

The surface imaginary potential is given by:

$$W_s(R) = -4a_D W_D \frac{d}{dR} \left( 1 + \exp \left( \frac{R - r_D A_T^{1/3}}{a_D} \right) \right)^{-1} \quad (2.38)$$

where  $V_r$  and  $W_v$  are the real and imaginary volume potential well depths,  $W_D$  is the well depth for the surface derivative term,  $R$  and  $a$  are the radius and surface diffuseness parameters, respectively. The parameter  $a$  is known as the barrier width where the

potential drops from 90% to 10%. The surface part dominates at low energy and the volume part becomes important at high energy. The choice of the potential shape is based on the nuclear saturation. Since the density of the nucleus is constant in the middle and quickly drops at its surface, most of the time this potential has the highest amplitude close to the surface. Since the target cannot penetrate the projectile, reactions happen at the surface and only the surfaces of two nuclei interact. Outer, valence nucleons are able to absorb energy, while for the inner nucleons there is no possibility to absorb energy as all nearby energy levels are occupied. Only if the incoming particle energy is too high, the imaginary part of the optical potential starts to act like the real potential.

Since the potential that is used in this model includes the Coulomb and nuclear parts, it can be used to separate the nuclear deformation and charge deformation lengths,  $\delta_n$  and  $\delta_c$  respectively. In this case, the nuclear part of the optical potential will be only affected by the nuclear deformation, while the Coulomb potential will be affected by the charge deformation length.

### 2.3.4 Gamma Decay

The excited nucleus may lower its energy by  $\gamma$ -ray emission,  $\beta$  decay, nucleon emission, conversion electron emission or fission. The decay of the excited states discussed here are possible only through  $\gamma$ -ray and conversion electron emission. The  $\gamma$ -ray decay is an electromagnetic decay process via photon emission. The photon field can be expanded into multipoles of either electric,  $E$ , or magnetic,  $M$ , type depending on the spins and parities,  $\pi$ , of the connected states. These states are represented as  $J_i^\pi$  and  $J_f^\pi$ . The type of the excitation is defined by certain selection rules on angular momentum and parity. The allowed multipolarities are restricted by:

$$|J_f^\pi - J_i^\pi| \leq \lambda \leq |J_f^\pi + J_i^\pi| \quad (2.39)$$

where  $\lambda$  is the multipole order of the emitted radiation. The transition is further classified as electric or magnetic based on the parities of the initial and final states,  $\pi_i$  and  $\pi_f$ :

$$\pi_i \pi_f = \begin{cases} (-1)^\lambda & \text{for } E\lambda \rightarrow \text{electric decay} \\ (-1)^{\lambda+1} & \text{for } M\lambda \rightarrow \text{magnetic decay} \end{cases} \quad (2.40)$$

where  $\lambda \neq 0$ , which means that  $0^+ \rightarrow 0^+$  is forbidden via single  $\gamma$ -ray decay since the photons are bosons with spin = 1 and they must carry at least one unit of angular momentum. Nevertheless, there are a few examples of even-even nuclei that have first excited and ground states that are both  $0^+$ . Once populated, these states decay by the internal conversion processes, via atomic electrons with significant penetration into the nucleus, and are directly emitted from the atom.

The angular correlation measurements can give information about the multipolarity of a  $\gamma$ -ray. This is simply the measurement of  $\gamma$ -ray intensity variation as a function of angle between the direction of  $\gamma$ -ray emission and another fixed direction such as the direction of an incident beam which excites the decaying state, or the direction of the

emission of a particle.

The  $\gamma$ -ray intensity as a function of angle in terms of Legendre polynomials is represented as:

$$W(\theta) = \sum_{k=0}^{2L} a_k P_k \cos(\theta) \quad (2.41)$$

where  $a_k$  are the coefficients that depend on the nuclear spins of the involved states and can be deduced experimentally from angular momentum carried by the  $\gamma$ -ray and the mixing ratios.

### 2.3.5 Collectivity Quantities

The energy of the first excited  $2^+$  state in even-even nuclei and the  $B(E2; 0^+ \rightarrow 2^+)$  values are sensitive to the presence of shell gaps, nuclear deformation, and nucleon-nucleon correlations in nuclei. For even-even nuclei, considering equation 2.27, the electromagnetic excitation strength for electric quadrupole transitions E2 can be written as:

$$B(E2; J_i \rightarrow J_f) = \frac{1}{2J_i + 1} \langle \Psi_f || E2 || \Psi_i \rangle^2 \quad (2.42)$$

where  $\langle \Psi_f || E2 || \Psi_i \rangle^2$  is the reduced E2 matrix element and  $J_i$  stands for the initial spin state while  $J_f$  is the final one. The electromagnetic excitation strength,  $B(E2)$  is a measure of quadrupole collectivity and is expected to be small if the valence nucleons are close to the shell closure, or at a closed shell, while it is expected to be large in case of collective nuclei when they are located close to the mid-shell. The reduced transition probability for a  $0^+ \rightarrow 2^+$  transition in an even-even nucleus is related to the Coulomb deformation parameter  $\beta_c$ :

$$B(E2) \uparrow = \left( \frac{3}{4\pi} Z e^2 R^2 \beta_c \right)^2 \quad (2.43)$$

where the  $Z$  is the charge of the excited nucleus,  $\beta_c$  is the deformation parameter and  $R$  is the nuclear radius.

Another powerful quantity for nuclear structure studies is the electric quadrupole moment that is connected to the nuclear wave functions, thus  $B(E2)$  values. For the  $0_1^+ \rightarrow 2_1^+$  transition, the relation between  $B(E2)$  value and intrinsic quadrupole moment  $Q_0$  is [48]:

$$B(E2; J_i \rightarrow J_f) = \frac{5}{16\pi} e^2 Q_0^2 \quad (2.44)$$

Hence, the  $B(E2)$  value contains information on the deformation of the nucleus. A negative spectroscopic quadrupole moment describes a prolate shape, whereas a positive spectroscopic quadrupole moment is linked to an oblate shape.

Inelastic scattering enables measurement of the transition matrix elements  $M_n$  and  $M_p$ .  $M_n$  and  $M_p$  stand for the neutron and proton transition matrix elements, respectively and can be used to identify the contribution of each nucleon to the excitation. In the basic picture of a collective nucleus, protons and neutrons would contribute equally and the ratio of the matrix elements follows  $N=Z$ . But, taking the closed shells and

the valence nucleons into account, the ratio deviates from  $N=Z$  and these deviations between  $M_n$  and  $M_p$  can be a measure of the isospin breaking between the IAS and also provide information about the relative contributions of neutrons and protons to the collective mode. They show how proton and neutron polarize the nucleus in a different way. Additionally, deviations lead to the conclusion that the deformation lengths for electromagnetic and nuclear interactions depend both on the spines of the nucleus and its energy [49], which makes the link between deformation parameters and the  $B(E2)$  values, confirming the reliability of the method that we use in order to deduce the  $B(E2)$  values.

Coulomb excitation is an electromagnetic tool that is sensitive to the charged protons, therefore to the  $M_p$  value. The proton transition matrix element for  $0^+ \rightarrow 2^+$  transition is directly related to the reduced electric quadrupole transition probability  $B(E2)$  stemming from the equation 2.42 as follows:

$$B(E2; J_i \rightarrow J_f) = \frac{M_p^2}{2J_i + 1} \quad (2.45)$$

The proton and neutron multipole matrix elements can be written in terms of isospin representation [39]:

$$M_{n(p)} = \frac{M_0(T_z) \pm M_1(T_z)}{2} \quad (2.46)$$

where  $M_0(T_z)$  is the isoscalar and  $M_1(T_z)$  the isovector multipole matrix element. Here, isoscalar refers to the part of the potential that makes no distinction between protons and neutrons and isovector means that neutron and proton constituents are treated differently. Assuming isospin conservation, the neutron and proton matrix elements for a mirror pair can be written as:

$$M_p(-T_z) = M_n(T_z) \quad (2.47)$$

and

$$M_p(T_z = 0) = \frac{1}{2}M_0(T = 1) \quad (2.48)$$

which means,  $M_p$  can be obtained by measuring the electromagnetic transition for the corresponding transition in the mirror nuclei and for  $T_z = 0$  nucleus,  $M_0$  can be obtained directly [39]. Hence, the  $B(E2)$  values can be used as a test of isospin symmetry.

# 3

## Experimental Setup

The experiments outlined in this chapter were performed to determine the reduced transition probability  $B(E2)\uparrow$  values of  $^{70}\text{Kr}$ ,  $^{70}\text{Br}$ ,  $^{68}\text{Se}$  and  $^{72}\text{Kr}$ . The method used to obtain  $B(E2)\uparrow$  is to scatter the exotic beam particles off a stable heavy target Au and to detect them in coincidence with the emitted  $\gamma$ -rays. In addition, nuclear inelastic scattering on a Be target was used to determine the nuclear interference to the excitation. For both cases, the ejectiles have been measured using the ZeroDegree Spectrometer at RIBF, RIKEN, while the emitted  $\gamma$ -rays have been detected with the DALI2 scintillator array. This chapter is dedicated to explain the beam production, processing, beam line detectors, the electronics and the performed simulations. Detailed information for each setting is also given describing the beam profile and the reaction target.

### 3.1 Radioactive Ion Beams

The investigation into the region far from stability requires experiments with Radioactive Ion Beams (RIB). RIBs can be produced in different ways, the Isotope Separation On Line (ISOL) and the In Flight (IF) techniques [50].

The ISOL method was invented in Copenhagen in 1951 [51]. In this method, a high energetic primary charged beam impinges on a thick target of several cm length creating exotic particles by fission or fragmentation reactions. It relies on the production cross section as well as the chemical properties of the elements of interest. The thick targets are preferred for the production of high intensity radioactive beams to increase the yield. The reaction products are extracted in the form of ions, after the selection of the mass. Post acceleration can be performed if required for the experiments. Since the ions are produced at rest, the ISOL technique is ideally suitable for low-energy experiments. The disadvantage of the ISOL method is the general difficulty in achieving high beam purity due to many isobars of different elements produced in the target. There are several ISOL facilities operating or being constructed around the world such as ISOLDE at CERN [52], SPIRAL at GANIL [53], SPES at Legnaro [54], ISAC at TRIUMF [55] and FRIB in USA [56].

In the In-Flight method, heavy ion beams are impinging on a thin target to induce fusion, fission or fragmentation reactions. The reaction products retain a large fraction of the initial projectile velocity, due to linear momentum conservation and they have a kinematic focusing at small angles along the beam direction. A fragment separator is located along the primary beam axis and, the selection of the RIB of interest is performed through the deflection of ions in magnetic and electric fields. Unlike the ISOL technique, this selection is independent of the chemical properties of the radioisotopes under production. There are several facilities around the world, where RIBs are produced with the In-flight technique. These are mainly NSCL-MSU in USA [57], GSI in Germany [58], GANIL in France [59] and RIKEN in Japan [60]. The experiments performed within this thesis were carried out at the Radioactive Isotope Beam Factory (RIBF), RIKEN Nishina Center. RIBF can provide stable beams at very high intensities and energies. For the present experiment, a primary beam of  $^{78}\text{Kr}$  was produced at an energy of  $345\text{ MeV/u}$  with an intensity of  $\approx 350\text{ pA}$ . Exotic beam production and identification followed by the desired secondary reaction and identification of the reaction products were done using the BigRIPS fragment separator and the ZeroDegree Spectrometer. Detector Array for Low Intensity 2 (DALI2) was used for the identification of the  $\gamma$ -rays that are emitted in the course of the de-excitation.

### 3.1.1 Production of RI Beams at RIKEN

At RIBF, the production starts with accelerating the ions from the ECR ion source up to  $6\text{ MeV/u}$  using the RILAC linear accelerator. After the first acceleration of the ions, the beam is injected into the RIKEN Ring Cyclotron (RRC), the Fixed frequency Ring Cyclotron (FRC), Intermediate Stage Ring Cyclotron (IRC) and lastly the Superconducting Ring Cyclotron (SRC). There are two charge strippers in this mode: one is located behind the RILAC, and the other is behind the RRC. SRC is the first Superconducting Ring Cyclotron in the world that consists of six superconducting sector magnets. Detailed information on the acceleration process can be found in reference [61, 62]. The stages that are used to produce and accelerate the primary beam are shown in Figure 3.1.

After the SRC, the beam is extracted and sent to BigRIPS, where it is bombarded on a primary target to produce the secondary RI-beams. For the experiments that were performed within this thesis work, a  $^{78}\text{Kr}$  isotope beam was accelerated to  $345\text{ MeV/u}$  and impinged on a  $7\text{ mm}$  thick  $^9\text{Be}$  primary target in order to produce the  $^{70,72}\text{Kr}$  isotopes as a secondary beam via projectile fragmentation.

### 3.1.2 Separation and Identification of the RI Beams

Separation and identification of exotic nuclei is done based on the following principle; a charged particle moving with a certain velocity through a magnetic field is influenced by the Lorentz force. According to the Lorentz force, particles with different charge move on different paths in a uniform magnetic field. The motion of a particle with charge  $q$  and mass  $m$ , moving in a homogeneous magnetic field with a velocity  $\vec{v}$ , is described by the following equation:

$$\frac{d}{dt}(m\vec{v}) = \vec{F}_{\text{Lorentz}} = q\vec{v} \times \vec{B} \quad (3.1)$$

## Mode (1): RILAC + RRC + (stripper2) + fRC + (stripper3) + IRC + SRC

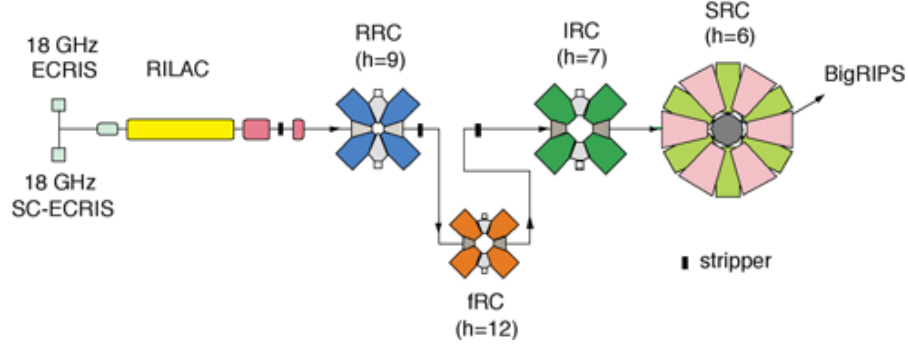


**Figure 3.1:** A schematic diagram of the RIBF heavy-ion accelerator system. RILAC+ RRC+ (stripper2) + fRC+ (stripper3)+ IRC+ SRC is used for the RI-beam  $^{78}\text{Kr}$  generation at 345 MeV/u with 350 pA. The process can be run in different modes depending on the desired outcome [63].

When  $\vec{B}$  and  $\vec{v}$  are uniform and perpendicular to each other, and the Lorentz force acts like a centripetal force ( $|\vec{F}_{\text{Lorentz}}| = mv^2/\rho$ ), then the trajectories moves in the magnetic field with the bending radius  $\rho$ . The magnetic rigidity,  $B\rho$ , results in:

$$B\rho = \frac{p}{q} \quad (3.2)$$

where the  $p$  is the momentum of the ion and is equal to  $mv$ . Thus,  $B\rho$  is specific for each ion depending on its velocity and mass. At relativistic energies  $m = m_0\gamma$  and in this case the momentum,  $p$ , can be written as;

$$p = m_0\gamma v \quad (3.3)$$

$$\gamma = \sqrt{(1 - \beta^2)^{-1}} \quad (3.4)$$

Here,  $\gamma$  is the Lorentz factor with  $\beta=v/c$  and  $c$  is the speed of light. Under these transformations,  $B\rho$  is proportional to the mass over charge ratio,  $A/q$  of the respective ion:

$$\frac{A}{q} = \frac{B\rho}{c\beta\gamma} \quad (3.5)$$

Hence, in a given magnetic field  $B$ , the radius of the curvature  $\rho$  defines the track of the particles. Depending on their mass and charge, by measuring the trajectories, the particles can be spatially separated by  $A/q$  and can be dispersed by the magnetic field to select a certain range of magnetic rigidities.

### 3.1.3 BigRIPS Fragment Separator

The production, selection and identification of the beam isotopes are performed in BigRIPS separator [60]. The BigRIPS fragment separator is composed of two stages. It starts with the primary target at the focal plane F0 and ends at F7 before the secondary target. The total path length of the fragment separator is 77 m. A schematic view of the beam line and the separator is shown in Figure 3.2.

The first stage, from the F0 to the F2 focal plane, is used for the production and separation of radioactive beams, while the second stage is used for the further separation and identification. Along both parts, in order to choose the isotopes of interest among the fragmentation products, a series of magnets, slits and degraders are used.

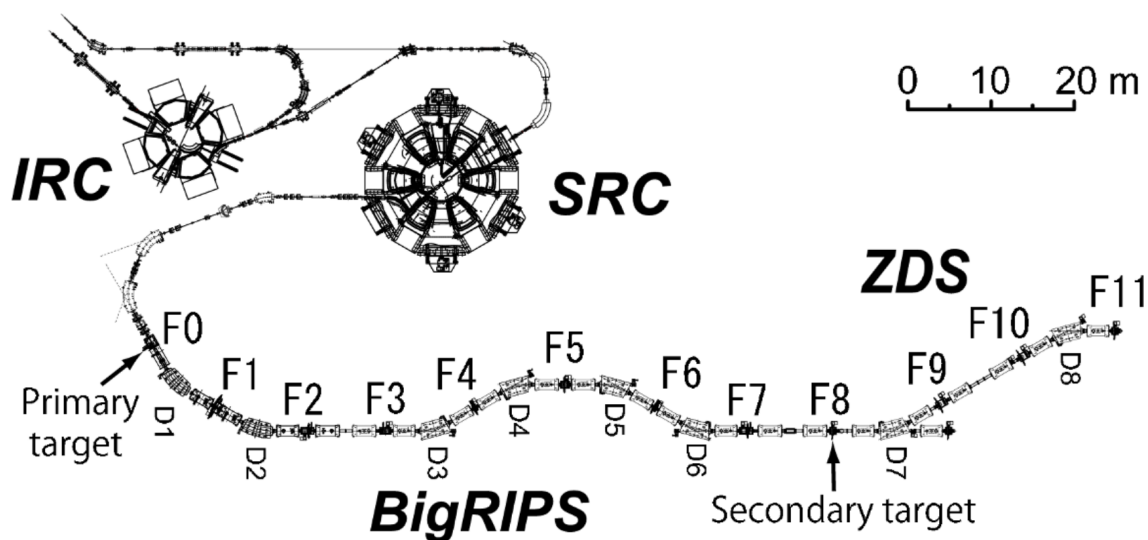


**Figure 3.2:** A schematic view of BigRIPS from F0 to F8 and the Zero Degree spectrometer from F8 to F11 focal planes. The secondary beam production takes place from focal plane F0 and the secondary targets of the present experiments were mounted at F8 [64].

The first stage of the BigRIPS has a  $80\text{ mrad}$  horizontal and  $100\text{ mrad}$  vertical angular acceptance. It consists of four superconducting quadrupoles (STQ, STQ1, STQ2, STQ3) and two dipole magnets (D1, D2). The primary target is placed at the momentum dispersive focal plane, at F0. At focal plane F1, a wedge-shaped Al degrader is used to provide an isotopic separation and an isobaric purification of the isotopes. The first dipole magnet provides a magnetic rigidity selection. Nuclei are selected by a slit at the exit of the first dipole magnet. After  $B\rho$  or  $A/q$  selection, nuclei pass through a wedge-shaped degrader installed at the momentum dispersive focal point F1. In the wedge shaped degrader, the ions experience an energy loss, depending on their nuclear charge  $Z$  as well as their position, hence, it allows compensation for the momentum dispersion for a given isotope. After passing the second magnet D2, slits placed at its exit select the ions with a certain  $B\rho$ . In the end, with this two stages selection of  $B\rho$ , ions can be separated by  $A/q$  as well as  $Z$  from the primary beam. Finally, the selected isotopes are transported to the achromatic focal plane F3.

The second stage of the BigRIPS starts with the achromatic focal plane F3, and consists of eight quadrupole and four dipole magnets with bending angles of 30 degrees. Along the second stage, F4, F5 and F6 focal planes are momentum dispersive while last focal plane F7 is doubly achromatic. The maximum magnetic rigidity in this stage is  $9\text{ Tm}$ . This part is mainly dedicated to the further separation and particle identification

of the different isotopes by measuring their charge and mass using the  $B\rho - \Delta E - ToF$  method. A 2 mm thick aluminum degrader is placed at F5 for the further purification of the beam by removing fragmentation products closer to stability. In this second stage of the BigRIPS separator, beam line detectors are used to measure the Time-of-Flight, energy loss, and particle trajectory. Parallel Plate Avalanche Counters (PPAC) are placed at F3, F5 and F7 to deduce  $B\rho$  position measurements. The energy loss is measured by using an ionization chamber placed at F7 and the information on the velocity of the particles between two focal planes are extracted by using plastic scintillators placed at F3 and F7 to determine the Time of Flight (ToF).

At the end of the BigRIPS, after selection and identification, the secondary beam is impinged on the secondary target placed at the focal plane F8, beginning of the ZeroDegree Spectrometer, with an energy of around 175 MeV/u.

#### 3.1.4 ZeroDegree Spectrometer

The reaction residues are identified and separated in the Zero Degree Spectrometer (ZDS). It starts with an achromatic focal plane at F8 and consists of six quadrupole and two dipole magnets bending the spectrometer by 30 degrees and ends at the doubly achromatic F11 focal plane with a momentum dispersive F9 focal plane in between. The total length of the ZDS is 36 m from F8 to F11. The angular acceptance of the spectrometer is horizontally 90 mrad and vertically 60 mrad. The identification of reaction products is done in the same way as in BigRIPS by employing the  $B\rho - \Delta E - ToF$  method. The time of flight is measured between the plastic scintillators at F8 and F11. PPACs along the beam line are used to track the trajectories of the particles and finally at F11, an ion chamber is used in order to measure the specific energy loss.

## 3.2 Beam Line Detectors

For the identification of each particle passing through the beam-line and the determination of their energy and travel path, a set of detectors are needed. This section is dedicated to the description of these detectors used along the beam-line in these experiments, including the electronics and the signal processing.

### 3.2.1 Parallel Plate Avalanche Counters

Parallel Plate Avalanche Counters (PPACs) are used for the tracking of the particles and to define the beam profile. A precise determination of the position and the angle of the particles along the beam line is necessary for an accurate beam tracking and the reconstruction. As the beam position and number of particles are extracted by PPAC measurements in each focal plane, it is of major importance to achieve a high PPAC efficiency for the experiment. PPAC units are placed at the focal planes F3, F5, and F7 in BigRIPS and at F8, F9 and F11 in the ZDS. Figure 3.3 illustrates the schematic view of a delay-line PPAC. Two PPACs, called A and B, are placed in each focal plane and each PPAC consists of two cathode plates connected to the delay-lines and an anode plane

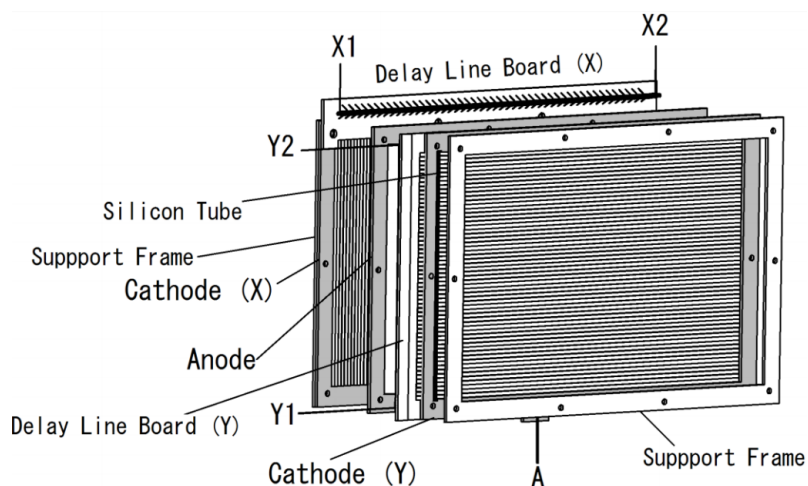


**Figure 3.3:** Schematic view of a delay-line PPAC [65].

in between at a distance of  $4\text{ mm}$ . Usage of double PPAC enables to measure the angle of the trajectory. The cathode plates have an active area of  $240 \times 150\text{ mm}^2$  consisting of  $2.4\text{ mm}$  wide strips. Five signals are obtained from each PPAC, one from the anode and 2 from each side of the cathode planes that are used for the time and charge information. The position information of the hits is deduced in two dimensions  $(x,y)$  by using the cathode signals of the X and Y strips that are oriented at  $90$  degrees to each other and the time difference between left and right signals. Each PPAC unit has a double PPAC inside and the unit is filled with  $\text{C}_3\text{F}_8$  gas at  $10\text{ torr}$  pressure during the operation. More detailed information about the PPACs can be found in reference [65].

Signal processing is performed as follows: The PPACs were operated with a bias voltage varying from  $700\text{ -}780\text{ V}$ , supplied to the anode. The anode signal has about  $13\text{ ns}$  rise time and about  $400\text{ mV}$  amplitude. After the preamplifier, PPAC signals are amplified by using fast linear amplifiers before splitting them in order to have signals for time and charge information. A linear FanIn/FanOut module was used to split the signal that was sent to a Constant Fraction Discriminator (CFD) module. Finally, the charge signal was fed into a charge sensitive Analog to Digital Converter (ADC) and the time signals were sent to a Time to Digital Converter (TDC).

### 3.2.2 Plastic Scintillation Detectors

The velocity of the ions along the beam line is deduced from ToF measurements, using fast plastic scintillation detectors. These scintillators are built from a BC-420 scintillation material coupled to HAMAMATSU H1949 Photo Multipliers (PMTs) at both sides. Each PMT gives one signal that is split into two analog signals to record the energy loss and the timing information of each hit. The time signal is fed into the TDC module after the Leading Edge Discriminator and the energy signal is sent to a charge sensitive module. The charges collected by the PMTs at both sides of the plastic material are related to the position of the particle hits due to the attenuation of the lights inside the scintillation

material before they arrive at the PMTs. The relation between the collected charges and the interaction position  $x$  is defined by the following equation:

$$x = \frac{\lambda}{2} \ln(q_1/q_2) \quad (3.6)$$

where  $\lambda$  is the attenuation length of light in the scintillation material,  $q_1$  and  $q_2$  are the charges measured in the left and right PMTs respectively. Therefore, position dependent corrections of the timing information are possible. Plastic scintillators are located at the focal planes F3 (1 mm thick) and F7 (2 mm thick) in BigRIPS and the thickness of the plastic material is both 1 mm for those located at F8 and F11 in ZDS. The time of flight is then calculated as:

$$ToF = \frac{L}{\beta c} \quad (3.7)$$

$L$  corresponds to the flight path length,  $\beta = v/c$ , where the  $c$  is the speed of light and  $v$  is the velocity of the particle.

### 3.2.3 Ionization Chamber

A Tilted Electrode Gas Ionization Chamber (TEGIC) is used at F7 and F11 to determine the atomic number of the fragments in the beam by measuring their energy loss. The ionization chamber consists of twelve anode and thirteen cathode planes enclosed in an aluminum chamber filled with Ar-CH<sub>4</sub> gas. All cathode planes were connected together and anodes were read-out in couples. At the end six signals are used from each ionization chamber. These signals were sent to the spectroscopic amplifier. The output of the amplifier was then sent to the QDC module. More detailed information about the TEGIC, including technical aspects, can be found in reference [66]. A schematic view of the TEGIC is given in Figure 3.4. As can be seen, the electrode plates are tilted by 30 degree to reduce the number of electron-hole recombinations. In this setup, there are two ionization chambers located at focal plane F7 in BigRIPS and at F11 in ZeroDegree.

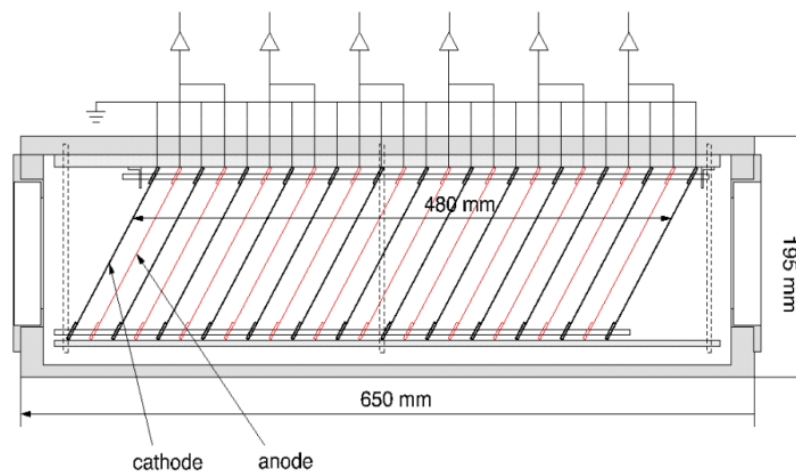


**Figure 3.4:** The schematic view of TEGIC [66].

The working principle of ionization chambers is as follows: The charged particle moving through a gas interacts with the electrons of the gas and loses energy. This interaction excites or ionizes the gas atom leading to an energy loss of the traveling particle. Since the number of created electrons is proportional to this energy loss, these electrons can be collected by using an electric field and used to determine the energy loss. This energy loss depends on the atomic number of particles with  $Z^2$  and their velocity. The mean energy loss of the ions per distance is given by the Bethe Bloch formula [28]:

$$-\left\langle \frac{dE}{dx} \right\rangle = \frac{4\pi}{m_e c^2} \frac{nz^2}{\beta^2} \left( \frac{e^2}{4\pi\epsilon_0} \right)^2 \left[ \ln \left( \frac{2m_e c^2 \beta^2}{I(1-\beta^2)} \right) - \beta^2 \right] \quad (3.8)$$

where the  $\beta = v/c$  for a particle with speed  $v$ ,  $c$  is the speed of light and  $\epsilon_0$  the vacuum dielectric constant, charge  $e$  and energy  $E$ , traveling distance  $x$ , electron number density  $n$  and mean excitation potential  $I$ ,  $e$  and  $m_e$  the electron charge and rest mass, respectively.

### 3.3 Gamma Spectroscopy

After the interaction with the target, excited nuclei emit  $\gamma$ -rays in their de-excitation process. At this point, highly efficient  $\gamma$ -ray spectrometers for high-precision detection of these  $\gamma$ -rays are needed. Gamma ray detection with germanium or scintillation materials is a well established analysis tool applied in many fields of physics. The goal is usually to achieve the highest detection yield in the shortest measurement time with the best possible energy resolution. The energy resolution of Ge detectors is much better than that of scintillators. However, scintillators have a higher efficiency in the detection and they offer better timing than Ge detectors. Additionally, Ge detectors are very expensive, require a complex infrastructure and are quite fragile. Nevertheless, they are needed for the experiments investigating high spin states. If there are few  $\gamma$ -rays emitted from the de-excitation of the nucleus, high efficiency is needed more than resolution. Therefore, in the experiments outlined in this thesis, a scintillator array was used for the detection of  $\gamma$ -rays.

#### 3.3.1 In-Beam Gamma Spectroscopy

Gamma-ray radiation emitted by a nucleus in motion, is detected in the laboratory system with a different energy than the actual transition energy in the self frame of the nucleus due to the Doppler effects. Therefore, the measured energy has to be corrected based on the emission angle and the particle velocity. The amount of shift in energy can be calculated via the following formula:

$$E_0 = E_{lab} \gamma (1 - \beta \cos \theta) \quad (3.9)$$

where  $E_0$  is the real de-excitation energy in its self frame,  $\beta$  is the in-flight velocity,  $E_{lab}$  is the energy measured by the detector,  $\theta$  is the angle between the direction of motion of the emitter and the detector,  $\gamma$  represents the Lorentz factor and  $\theta$  denotes the angle with respect to the direction of motion of the nucleus. The plot in Figure 3.5 illustrates the magnitude of the Doppler effects depending on the angle.

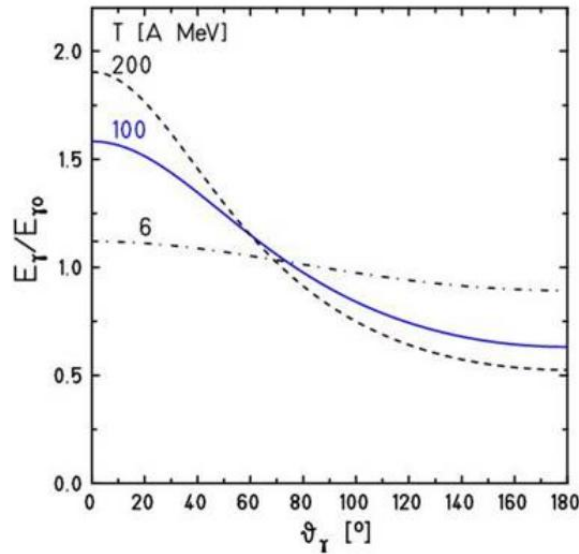


**Figure 3.5:** Ratio of the photon energy in the laboratory frame to the photon energy in the rest frame of the projectile versus the laboratory angle for different energies [67].

The Doppler effect leads also to a broadening of the measured  $\gamma$ -ray spectrum. Doppler broadening is caused by the inaccurate angle determination mainly due to the limited opening angle of the detectors and the velocity spread caused by the energy variation of the recoils. In order to minimize the broadening of the transition lines in the Doppler corrected energy spectrum, the first interaction point of the gamma-ray in the detector has to be determined precisely. The effectiveness of the Doppler correction is proportional to the precision of the hit position determination which is limited by the uncertainty on the velocity and angle. Usage of the large number of detectors at large distances also improves the correction of this effect but affects the efficiency of the measurement.

At present, these arrays are built up by using Scintillators or Ge detectors. The AGATA in Europe [68] and GREINA in the USA [69] are the most powerful examples of today spectrometers as Germanium arrays. The CEASAR scintillator array at MSU composed of 192 CsI(Na) crystals [70], the DALI2 in RIKEN [2] and PARIS a high resolution scintillator array for medium and high energy  $\gamma$ -rays built from novel scintillator material LaBr<sub>3</sub>(Ce) [71] are examples for  $\gamma$  detection arrays built up by using scintillators.

### 3.3.2 DALI2 Gamma Detector Array

The DALI2 is a  $4\pi$   $\gamma$ -ray detector array placed around the beam line at the reaction target in order to measure the de-excitation by  $\gamma$ -rays of reaction products [2]. It is composed of 186 rectangular shaped NaI(Tl) crystals from Saint-Gobain, Bicron and Scionix, all coupled to the Hamamatsu R580 and R1306 model PMTs. Table 3.1 shows the combination of different type of DALI2 scintillators and the layout of the configuration is shown in Figure 3.6.

**Table 3.1:** Variety of DALI2 scintillators used to build the array.

Company	Number	Crystal size (mm)	PMT Diameter $\Phi$
Scionix	66	80 x 40 x 160	38
Saint-Gobain	88	80 x 45 x 160	38
Bicron	32	61 x 61 x 122	51

Generally, it is important to cover all angles around the reaction target to increase the detection efficiency. The array is expected to have  $\sim 25\%$  full energy peak efficiency and  $\sim 10\%$  energy resolution for 1 MeV  $\gamma$ -rays with  $\sim 0.5c$  velocity.

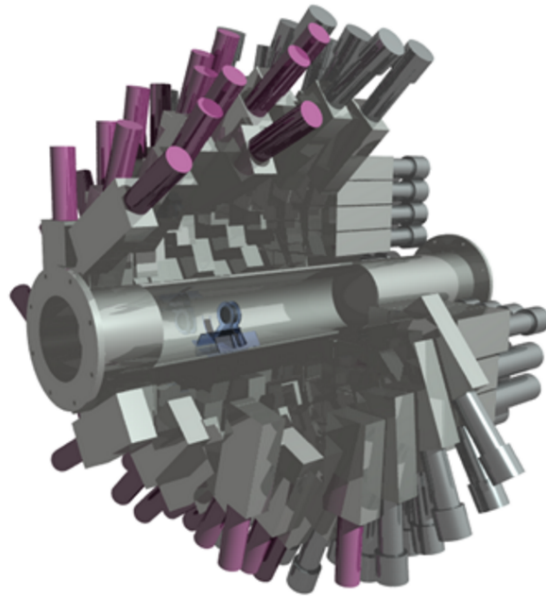


**Figure 3.6:** An insight view of the DALI2 detector array. In total 186 crystals surround the reaction target around the beam pipe.

In the case of in-beam spectroscopy, since the relativistic velocity of the particles results in a Lorentz boost towards forward angles, coverage of the forward angles becomes very important. At relativistic energies, the Lorentz boost plays a major role in increasing the detection efficiency and the energy resolution at forward angles. Polar angular coverage of the DALI2 is obtained from GEANT4 simulations. It ranges from 15.4 to 170 degrees for the geometric center of the crystals. The radius of the array around the beam-line increases with decreasing  $\theta_\gamma$  detection angle and then decreases again. This configuration was chosen to increase the add-back efficiency for  $\gamma$ -rays scattered between the crystals until they are fully absorbed.

The Compton-scattering process has a significant cross section. If a  $\gamma$ -ray leaves the crystal after such a scattering process, the measured energy is not the full energy of the

emitted photon but only a part of it. For reconstruction of the energy of these  $\gamma$ -rays, measured values in neighboring detectors are added in an add-back procedure. This is performed for the detectors within a certain distance, if they are in a common time window. The determination of this add-back distance is explained in Section 3.5. As a starting step, the crystal with the highest energy deposition is chosen and the smaller energies from surrounding crystal within a chosen add-back distance are added. Most frequently, the largest energy deposited is at the first interaction point of the  $\gamma$  ray, it has been assumed that this point lies in the crystal that measured the largest contribution to the sum. The position of this crystal then is used the Doppler correction.

The atomic background needs to be considered while performing  $\gamma$ -ray spectroscopy below about  $400\text{ keV}$  energy since it limits the observation due to overlapping energies. This is one of the major challenges, especially in Coulomb excitation experiments. Since, at these small energies, the atomic background cross sections can reach several  $kb$ , which is orders of magnitude larger than typical Coulomb excitation cross sections. The low-energy  $\gamma$ -rays are mostly caused by the atomic process called Bremsstrahlung, the interaction between the incoming beam and target electrons. Materials with high atomic numbers are generally used as a shielding to reduce the low energy atomic background caused by X-rays and low-energy  $\gamma$ -rays. A reduction is caused by the attenuation of  $\gamma$ -rays inside the shielding material. In the repeated experiments  $1\text{ mm}$  Pb and Sn plates were used as a cover around the beam pipe, where the reaction target was placed, and the energy threshold for the  $\gamma$ -ray detection was set to about  $50\text{ keV}$ .

The signal processing of the DALI2 array was performed as follows: During the experiment, 184 NaI(Tl) were biased out of 186. No signals were obtained from the other two detectors due to broken PMTs. The amplitude of the raw signal from the preamplifier of the PMT was measured to be around  $-1\text{ V}$  with a  $4\text{ }\mu\text{s}$  rise time and  $80\text{ }\mu\text{s}$  fall time. This signal was fed into a Caen N5688 model Spectroscopic amplifier. One of the two outputs from here was fed into a Caen V785 ADC. The range of the ADC is set to  $4000\text{ keV}$  corresponding to an amplitude of the signal fed into this ADC of  $1\text{ V}$ . The other output signal, from the fast output, was fed into a CAEN V812 CFD module. One of the outputs from the CFD module was fed into a CAEN V1190 model Multi Hit Time to Digital Converter (MHTDC) module to get the time information and the other output was used to create the  $\gamma$ -ray trigger as all the signals were in logical OR condition.

### 3.4 Performed Experiments

A set of Coulomb excitation and inelastic reactions were performed to identify the  $B(E2)$  values of  $^{72,70}\text{Kr}$ ,  $^{70}\text{Br}$  and  $^{68}\text{Se}$  isotopes. After the separation and particle identification process in BigRIPS, these isotopes were delivered in-flight at relativistic energies and bombarded onto a secondary target. A different Au and Be targets were used in order to scatter these radioactive isotopes. The Au target was chosen due to high atomic number to increase the probability of electromagnetic excitation. The Be target was used in order to increase the probability of nuclear excitation. The nuclear interactions can result in the excitation of higher spin states while the electromagnetic interaction is limited to the low excited spin states.

**Table 3.2:** *Settings of the performed experiments.*

	Setting 1	Setting 2	Setting 3	Setting 4
Centered BR	$^{72}\text{Kr}$	$^{72}\text{Kr}$	$^{70}\text{Kr}$	$^{70}\text{Kr}$
Secondary Target	$^9\text{Be}$	$^{197}\text{Au}$	$^9\text{Be}$	$^{197}\text{Au}$
Centered ZDS	$^{71}\text{Kr}$	$^{72}\text{Kr}$	$^{70}\text{Kr}$	$^{70}\text{Kr}$

Four different BigRIPS and ZeroDegree settings were used for the experiment. These settings are listed in Table 3.2. In the first setting,  $^{72}\text{Kr}$  isotopes were centered in BigRIPS and  $^{71}\text{Kr}$  was centered in ZeroDegree to study the inelastic scattering and knock-out reactions with a  $3.80(1)\text{ mm}$   $^9\text{Be}$  target. In the second setting, the  $^{72}\text{Kr}$  isotope was centered in BigRIPS and ZeroDegree for the Coulomb excitation on a  $0.200(8)\text{ mm}$  thick  $^{197}\text{Au}$  target. For the third setting,  $^{70}\text{Kr}$  isotopes were centered in BigRIPS and ZeroDegree for the inelastic scattering and knock-out reactions using a  $^9\text{Be}$  target. In the last setting, the  $^{70}\text{Kr}$  isotope was studied in the same way as the second setting, Coulomb excitation on a  $0.500(4)\text{ mm}$  thick  $^{197}\text{Au}$  target. The thicker Au target was chosen to account for the limited beam time in order to increase the  $\gamma$ -ray yield. The drawback was an increased angular straggling prohibiting a proper angular cut.

The number of the  $atoms/cm^2$  in the target is calculated by,

$$N_{target} = \frac{\rho L N_A}{M_t} \quad (3.10)$$

where  $L$  is the target thickness in  $mm$ ,  $\rho$  is the target density  $g/cm^3$ ,  $N_A$  is the Avogadro number given as  $6.02 \times 10^{23}$   $atoms/mol$  and  $M_t$  is the target mass in  $g/mol$ . Properties of the targets that were used in the experiments are listed in Table 3.3.

**Table 3.3:** *List of targets used in different settings.*

Target	Thickness [ $mm$ ]	Areal Density [ $g/cm^3$ ]	$N_{target}$ [ $atom/cm^2$ ]
$^{197}\text{Au}$	0.5	0.996	$0.118 \times 10^{22}$
$^{197}\text{Au}$	0.2	0.405	$0.295 \times 10^{22}$
$^9\text{Be}$	3.8	0.703	$4.623 \times 10^{22}$

Inelastic scatterings were studied by gating on the same isotopes in BigRIPS and ZeroDegree Spectrometers. Additionally, knock-out reactions were performed mainly to investigate excited states of  $^{70}\text{Kr}$  and  $^{71}\text{Kr}$  isotopes for the first time. All of the possible reaction channels were studied in detail, especially the one or two neutron knock-out from  $^{72}\text{Kr}$  and neighboring channels in the region. The content of this thesis includes only the inelastic reaction channels from each setting.

### 3.4.1 Trigger Configuration

In this section, the trigger conditions applied for the DAQ are explained. The trigger is set to select a subset of events to be read-out from the detectors. Each detector in the beam-line has an independent trigger made of a logical OR of time signals. In each setup used for the experiments, the main trigger was created from the timing signals of the plastic scintillators by feeding them into the logic coincidence module in AND condition. As the main trigger, the F7 plastic signal was chosen. This signal was split and sent to a rate divider to downscale (DS) it and create the F7DS trigger condition. A downscale factor is set to improve the data collection by reducing the dead time of the DAQ, since the counting rate in the BigRIPS part is much higher than ZeroDegree. F7DS events were assigned as beam events and used to identify the number of particles arriving to the secondary target. This scaling factor is set separately dependent on the experiment and factors are given in the table at the end of this section. Before the F7DS was created, the F7 signal was divided into two, and used to create the trigger from F7 and F11 signals as  $F7 \times F11$ . Afterwards, the  $F7 \times F11$  signal was put in coincidence with  $\gamma$  trigger from DALI2. This signal then creates the  $F7 \times F11 \times \gamma$  trigger. Trigger events from DALI2 corresponded to at least one NaI crystal hit and the PPACs were not part of any triggers and but they were recorded for each event. In this way, individual triggers were combined to obtain the main trigger signal for the data acquisition system. With the scaler module, the system dead time is calculated from the number of not gated and gated events. The trigger rate was limited around the 1 kHz in order to avoid large dead time.

## 3.5 Monte Carlo Simulations

The Monte-Carlo simulation code for DALI2 was developed using the GEANT4 package [72]. It includes the geometry of the DALI crystals, the beam pipe, absorbers, and the target holder. The beam profile was additionally modeled to reproduce the experimental energy and angular emittance. Energy thresholds and resolutions of the individual detectors were modeled from source measurements as well. The simulated data was analyzed the same way as the in-beam data, as Doppler correction was performed. The simulated transitions were obtained as a response function which was then fitted to the experimental spectra to obtain the  $\gamma$ -ray yield. Performed Geant4 simulations are explained in detail in reference [73]. The simulation has three steps that considers different physical processes. They are called Event Generator, Event Builder and Reconstructor, respectively.

In the first part, the beam and target species are described as an input file in order to simulate the interaction process. This input file includes the energy and the position of the beam onto the target, species of the target and its thickness, energy loss of the beam along the target, transition energy and the lifetime of the simulated excited state. The target thickness and the lifetimes of the excited states effect the line shape of the measured peak from the detected  $\gamma$ -rays. The beam energy in front, and the energy loss along the target was calculated using the ATIMA [74] code. The energy spread of the

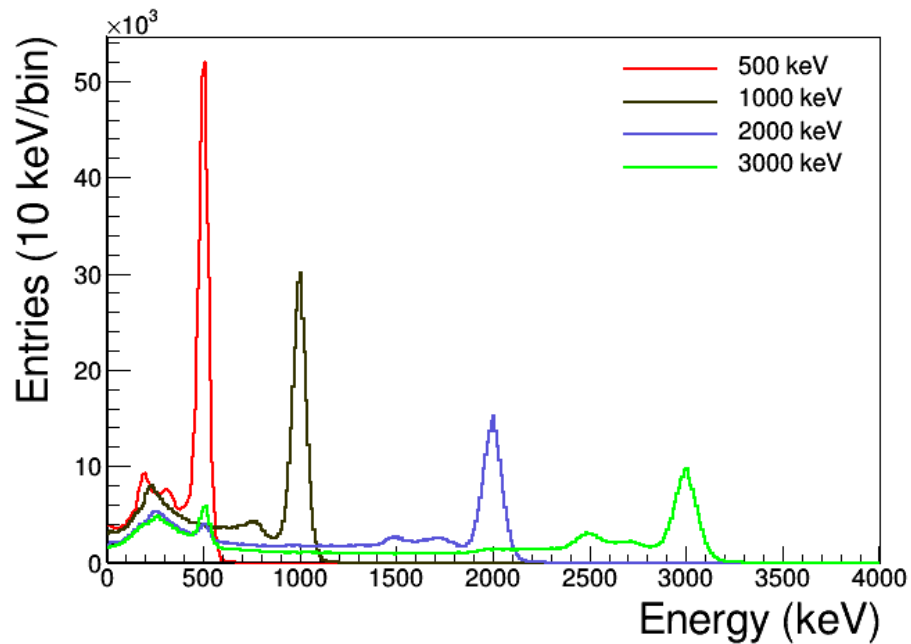
projectile was modeled using a Gaussian distribution to reproduce the experimentally measured distribution. The first step of the simulation creates the Doppler shifted  $\gamma$ -rays event-by-event and the simulated ejectile velocity at the time of emission.

After the simulation processes this information, in the second step, the DALI2 geometry with respect to the target, resolution of individual detectors, thresholds and absorbing materials such as housing, shielding and the beam pipe are included. An additional offset is added for the target position. This value is extracted from the technical drawings of the F8 focal plane and the placed detectors, combined with the mechanical measurements of the distances after mounting the beam-pipe and the target. The energy resolution of the detectors is the experimentally measured intrinsic resolution of each crystal. With all the given information, the detection of the emitted  $\gamma$ -rays is simulated. The information of the beam-target interaction is taken from the first step and detection of the emitted  $\gamma$ -rays from this interaction is simulated.

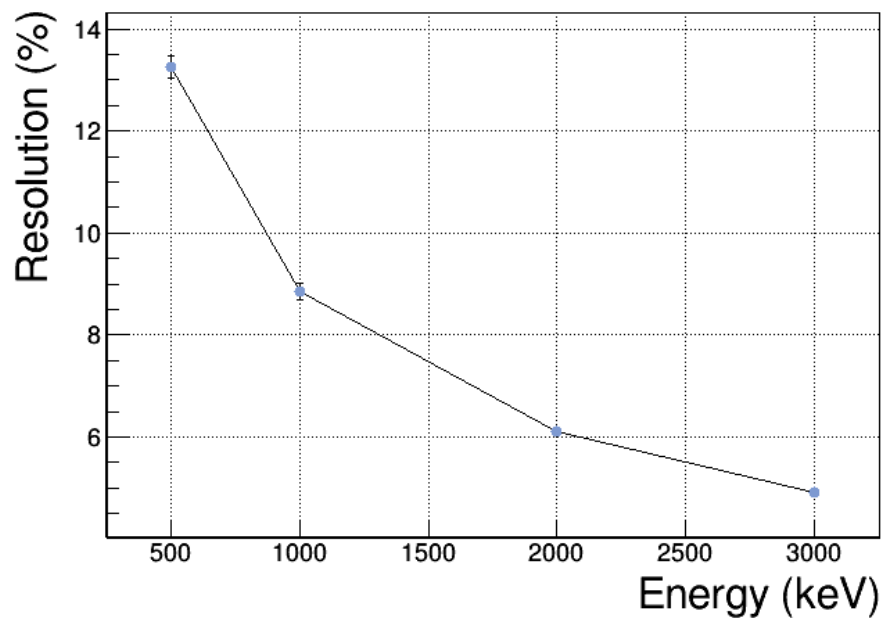
In the last step, the results are collected for the analysis procedure. It is done in the same manner as for the experimental data. The Doppler correction is applied, different add-back procedures are tested. Additionally, in this step the first interaction points are also extracted from the simulation to be used in the analysis of the experimental data as the geometrical center of each crystal. Precise polar angle determination is needed in order to achieve a more accurate Doppler shift correction. Thus, the simulation results were obtained in the same way as the experiment results. Finally, they were used to fit with the experimental data to deduce the number of emitted  $\gamma$ -rays and calculate the cross-sections of the studied interactions. Obtained cross sections were then used to extract the  $B(E2)_{\uparrow}$  values of relative transitions. This procedure is explained in Section 5 in detailed.

The response function of the DALI2 array for different  $\gamma$ -ray energies are shown in Figure 3.7(a), and the decrease in the relative resolution is given as a function of the energy of the emitted  $\gamma$ -ray is shown in (b). Obtained values are in agreement with the measured values that are given in Table 4.6. Since the add-back procedure is also applied both in the experimental data and in the simulation, its effect is represented here. The simulation was used in order to test the add-back parameters such as add-back distance. This procedure is employed to recover the scattered  $\gamma$ -rays from neighboring crystals and increase the peak efficiency. In each event, energy depositions in multiple crystals are summed within certain distances to recover additional full-energy  $\gamma$  events. Figure 3.8(a) shows the effect of this procedure for different distances at an energy of  $1000\text{ keV}$ . Figure 3.8(b) shows the effect of the add-back procedure on the absolute photo-peak efficiency depending on the energy of emitted  $\gamma$ -ray. It increases for higher energies, the comparison in the figure is done with  $15\text{ cm}$  add-back distance. It was optimized as  $15\text{ cm}$ , since the improvement in the photo-peak efficiency saturates and becomes less significant in higher distances. Within this thesis, for the analysis of the  $\gamma$ -rays,  $15\text{ cm}$  add-back distance was chosen in all the steps. The consistency of the cross-section results is checked and approved for different add-back distances.

Finally, the simulations are benchmarked with the measured data in order to define the agreement between them. More detailed information about the benchmark can be found in Section 4.5.2.

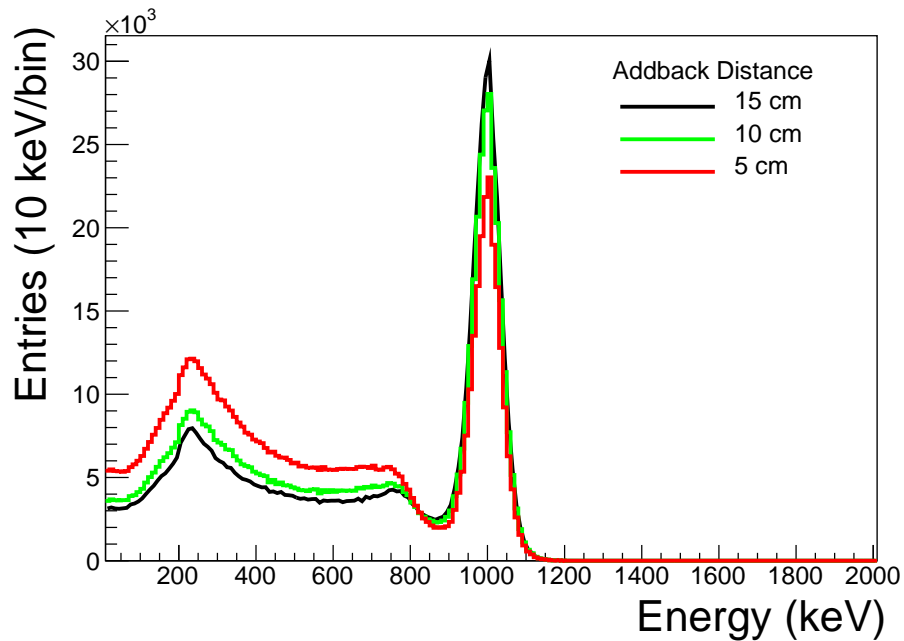


(a) Simulated  $\gamma$ -ray energy spectrum for arbitrary energies.

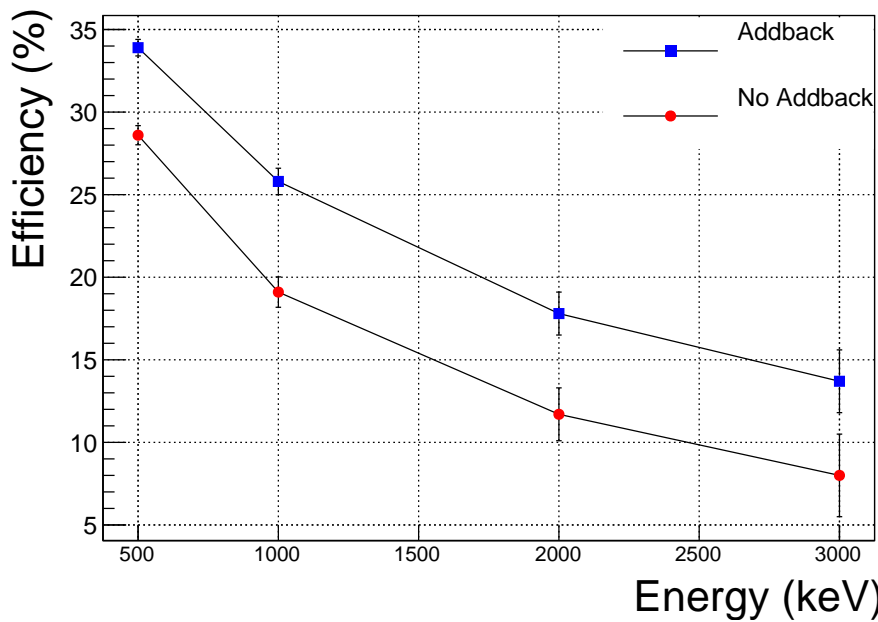


(b) Dependence of the energy Resolution in FWHM(%) on the energy of the transition.

**Figure 3.7:** a) Comparison of simulated spectra for  $10^6$  emitted  $\gamma$ -rays at different energies. The red distribution shows the emitted  $\gamma$ -rays with 500 keV energy, purple is 1000 keV, blue is 2000 keV and green is 3000 keV. b) Simulated  $\gamma$ -ray peaks with DALI2 array show a decrease in the resolution depending on the energy.



(a) Photopeak efficiency for different addback distances.



(b) Photopeak efficiency for different transition energies using 15 cm addback distance.

**Figure 3.8:** a) Simulated results shows that the photopeak efficiency changes with different add-back distances. Red distribution is for the 15 cm, yellow is for 10 cm and purple line is for 5 cm add-back distance. b) The absolute photo-peak efficiency comparison is shown with and without add-back as a function of emitted  $\gamma$ -ray energy. Add-back distance is chosen as 15 cm.

# 4

## Data Analysis

In this chapter the data analysis procedure is explained in detail. As a first step, the energy, position and time calibration of each beam-line detector is performed which enables the energy loss, position and time-of-flight information of each particle. Selection and identification of the ions in the beam cocktail are done on an event-by-event basis, using the  $B\rho - \Delta E - ToF$  method. The atomic number of the particles is deduced from the  $\Delta E - ToF$  relation, while  $A/q$ , the mass to charge ratio, is determined using the magnetic rigidity  $B\rho$ . Following this, various gates are applied in order to reject background events, and the particle identification resolution is improved by correcting for trajectory dependent effects. In order to measure the reaction cross section, the number of detected particles in ZDS has to be identified correctly considering the efficiency and transmission losses along the beam line. Therefore, transmission rates are identified for each selected isotope. For the determination of the differential cross section, the scattering angle of the excited particles at the target is reconstructed using a set of PPACs. In this chapter, the Cartesian coordinate system  $x,y,z$  is used such that  $z$  is defined as the beam axis,  $x$  as horizontal line with respect to the beam direction and  $y$  as the vertical axes.

Firstly, energy and time calibrations are performed. Doppler correction is applied to obtain the energy of the emitted  $\gamma$ -rays taking into account the velocity of the excited particles in-flight. Finally, Monte Carlo simulations are performed and the response function is used to fit the experimental  $\gamma$ -ray spectra. The simulations are benchmarked with the measurements by studying the efficiency of the system. The final numbers are then used to extract the Coulomb excitation and inelastic scattering cross-sections in Chapter 5.

### 4.1 Particle Identification

Particle IDentification (PID) is necessary to choose the isotope of interest in order to analyze a certain reaction channel and to define the number of incident particles on the target. In the BigRIPS and ZeroDegree Spectrometers the same identification method is used for the incident and scattered beam particles [75]. Trajectory reconstruction of the beam is performed using the positions and angles of the fragments deduced from the  $B\rho$  measurement performed by the position-sensitive PPACs, velocity of the particles are

determined using the plastic scintillators and Z information is from ionization chambers.

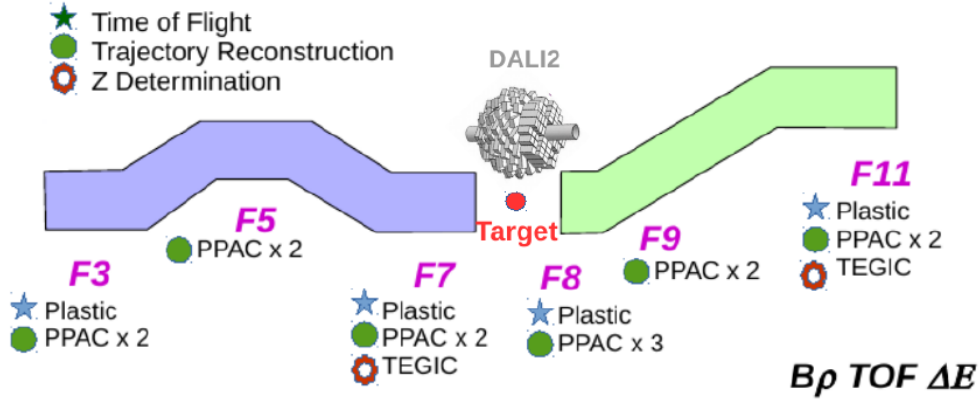


**Figure 4.1:** Schematic view of BigRIPS (blue part) and ZeroDegree (green part) Spectrometers, indicating the detectors used in each focal plane and the secondary target position.

The location of these detectors along the spectrometer is shown in schematic diagram in Figure 4.1. Detailed information about the usage of these components is given in following sections.

#### 4.1.1 Position Determination

Position measurements were performed using the PPAC detectors that is explained in detail in Section 3.2.1. Along the beam line, PPACs are placed at the F3, F5, F7 focal planes of BigRIPS and the F8, F9, F11 focal planes of ZeroDegree and are used to track the beam along the spectrometer.

To extract the position information, the cathode strips are configured in  $x$  directions for the front plate and  $y$  direction for the back plate (section 3.2.1). The two dimensional hit position is deduced from the time differences of these signals. The signals from the cathode are named  $T_{x_{right}}$ ,  $T_{x_{left}}$  and  $T_{y_{down}}$ ,  $T_{y_{up}}$ . The  $(x, y)$  position information of the particles are extracted from the following formula;

$$x = c_x \frac{T_{x_{right}} - T_{x_{left}}}{2} + X_{offset} \quad (4.1)$$

$$y = c_y \frac{T_{y_{down}} - T_{y_{up}}}{2} + Y_{offset} \quad (4.2)$$

where  $c_x$ ,  $c_y$  are the coefficients from the delay-line used for time to length conversion and  $X_{offset}$ ,  $Y_{offset}$  are the offsets that have to be taken into account to correct the arbitrary position with respect to the central trajectory. When there is a single hit on a PPAC, the sum of the time signals from left and right should have a narrow distribution, while the multi hit events would lead to smaller entry values compared the single hit ones. The deviating events can be removed from the analysis by applying a gate on the sum of these signals:

$$T_{sum\ x} = T_{x_{right}} + T_{x_{left}} \quad (4.3)$$

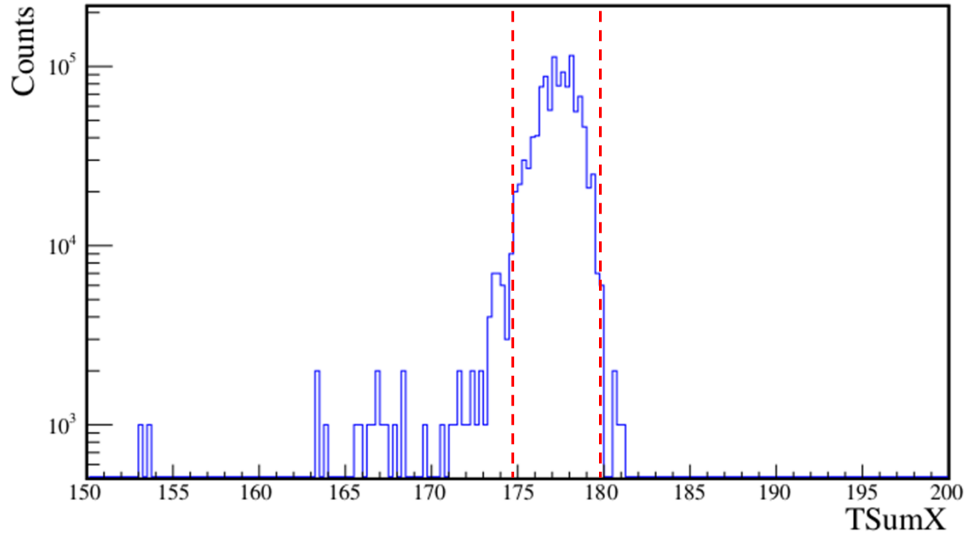


**Figure 4.2:** The example of  $T_{sum_x}$  [mm] from PPAC2A at focal plane F3 with the applied gate. The same procedure is applied also to  $T_{sum_y}$  signals.

$$T_{sum_y} = T_{y_{up}} + T_{y_{down}} \quad (4.4)$$

The signals are gated in order to reduce the background and the noise in the PPAC. All the signals from each plate are gated with a width of  $3\sigma - 4\sigma$  around the centroid of the peak as shown in Figure 4.2.

The efficiency of a PPAC depends on the atomic number of the isotopes. For this experiment, all of the efficiencies are calculated for the  $Z=36$  mass region. They are determined for each focal plane. Each focal plane has two double PPACs that enable measurement of the incoming angle of each individual ion, see chapter 3.3. In order to get the best efficiency at each focal plane, two PPACs are used in the OR condition. Each PPAC plate in a certain focal plane is considered as one PPAC and one hit in any plate is considered as a signal in this focal plane. The PPAC efficiencies are calculated by dividing the number of counts in each PPAC by the total number of triggered events in the ionization chamber that is placed at the end of each spectrometer. The efficiencies that we obtained during the experiments are given in tables in Appendix A.1 for all the focal planes. As it is seen in these tables, there is one PPAC plate with zero detection efficiency. This PPAC was turned off during the experiment due to too high beam intensity. Figure 4.3 shows the position of the  $^{70}\text{Kr}$  beam particles, gated in BigRIPS and ZDS, at each focal plane for a single run together with the number of ions passing through. These numbers agree with the efficiencies of the PPACs and the width of the beam at each focal plane is consistent with the applied slits.

#### 4.1.2 ToF Measurement

The ToF was measured with plastic scintillators placed along the beam line to determine the velocity of the particles,  $\beta$ , using equation 3.7. Besides measuring the time-of-flight, the plastic scintillators at F7 and F11 are also used as the trigger for the data acquisition. In the data analysis, the ToF information is extracted using the focal planes F5 and F7

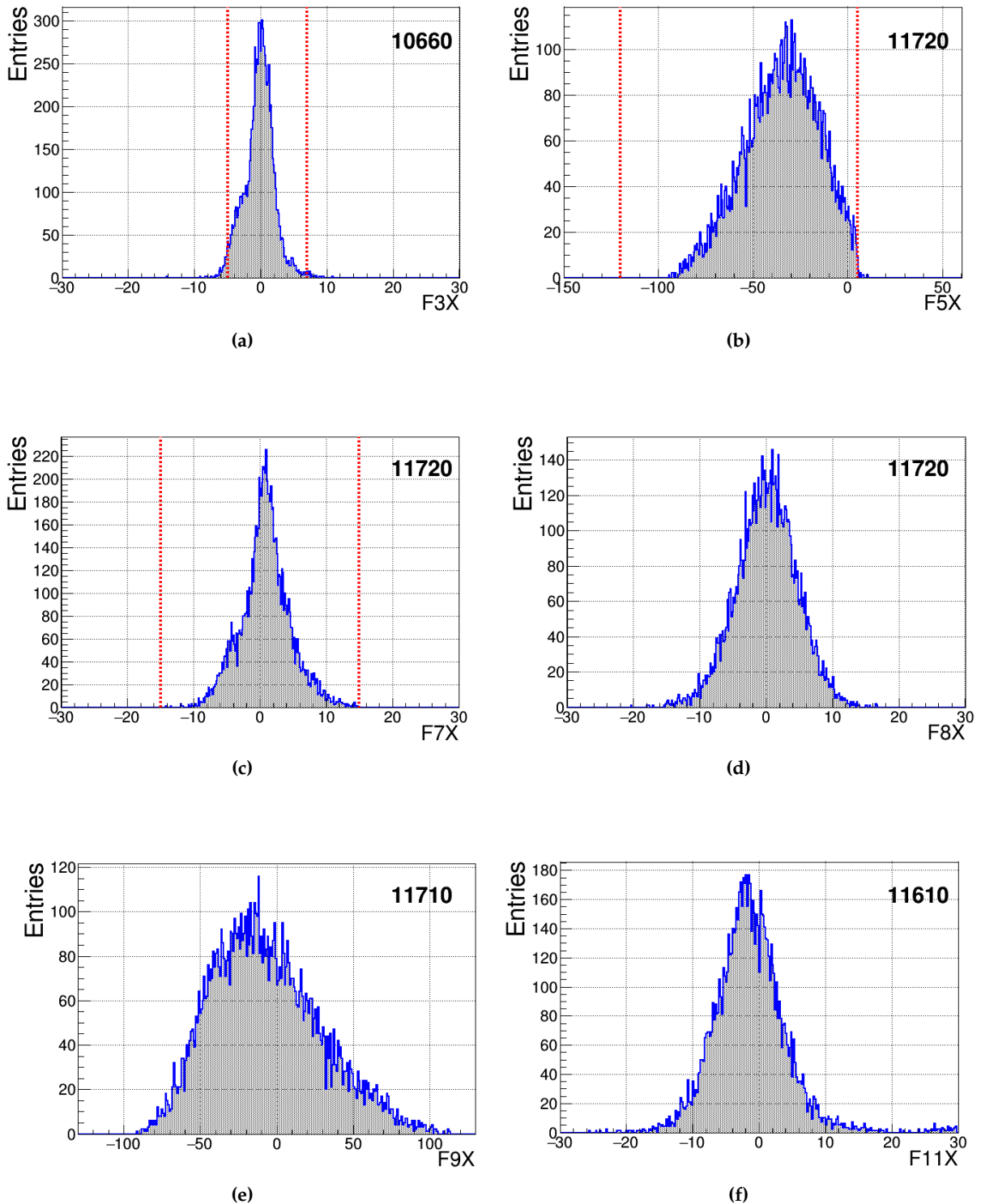


**Figure 4.3:** Horizontal positions (in mm) in the F3, F7, F8, F11 achromatic and F5, F9 dispersive focal planes for the  $^{70}\text{Kr}$  projectile and ejectile. The number of particles at each focal plane is indicated on the right top of the figures. Red dashed lines show the slits that were set at these focal planes.

for BigRIPS and F8-F9 for ZeroDegree by the following equations:

$$ToF_{BR} = T_{F7} - T_{F3} + T_{BRoffset} \quad (4.5)$$

$$ToF_{ZD} = T_{F11} - T_8 + T_{ZDoffset} \quad (4.6)$$

An absolute correction is done by matching the corresponding known  $A/q$  of the relative isotope to the nominal value. This additional time offset is introduced to correct for the unknown delays that are caused by the electronics and different cable lengths.

The efficiency of the plastic detector placed at F7 is assumed to be 100% since it defines the trigger events. Then, the relative efficiency is determined for the other plastic detectors corresponding to the one at F7. The number of gated events in each plastic detector is divided by the number of events in the reference detector. The total efficiency for particles reaching F11 at the end of the ZeroDegree spectrometer is found to be 99.99%.

#### 4.1.3 Atomic Number Determination

The atomic number  $Z$  is determined from the energy deposited in the ionization chamber and the velocity of the particles is extracted from the  $ToF$  measurement. A Gaussian fit to the data is performed to obtain the uncalibrated channel numbers. A linear calibration is performed between these ADC channels of the TEGIC spectrum and the known  $Z$  values of the isotopes, taking the energy loss into account. The same procedure was applied to all settings. After the calibration, a remaining dependency of  $Z$  on  $\beta$  was observed. A linear fit was performed to remove this dependence. Figure 4.4 shows the

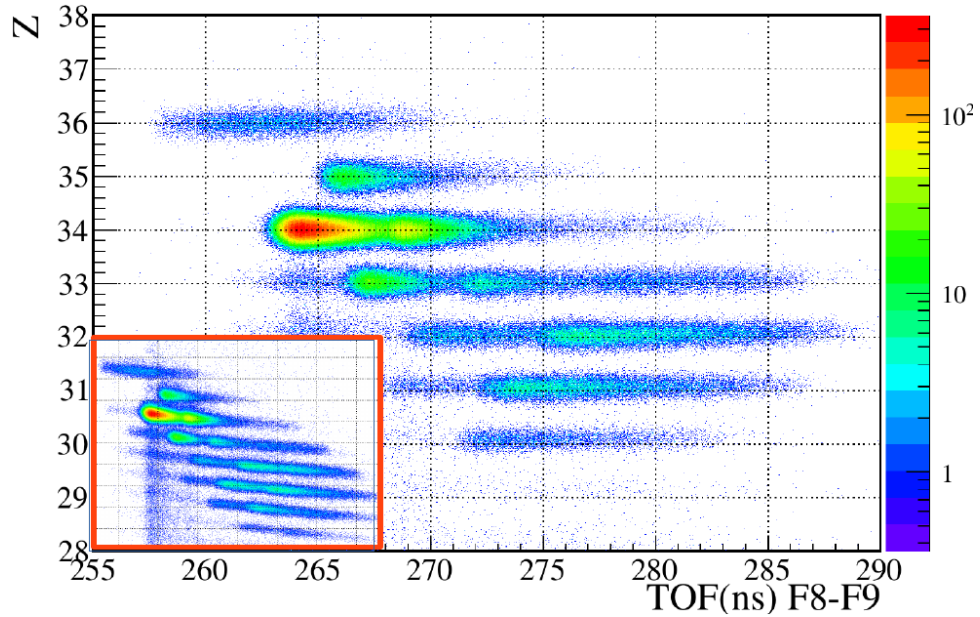


**Figure 4.4:** The corrected velocity dependence of  $Z$  in TEGIC placed in the ZeroDegree Spectrometer and the dependence before the correction is shown in the red box on left bottom.

relation between  $Z$  and  $ToF$  before and after this correction for each isotope in ZeroDegree. The same procedure was applied also for the BigRIPS part. After this correction, the sequence of the ions in the final PID plot, with same  $Z$  and different  $A/q$  value, were aligned.

The ionization chamber efficiency was determined in a similar way to the plastic efficiencies. For the TEGIC in F7, the number of events passing each cathode plane was divided by the total number of triggered events passing through the ionization chamber with the trigger condition F7DS. For the IC at F11, it was determined in a similar way by considering the trigger conditions F11 and F7. At the end, it was concluded that F7 IC has 99.88% efficiency while F11 IC has 99.91%.

#### 4.1.4 Particle IDentification (PID) of Ions

After the calibration of particle detectors along the spectrometers, the particle identification (PID) can be performed. As the PPAC efficiency at F3 was lower than the rest, different sets of focal planes were tested in the BigRIPS section. For the F3 - F7, F5 - F7 and F3 - F5 distances, PID plots were constructed and the number of particles detected passing through these focal planes were compared. Due to the low PPAC detector efficiency at the beginning of the BigRIPS spectrometer, the F5 and F7 focal planes were chosen to increase the number of detected particles and the resolution of the position determination. By eliminating the F3 focal plane from the PID, the number of detected particles were increased by only 2% compared to the case that it was included, but the resolution of the  $A/q$  was improved by approximately 30%. The resolution was obviously affected by the damage in the PPAC placed at F3 focal plane, caused by the high intensity of the particles.

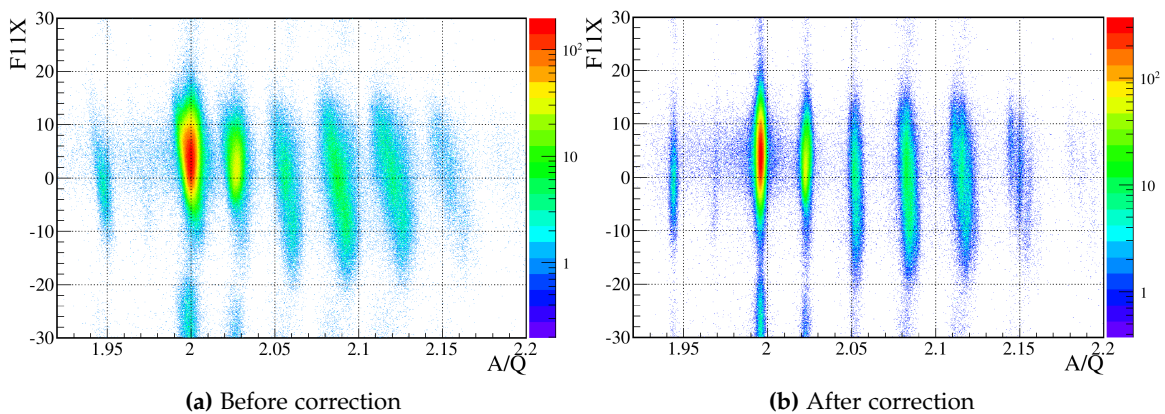


**Figure 4.5:**  $A/q$  position dependence at the F11 focal plane.

For the ZeroDegree spectrometer, the F8 - F9, F9 - F11 and F8 - F9 focal planes were tested for the analysis of the ejectiles. The difference in the total number of particles between choosing different focal planes in ZeroDegree was around 1%. The losses along the ZeroDegree were mainly caused by the creation of charge states. These charge states with

different  $Z$  and  $A/q$  values are created while an ion passes through the materials located along the beam-line. The best efficiency was obtained using the F8-F9 focal planes to extract the PID information. In addition, PPACs at F8 are used to construct the scattering angle of the ejectiles and thus rendering the particle identification at F8 crucial.

After the calibrations, further corrections are needed to improve the  $Z$  and  $A/q$  resolutions. The  $A/q$  value of each ion has to be independent of the measured angles and positions. To remove any dependence, optical corrections are applied as follows. The  $A/q$  value is plotted versus the angle  $A$  and position  $X$  at each focal plane for a set of isotopes. As an example, Figure 4.5 shows the F11 position versus the  $A/q$  value for the Kr isotopes, (a) position dependencies on measured  $A/q$  and (b) after these dependencies are removed. In order to remove these dependencies, the profile in (a) is fitted for the isotopes of interest with a polynomial function up to 3rd order in order to obtain the correction parameters. Using these parameters, the position and angle dependencies on  $A/q$  is removed and the resolution improved at this focal plane around 36% depending on the chosen isotope. Figure 4.5(b) shows the F11 position against the  $A/q$  value after the correction is applied. The corrections can only be optimized for one particular isotope, and therefore have to be done individually for different mass regions. Figure 4.6 shows this improvement on the  $A/q$  resolution at F11 focal plane, before (red line) and after (green line) the corrections for the production from  $^{72}\text{Kr}$  beam.

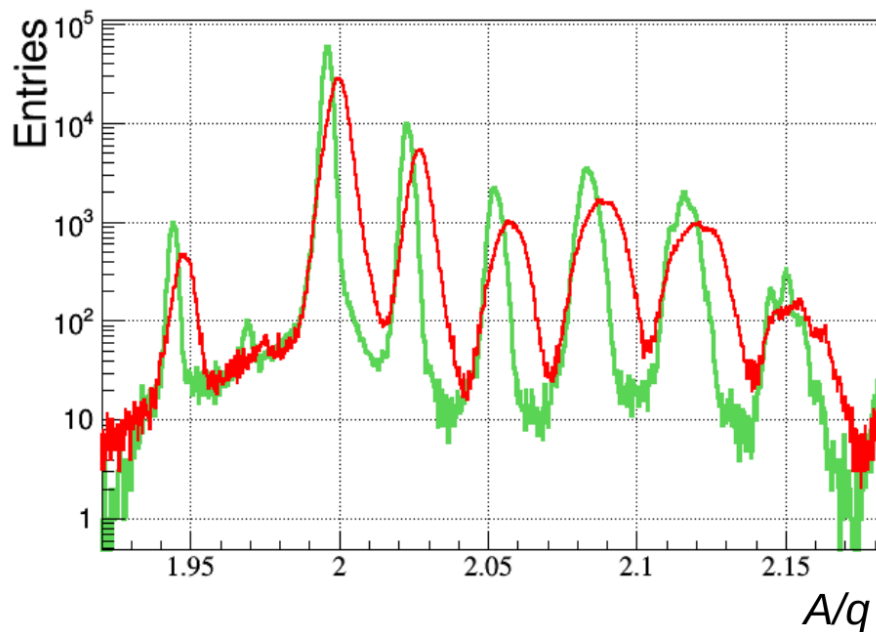
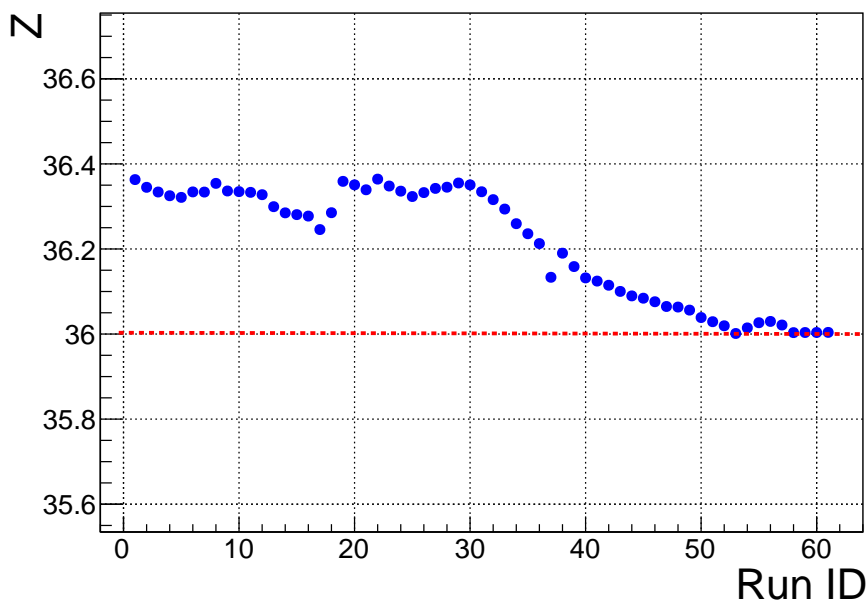
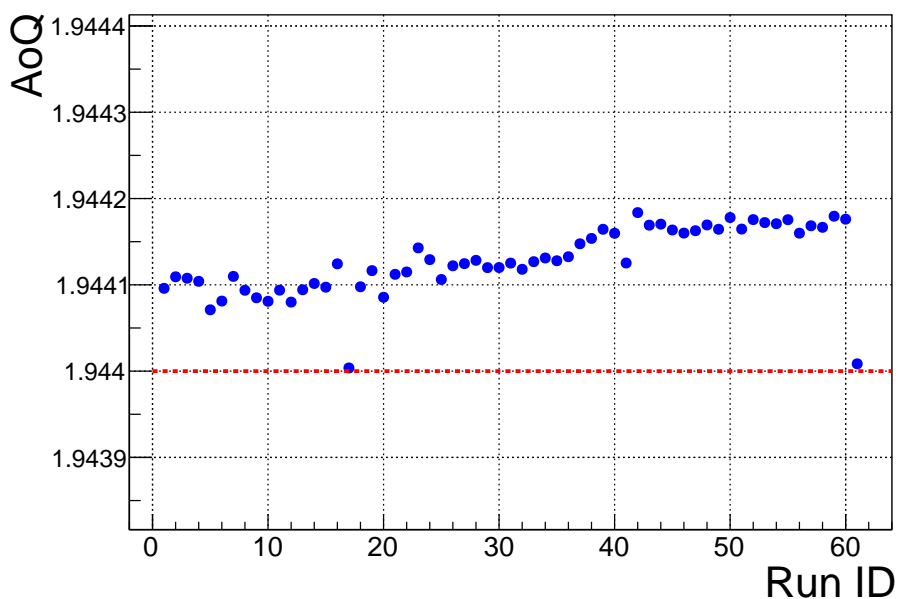


**Figure 4.6:** The  $A/q$  resolution was improved by around 36% after corrections on angle and position dependence. The plot shows the  $A/q$  of values measured  $Z = 36$  isotopes before (red line) and after (green line) these corrections.

After all these corrections were applied to the data, a gain shift was observed in  $A/q$  and  $Z$  values among the different runs. The shift in  $A/q$  is caused by a voltage change in the plastic scintillators, while the shift in  $Z$  values is due to pressure changes in the ionization chambers. These fluctuations in the TEGIC are mainly correlated with the varying temperature of the gas. The gain shifts were corrected by adding an additional



(a) Gain shift in Z values



(b) Gain shift in A/q values

**Figure 4.7:** Figure a shows the gain drift in Z values and figure b shows the gain drift in A/q. The red dashed line indicates the distribution after the correction.

offset value in the calibration. Figure 4.7 shows the Z and A/q values measured for  $^{70}\text{Kr}$  before the correction as a function of run number. All the data points were then shifted to the real values, shown as red dashed line. Larger fluctuations are due to the low statistics in the relevant run.

**Table 4.1:** The  $A/q$  and  $Z$  resolutions for the particle identification of  $^{70}\text{Kr}$ 

	$\sigma_Z$	$\sigma_{A/q}$
BigRIPS	0.15 (1)	0.0124(3)
ZDS	0.13 (2)	0.0351(3)

Obtained  $Z$  and  $A/q$  resolutions for the BigRIPS and the ZeroDegree spectrometers are given in Table 4.1. The uncertainties on the resolutions are the standard deviation of the measured resolution among different isotopes. The values given in the table are for the  $^{70}\text{Kr}$  on Au setting. The procedure was applied for all the settings individually.

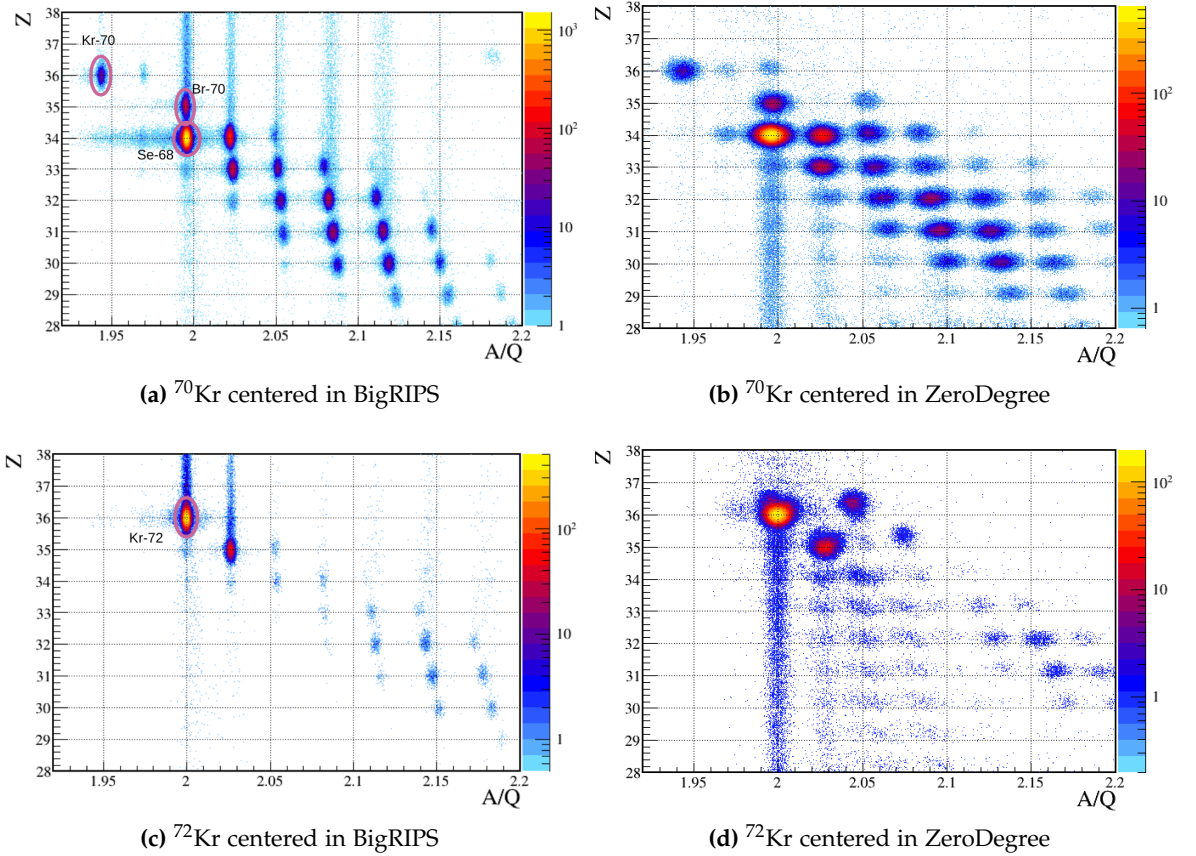


**Figure 4.8:** The  $A/q$  versus  $Z$  particle identification plot of Coulomb excitation setup. In the left side BigRIPS and on the right side ZeroDegree PID plots are given.

Finally, after multiple corrections, in order to achieve a good resolution in the PID plots, final gates were applied to chose the proper reaction channels. In Figure 4.8, typical PID plots for the Coulomb excitation experiments are shown. In plots a and b,  $^{70}\text{Kr}$ ,  $^{70}\text{Br}$  and  $^{68}\text{Se}$  were selected as an incoming beam and followed by the same channels as an outgoing beam after the Coulomb excitation with the 0.5 mm thick  $^{197}\text{Au}$  target. Plots

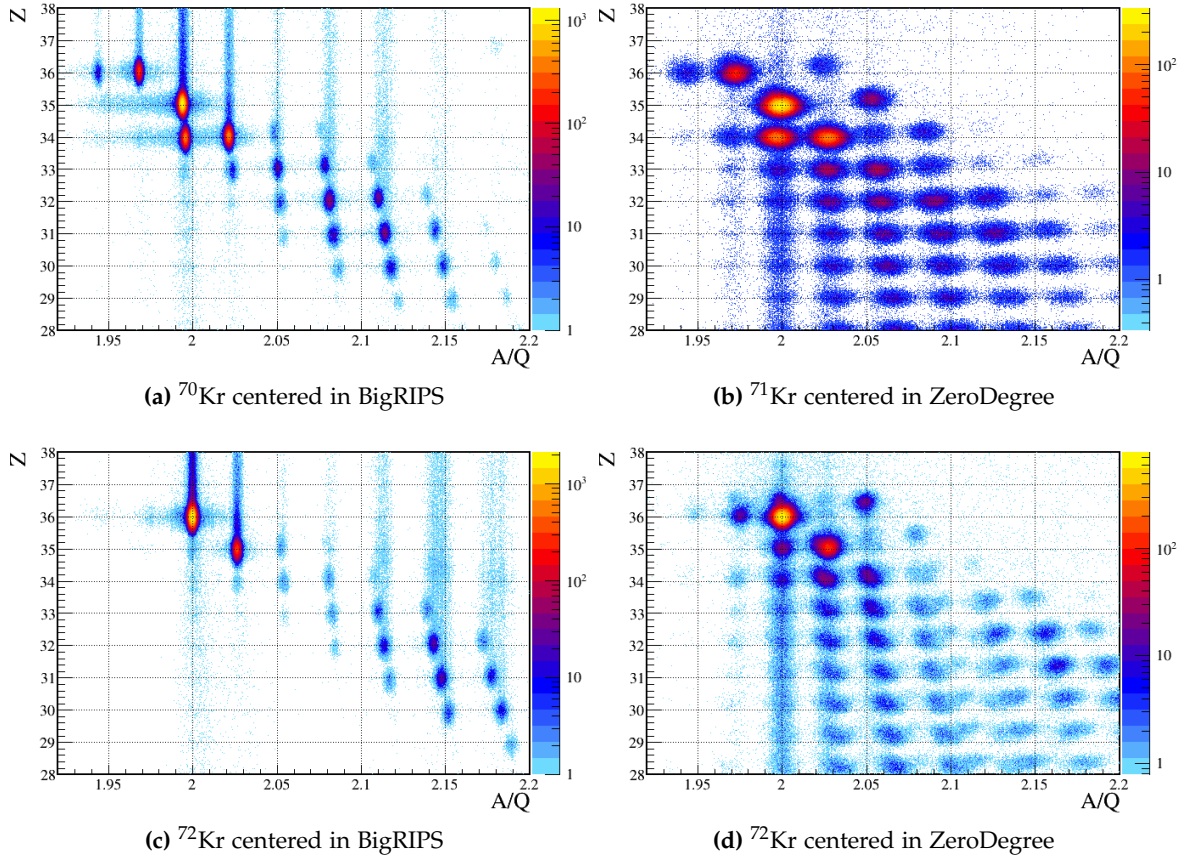


**Figure 4.9:** The  $A/q$  versus  $Z$  particle identification plot of the inelastic reactions setup. On the left side BigRIPS and on the right side ZeroDegree PID plots are given. The figures illustrate the full set of isotopes in these spectrometers.

c and d show the setting centered on  $^{72}\text{Kr}$  for the Coulomb excitation with the 0.2 mm thick Au target. In Figure 4.9, typical PID plots for the inelastic scattering of the same isotopes on a Be target is shown.

The applied gates were used in order to identify the number of incoming and outgoing particles in BigRIPS and ZeroDegree, with certain trigger conditions. This is important to calculate the cross sections for the respective reaction channels with  $\gamma$ -rays in coincidence. The number of particles in these gates was checked with the F7DS trigger condition and multiplied by the downscale factor. These numbers are given in the Table 4.2 for each setting. The first column shows the isotope gated as incoming and outgoing, the second one shows the type of the target, in the third column, the number of incoming particles is shown, multiplied by DS factor and the last column shows the number of outgoing particles with F11 trigger request, which could arrive up to the end of ZeroDegree Spectrometer, F11 focal plane.

**Table 4.2:** The number of selected isotopes of an incoming beam on the secondary target  $N_{BR}$  and the number of outgoing particles  $N_{ZD}$ .

Isotope	Target	$N_{BR}$ [ $10^5$ ]	$N_{ZD}$ [ $10^4$ ]
$^{70}\text{Kr}$	$^{197}\text{Au}$	31.334(56)	55.185(74)
$^{70}\text{Kr}$	$^9\text{Be}$	12.706(50)	6.099(25)
$^{70}\text{Br}$	$^{197}\text{Au}$	177.97(13)	269.98(16)
$^{70}\text{Br}$	$^9\text{Be}$	1292.53(51)	631.39(25)
$^{68}\text{Se}$	$^{197}\text{Au}$	1821.11(43)	852.75(53)
$^{68}\text{Se}$	$^9\text{Be}$	400.45(28)	186.88(14)
$^{72}\text{Kr}$	$^{197}\text{Au}$	1572.35(69)	1043.41(32)
$^{72}\text{Kr}$	$^9\text{Be}$	1757.72(94)	423.09(21)

## 4.2 Scattering Angle Determination

In Coulomb excitation experiments performed at intermediate energies, the cross-section for the excitation is a superposition of nuclear and electromagnetic contributions. The type of the interaction can be roughly distinguished by their scattering angle dependence (see Figure 2.6). Depending on the resolution and the angular straggling that is caused by the target thickness, these distributions are smeared out and may become not sensitive to the type of the interaction. In this case, a cut on small scattering angles, as done in other experiments is not enough to eliminate the nuclear excitation [5]. Ideally, a cut can be applied to a certain angle during the analysis to minimize the contribution of the nuclear excitation. Nevertheless, a theoretically calculated angular distribution has to be convoluted with the experimental resolution and the angular straggling.

In this section, the scattering angle reconstruction of the scattered particles is explained. The scattering angle of the particles is also needed to determine the differential cross section. As discussed before, the  $\gamma$ -ray spectrometer is placed around the secondary target and three PPACs are used as tracking detectors. The two PPACs are placed at the F8 focal plane, in front of the target, are used to track the beam and one PPAC that is placed behind the target is used to determine the scattering angle of the ejectiles.

The mechanical alignment of the PPACs was checked before the experiments with a laser alignment system. The system was set to reproduce the beam axis, and the PPAC behind the target was centered according to the laser spot. A schematic view of the PPAC positions and the target is shown in Figure 4.10. A further correction was needed for an accurate determination of the projectile direction of the particles. The angles of the incoming beam are calculated from the beam going through the PPAC1 and PPAC2

via the relation:

$$\theta_x = \tan^{-1} \frac{dX}{Z_2 - Z_1} \quad (4.7)$$

$$\theta_y = \tan^{-1} \frac{dY}{Z_2 - Z_1} \quad (4.8)$$

The two PPACs before the target were placed at  $-1273 \text{ mm}$  and  $-773 \text{ mm}$ , the target was placed at  $131 \text{ mm}$ , and the third PPAC was placed behind the target at  $1026 \text{ mm}$ , where  $0 \text{ mm}$  corresponds to the nominal focus. An empty target run was used to correct the alignment of the PPACs. The incoming trajectories are extrapolated to PPAC3 to align it with respect to the other two. For the production runs, with the target, the information from PPAC1 and PPAC2 is used to determine the  $x$  and  $y$  position at the target by extrapolating the hit positions at the F8PPACs. Setting  $Z_{tar}$  as the middle of the target, the  $X$  and  $Y$  positions are given by:

$$X_{tar} = X_1 + dX \frac{Z_{tar} - Z_1}{Z_2 - Z_1} \quad (4.9)$$

$$Y_{tar} = Y_1 + dY \frac{Z_{tar} - Z_1}{Z_2 - Z_1} \quad (4.10)$$

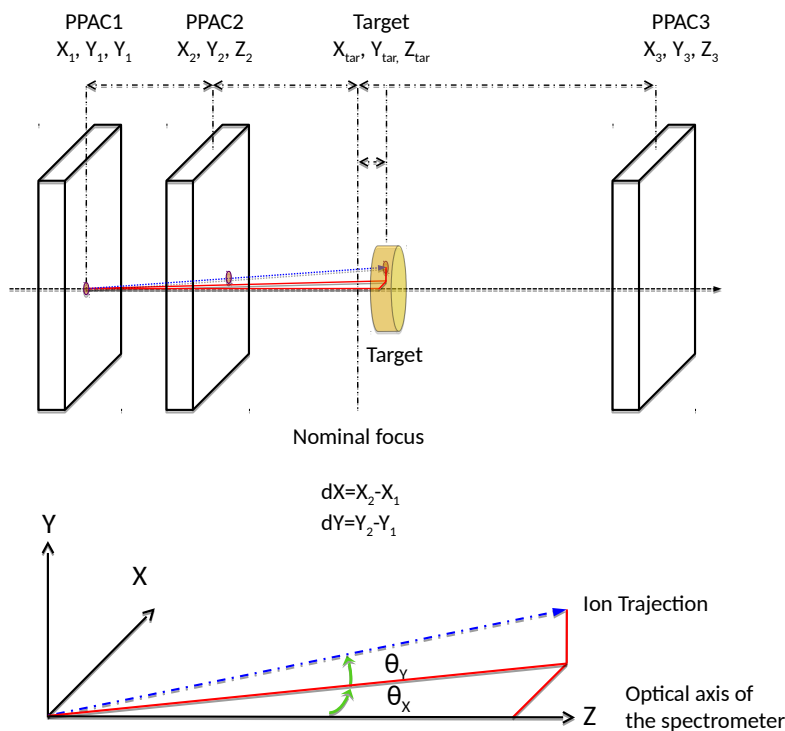


**Figure 4.10:** A schematic view of the scattering angle reconstruction of the ions using PPAC detectors located at focal plane F8.

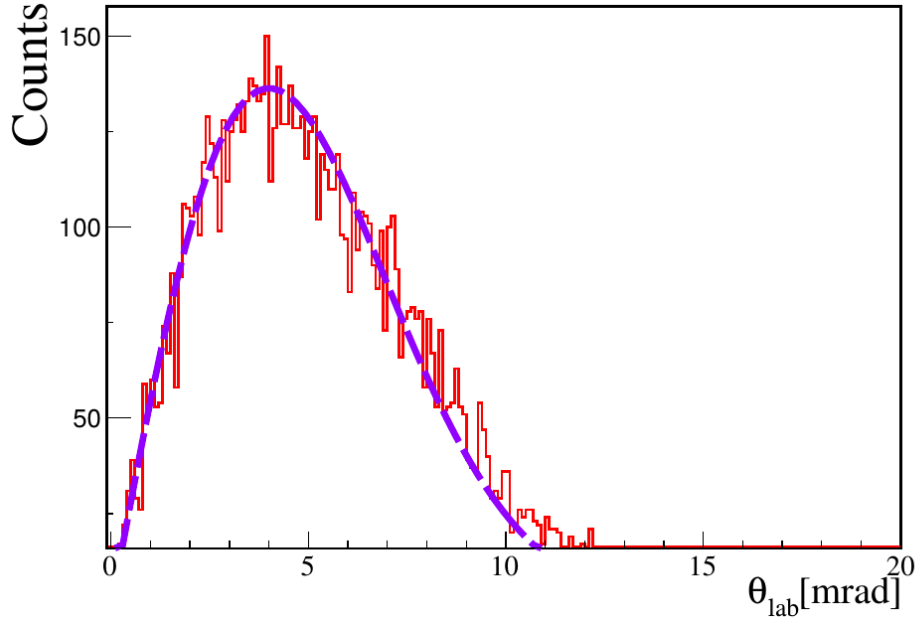


**Figure 4.11:** Scattering angle resolution for  $^{70}\text{Kr}$  isotope was determined using the empty target case, by gating on the  $^{70}\text{Kr}$  isotopes in BigRIPS and ZeroDegree Spectrometers. The red line shows scattering angle distribution, while the purple dotted line is fit to the data.

The scattering angle of the isotopes is then calculated event by event from:

$$\cos\theta = \frac{\vec{a} \cdot \vec{b}}{|\vec{a}| |\vec{b}|} \quad (4.11)$$

where the  $\theta$  is the scattering angle,  $\vec{a}$  is the direction of the incoming particle before the target and  $\vec{b}$  describes the direction of the outgoing particle after scattering off the target.

Determination of the scattering angle is important since it is related to the type and magnitude of the interaction. As explained before, the setup that was used in this experiments was not sensitive to this purpose, however it can be used for the high statistics case to measure the angular distribution and the angular transmission. The experimental scattering angle of the ion of interest was studied by gating on the specific isotope with both in BigRIPS and ZeroDegree Spectrometers. For each case, the angular resolution,  $\sigma_R$ , was determined to be around 2 mrad. Figure 4.11 shows the obtained scattering angle distribution for  $^{70}\text{Kr}$  with empty target case. During the experiment, the scattering angle is smeared by the angular straggling,  $\sigma_S$  in the target. This contribution was determined for each case by using ATIMA calculations. For each ion-target combination, obtained straggling is listed in Table 4.3. The effect of the target thickness on the angular straggling is clearly visible between the listed values.

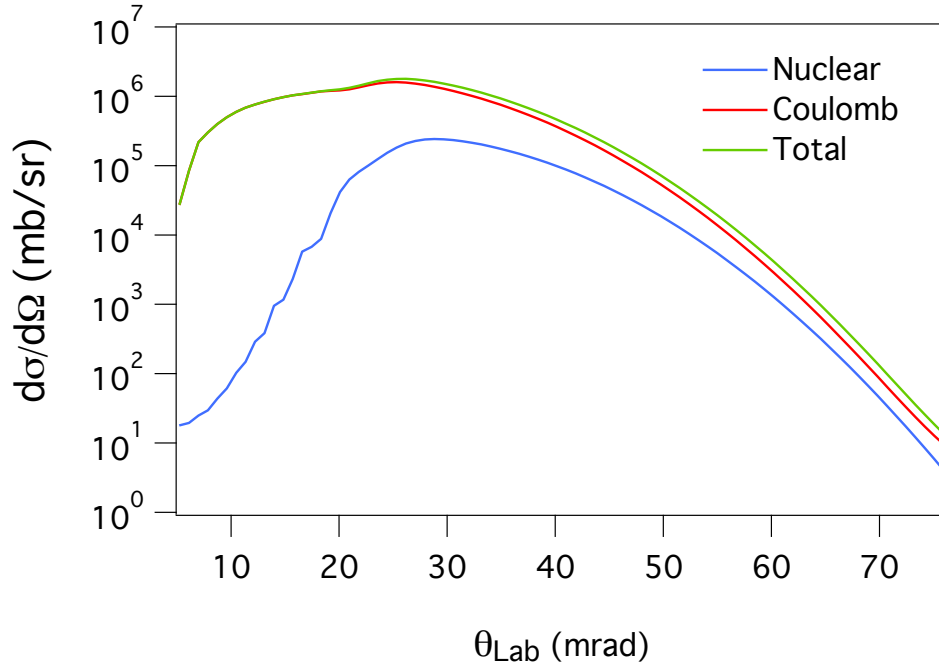


**Figure 4.12:** Calculated nuclear and electromagnetic differential cross-sections are convoluted with the angular resolution and the angular straggling.

**Table 4.3:** The measured angular spread with target  $\sigma_S$  are obtained by ATIMA calculation while the  $\sigma_R$  values are the scattering angle resolution with the empty target case.

Target	Empty	Be	Au
	$\sigma_R$ [mrad]	$\sigma_S$ [mrad]	$\sigma_S$ [mrad]
$^{70}\text{Kr}$	1.92(2)	2.97	10.9
$^{68}\text{Se}$	2.06(1)	2.90	10.7
$^{70}\text{Br}$	1.94(1)	2.99	11.0
$^{72}\text{Kr}$	1.42(1)	2.81	5.95

The calculated scattering angle distribution has to be corrected for these experimental limitations in order to be comparable with the experimental data. This correction was performed as the convolution of the theoretical distribution. The final angular distributions shown in Figure 2.6 are convoluted with this angular resolution and the straggling, and the result is given in Figure 4.12. As it is seen, after convolution, the angular distributions of nuclear and Coulomb excitation completely overlap, such that a gate on the scattering angle cannot be used to discriminate between the two interactions.

### 4.3 Particle Transmission through the Spectrometer

The transmission of the particles along the spectrometer can be affected by several reasons. In order to determine the cross section, particle losses along the spectrometer have to be determined. These are caused by the limited efficiency of the detectors, reactions in the detector materials, target or beam-line materials, angular and momentum acceptance of the spectrometer. Depending on the detector efficiency, the particle may not be counted even if it was transmitted. Particle detector efficiencies  $\epsilon_{det}$  are determined individually and values are given in Section 4.1.

The transmissions are determined by applying a cut to each isotope in BigRIPS and ZeroDegree. Each effect that can cause a loss in the particle transmission is studied separately. Taking into account all contributions, the transmission can be formulated with a relation between the number of particles in BigRIPS,  $N_{BR}$ ,  $\epsilon_{det}$  and the number of particles in ZeroDegree  $N_{ZD}$ :

$$N_{ZD} = N_{BR}\epsilon_{det}\epsilon_{ZD}\epsilon_{tar} \quad (4.12)$$

where  $\epsilon_{ZD}$  accounts for the transmission efficiency in the spectrometer and  $\epsilon_{tar}$  is for the efficiency through the target.

To identify the count rate effect caused by the beam-line detector efficiencies and the collisions with the detector materials, the ratio of the number of particles counted in BigRIPS and ZeroDegree is taken with the F7DS trigger condition. The losses in the detector material are determined with the empty target run. The momentum acceptance of the ZeroDegree spectrometer can be seen by plotting the distribution in the dispersive F5 focal plane as shown in Figure 4.13.a for  $^{70}\text{Kr}$ . A 94 % of the  $^{70}\text{Kr}$  nuclei are transmitted from F7 to F11.

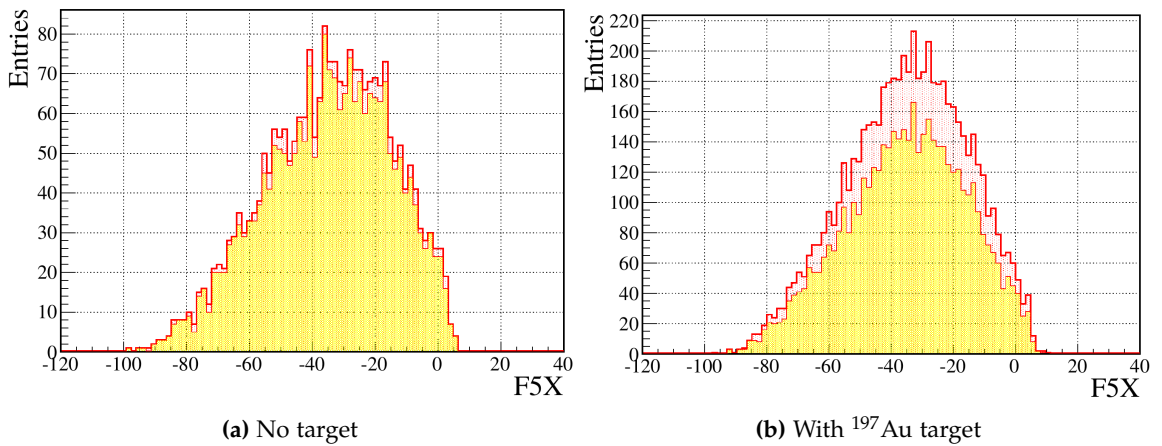


**Figure 4.13:** Comparison of the transmitted  $^{70}\text{Kr}$  isotopes along the beam line before and after the target is shown in the figure left and right, respectively. The red distribution shows the transmitted particles in BigRIPS while the yellow one shows the transmitted particles in ZeroDegree.

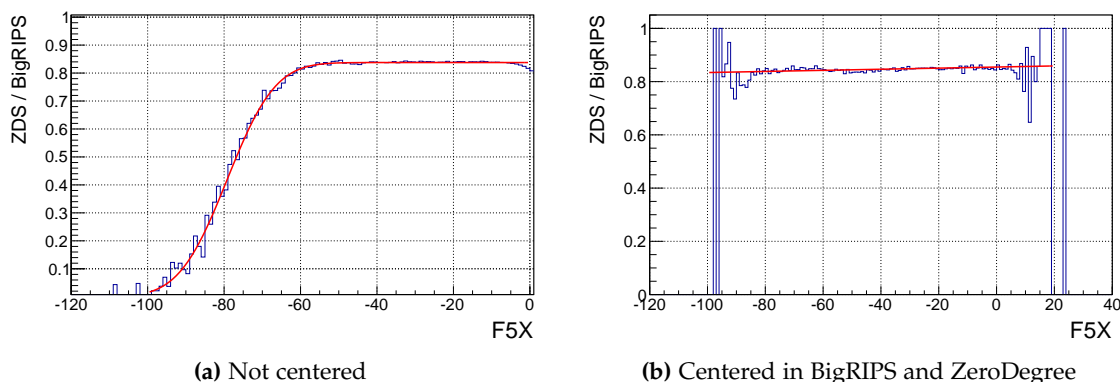


**Figure 4.14:** Ratio of the number of particles from ZeroDegree and BIGRIPS. The left plot is for  $^{70}\text{Br}$  reacting with the Be target and the right plot shows the case of  $^{70}\text{Kr}$  reactions with a Au target. The difference for the centered and not centered isotope is clearly seen.

The transmission depends on the gated isotope. To determine the losses caused by reactions with the target, the same procedure was repeated with the target runs and the rate was determined as 84.6% for  $^{70}\text{Kr}$ . The difference between the two cases is caused by the reaction with the target. Hence, the most important contribution to the transmission comes from losses in the target. The effect is shown in Figure 4.13.b, with the projection of the beam taken from the F5X focal plane. The red distribution shows the transmitted particles in BigRIPS and yellow shows the one with the gate on BigRIPS and ZeroDegree.

The losses caused by the reaction with the materials along the beam-line or by the efficiency of the detectors do not depend on the position. The dependence on the position comes from the transmission of the spectrometer. In general, less transmission occurs in terms of emittance at the edges of the beam spot, as the beam is more dispersed and not all the isotopes were centered in the spectrometers. The transmission can be corrected by determining the loss fraction as a function of the dispersive position. An empirical function is fitted to the distribution to evaluate the losses. Figure 4.14 illustrates this procedure for  $^{70}\text{Br}$  and  $^{70}\text{Kr}$  isotopes in plots a and b, respectively. The  $^{70}\text{Kr}$  isotope was centered in BigRIPS and ZeroDegree but  $^{70}\text{Br}$  was not. Therefore, one can judge the difference in both cases. As can be seen, for the  $^{70}\text{Br}$  case, the ratio is constant for about 60 mm on the top and then drops down at the edges. The constant part represents all losses which are not dependent on the momentum, angle and the position, which is the result of  $\epsilon_{det}$  and  $\epsilon_{tar}$ . The deviation is then due to the transmission of the spectrometer. This deviation differs depending on the chosen isotope. For the isotopes centered in BigRIPS and ZeroDegree, this effect is not observed.

The transmission has to be taken into account to get the absolute value of the cross section. The values representing the overall transmission factors, are obtained for all of the reaction channels and are studied individually with the F7DS trigger condition. The

numbers are listed in Table 4.4.

**Table 4.4:** Total transmission for selected isotopes in different settings, including all contributions to losses along the spectrometer.

Gated Isotope	Target	Transmission [%]
$^{70}\text{Kr}$	$^{197}\text{Au}$	84.6(2)
$^{70}\text{Kr}$	$^9\text{Be}$	80.1(6)
$^{70}\text{Br}$	$^{197}\text{Au}$	78.8(1)
$^{70}\text{Br}$	$^9\text{Be}$	83.31(4)
$^{68}\text{Se}$	$^{197}\text{Au}$	83.36(4)
$^{68}\text{Se}$	$^9\text{Be}$	79.51(8)
$^{72}\text{Kr}$	$^{197}\text{Au}$	90.5(1)
$^{72}\text{Kr}$	$^9\text{Be}$	82.73(6)

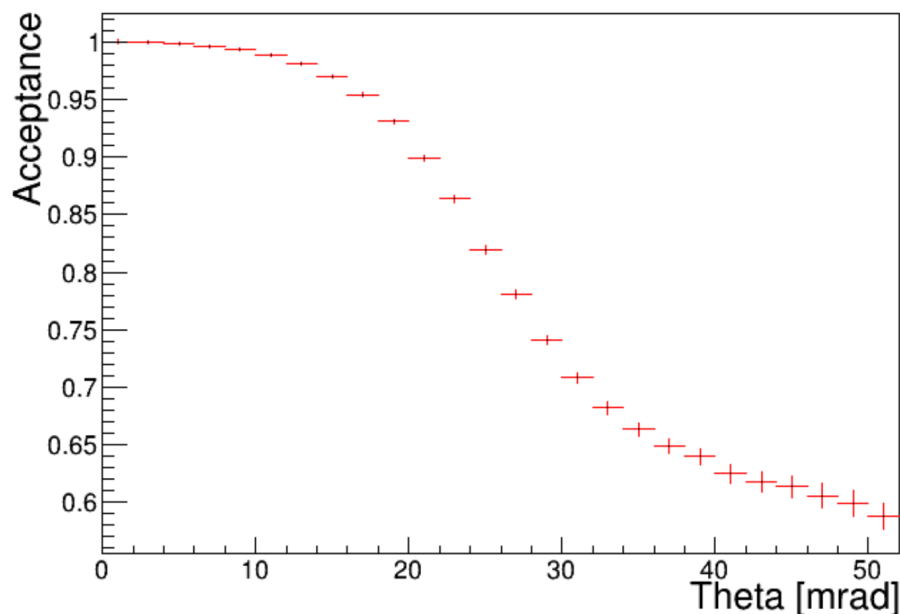


**Figure 4.15:** Angular acceptance of the ZeroDegree Spectrometer measured for gated  $^{72}\text{Kr}$  beam particles.

In order to study the angular acceptance of the spectrometer, position dependent and non-dependent effects have to be determined separately. Only with position dependent effects, the transmission is expected to be 100% at the center of the beam. It is assumed that the deviations through the larger angles are caused by geometrical reasons. The acceptance of the spectrometer depends on the momentum, position and angle of the particle. In order to determine the angular acceptance, the ratio of the particles in ZDS and BigRIPS is taken and corrected with the non-position dependent factors. The angular acceptance of the spectrometer is plotted as a function of the scattering angle in Figure 4.15. This deviation can be used to correct cross sections for the events at the

corresponding angle.

## 4.4 Velocity Determination of the Particles

Determining the beam particle velocity,  $\beta$ , in an accurate way is essential as it is used for the Doppler correction of the measured  $\gamma$ -ray transitions. The  $\beta$  value can be extracted from the experimental data by using the *ToF* and *B $\rho$*  (see section 4.1.2), then the energy loss in the target is calculated by the ATIMA code and inserted in the simulations to determine the  $\beta$  at the moment of decay.

It is not possible to precisely measure the real  $\beta$  value at the moment of decay. Nevertheless, it can be estimated in BigRIPS, before the target and in ZeroDegree, after the target, from the experimental data using the *ToF* detectors. However, after the particle is measured by the *ToF* detectors in ZeroDegree, it may undergo multiple scatterings in the thick target or extra energy losses along the beam line may occur. In this case, the *ToF* value will differ from its actual value, which results in giving a lower energy of the particle in the moment of decay. Conversely this value measured in BigRIPS would be higher than its real value since there are more energy losses after the plastic detectors. The experimentally determined  $\beta$  is deduced by using the empty target runs and considering the value measured in the ZeroDegree Spectrometer that corresponds to the centroid of the Gaussian velocity distribution. The energy in front of the target is then extracted from this information and used in the DALI2 GEANT4 simulations where the energy loss factors along the target are introduced from the ATIMA parametrization. The input parameters for the ATIMA code are the charge  $Z$  and mass  $A$  of the fragment, its initial kinetic energy in front of the target, and the thickness of the matter which causes energy loss. This then returns the fragment kinetic energy after passing through the target and enables one to calculate the corresponding velocity. However, the calculated value corresponds only to the centroid of the fragment velocity distribution. In the simulations, the interaction process was simulated and the  $\beta$  value before the interaction,  $\beta_b$ , real value at the moment of interaction,  $\beta_r$ , and value after the target,  $\beta_a$ , was determined.

However, the accuracy of the  $\beta$  value is limited by the lifetime of the excited state since the decay may occur at different positions, therefore the velocity varies and it is not possible to estimate the exact position of the particle in the moment of decay. The emission position of the  $\gamma$ -ray is usually taken as the center of the target. A thicker target enlarges the uncertainty on the interaction position. When the lifetime of the state is long, such that it can travel longer than the width of the target before it decays, the measured  $\gamma$ -ray peak becomes broader and leads to a low-energy tail.

In Figure 4.16,  $\beta$  distributions obtained from simulations before, at the moment of decay and after the target are shown. On the right plot, in order to show only the velocity change along the target, lifetime effects are eliminated by choosing the half-life of the excited state,  $t_{1/2} = 0$ . In this case, the beta distribution directly relates to the interaction probability distribution along the target thickness. The left plot shows the beta distribution when a non-zero lifetime is considered, when most of the decays occur after the interaction moment. In this figure, around 10% of the events decay along the target and

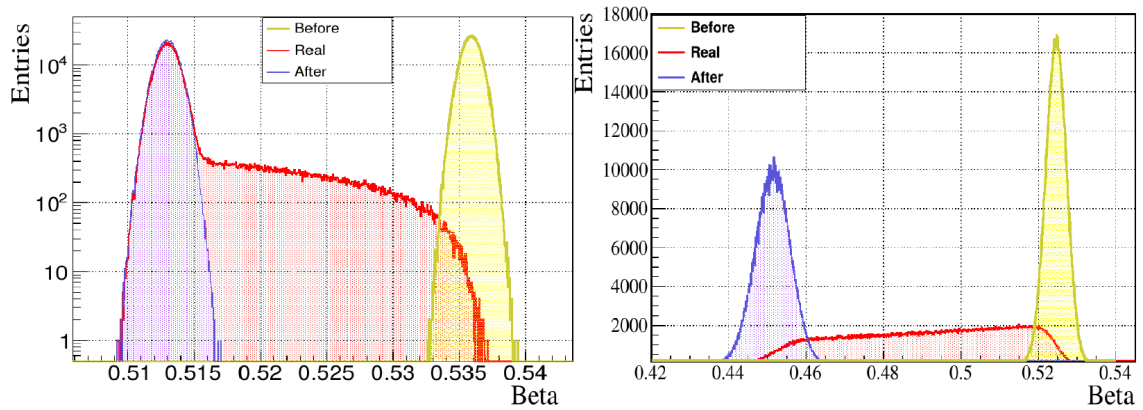


**Figure 4.16:** Simulated  $\beta$  values before, after and at the moment of decay is shown. In the right plot  $t_{1/2}$  effects are eliminated by taking it to be zero. In the left plot,  $t_{1/2} > 0$  (3.1 ps for  $2^+$  state of  $^{72}\text{Kr}$ ) therefore the most of the particles after interacting will travel through the target, before they decay.

the remainder decay afterward.

For the data analysis, the Doppler correction was performed by using the  $\beta_r$  value.  $\beta_r$  values for different isotopes are given in Table 4.5.

**Table 4.5:** The energy of corresponding isotopes in front of the target and obtained  $\beta$  values.

Isotope	$^{72}\text{Kr}$	$^{70}\text{Kr}$	$^{70}\text{Br}$	$^{68}\text{Se}$
$E_{\text{incident}} (\text{MeV}/u)$	170.06	167.78	161.70	164.295
$^{197}\text{Au}$ target				
$\beta$	0.50	0.46	0.45	0.46
$^9\text{Be}$ target				
$\beta$	0.48	0.48	0.47	0.47

## 4.5 The Analysis of the Emitted Gamma-Rays

Gamma rays carry information about the arrangement and ordering of excited states in the nucleus. Therefore, the detection and subsequent analysis of the emitted gamma rays is a key component of this study. To undertake this, several steps have to be considered, starting with an energy calibration and efficiency determination of the gamma-ray detection array, and subsequently extraction of the intensity of the  $\gamma$ -ray lines of interest. The steps of these processes will be discussed in this section.

### 4.5.1 Energy Calibration

The energy calibration for the detector electronics was performed using several  $\gamma$ -ray sources with different energies which cover the range of interest within these experi-

ments. The standard reference sources that were used are  $^{88}\text{Y}$  which emits  $\gamma$ -rays with two different energies, at  $898\text{ keV}$  and  $1836\text{ keV}$ ,  $^{137}\text{Cs}$  at  $661\text{ keV}$  and  $^{60}\text{Co}$  has two transitions with  $1173\text{ keV}$  and  $1332\text{ keV}$ . The calibration measurements were performed by placing each source inside the  $4\pi$  DALI2 array, on the beam-pipe, close to the detectors to collect enough statistics. Data was taken for 30 minutes depending on the source activity to obtain a sufficient level of statistics, during which the DALI2 detectors were run in self-trigger condition. The energy calibration was done by converting the corresponding ADC channels to the known source energies. Each ADC input has 4096 raw channels which corresponds to an approximate  $5\text{ MeV}$  energy range. The centroid channels of the peaks were identified for those known energies by fitting the spectra individually with proper fit function depending on the shape of the peak and the shape of the background. For an accurate line shape description of the peaks, a Hyper-EMG function (Hyper-Exponentially Modified Gaussian function) which can accommodate multiple exponential tailings of different strength on both left and right tails of a Gaussian was used [76]. Then, the channel to energy conversion was done by defining these conversion factors and offset parameters with a linear fit. The statistical uncertainty was

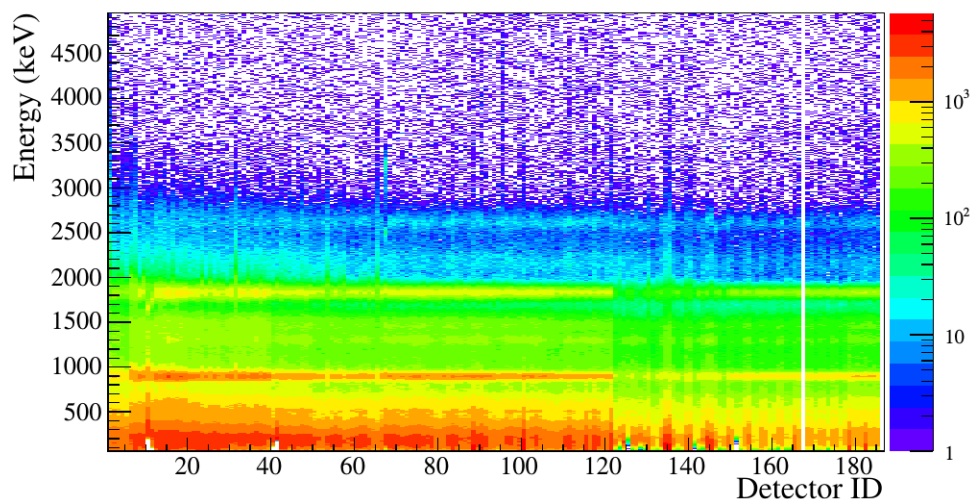


**Figure 4.17:** The energy spectra for a  $^{88}\text{Y}$  source as a function of the detector number.

taken into account to determine the error. The calibrated energy spectra from DALI2 detectors are shown in Figure 4.17 for a  $^{88}\text{Y}$  source. Detectors placed upstream at the beginning of DALI2 may have worse energy resolution due to possible radiation damage from incoming particles, detector ID 168 and 186 were not used and the ID 10 had a poor energy resolution such that  $\gamma$ -ray peaks were unresolvable.

The accuracy of the calibrated peak positions was checked for each source individually. The difference between the measured and known energy values of each transition was determined. This relative deviation in the energy,  $\delta E_{rel}$ , is defined by:

$$\delta E_{rel} = \frac{|E_T - E_M|}{E_T} \quad (4.13)$$

where the  $E_T$  is the known excitation energy from the literature and the  $E_M$  is the measured energy. The deviations among different detectors are represented in Figure 4.18, the measured and tabulated energies are listed in Table 4.6 together with the global energy resolutions. Most of the detectors showed a consistency within  $\sim 2\%$ . Four of the detectors showed a higher difference. They were removed from the analysis, and for consistency disabled in the simulation.

**Table 4.6:** Deviations between the calibrated energies and reference energies measured with the DALI2  $\gamma$ -ray detection array.

Source	Energy [keV]	Measured Energy [keV]	Resolution [%]
$^{137}\text{Cs}$	661	660 (1)	9.6(1)
$^{60}\text{Co}$	1173	1173 (2)	7.6 (2)
	1332	1332 (3)	7.1 (2)
$^{88}\text{Y}$	898	898 (1)	8.48 (8)
	1836	1834 (4)	6.24 (6)

The number of the photons created in the scintillation material depends on the energy of the  $\gamma$ -ray absorbed by the detector. Therefore, the resolution of the photo-peak is affected by the energy of the  $\gamma$ -ray with the following equation:

$$\text{FWHM} = a \times E^b \quad (4.14)$$

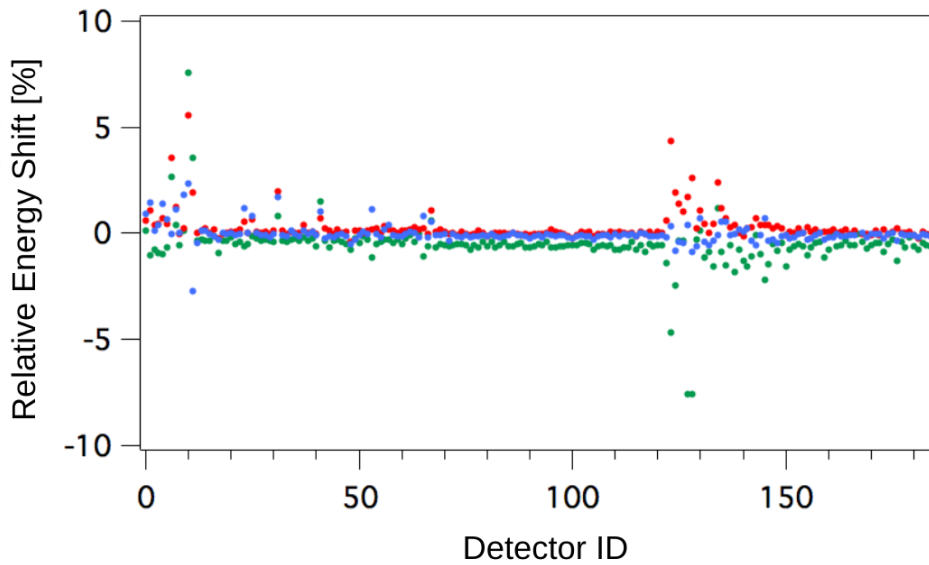


**Figure 4.18:** Energy difference between the measured and tabulated values of the source transitions. Red data points indicate the 898 keV emission of the  $^{88}\text{Y}$  source, while the green ones for the 662 keV emission of  $^{137}\text{Cs}$  and blue ones are for the 1332 keV emission of the  $^{60}\text{Co}$  source.

$a$  and  $b$  parameters are identified for each detector by fitting the data points and the results are used as an input file in Monte Carlo simulations where the detected energy is smeared with a Gaussian resolution function for a realistic comparison with the data. Figure 4.19 shows the energy resolution in sigma ( $\sigma$ ) as a function of energy where the

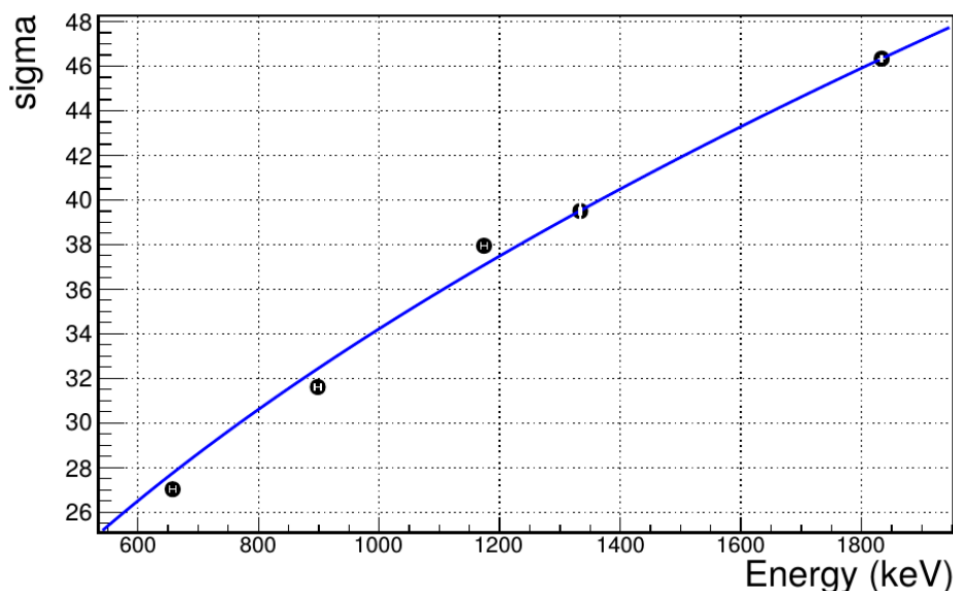


**Figure 4.19:** The dependence of the resolution on the energy for detector ID 65.

Full Width at Half Maximum (FWHM) is  $2.355\sigma$ . The blue solid line is a fit to the data points according to equation 4.14. The plot is obtained for detector ID 65, all the other detectors of the array also showed similar results.

The overall energy resolution of the system is a combination of the resolutions of all individual detectors. The detectors with a poor energy resolution or high gain shift were removed in the off-line analysis steps as to not affect the result. At the end, adding all correctly functioning DALI2 detectors, the observed peak positions from the reference energies could be reproduced within a few keV. The example of the fits that define the global energy resolution of the DALI2 array is shown in Figure 4.20 for all calibration sources.

#### 4.5.2 Full Energy Peak Efficiency

It is crucial to benchmark the simulations with the measurements to verify that they are compatible. Indeed, in order to determine the exclusive cross sections for the inelastic scattering channels, the number of emitted  $\gamma$ -rays has to be determined and this information is extracted by fitting the measured energy spectrum to the simulation. This verification is performed by determining the efficiency both for measurement and simulation.

The detection efficiency is a measure of the fraction of radiation that a given detector can detect from the overall yield emitted from the source. The number of emitted  $\gamma$ -rays can be determined from the source activity, the measurement time and the branching

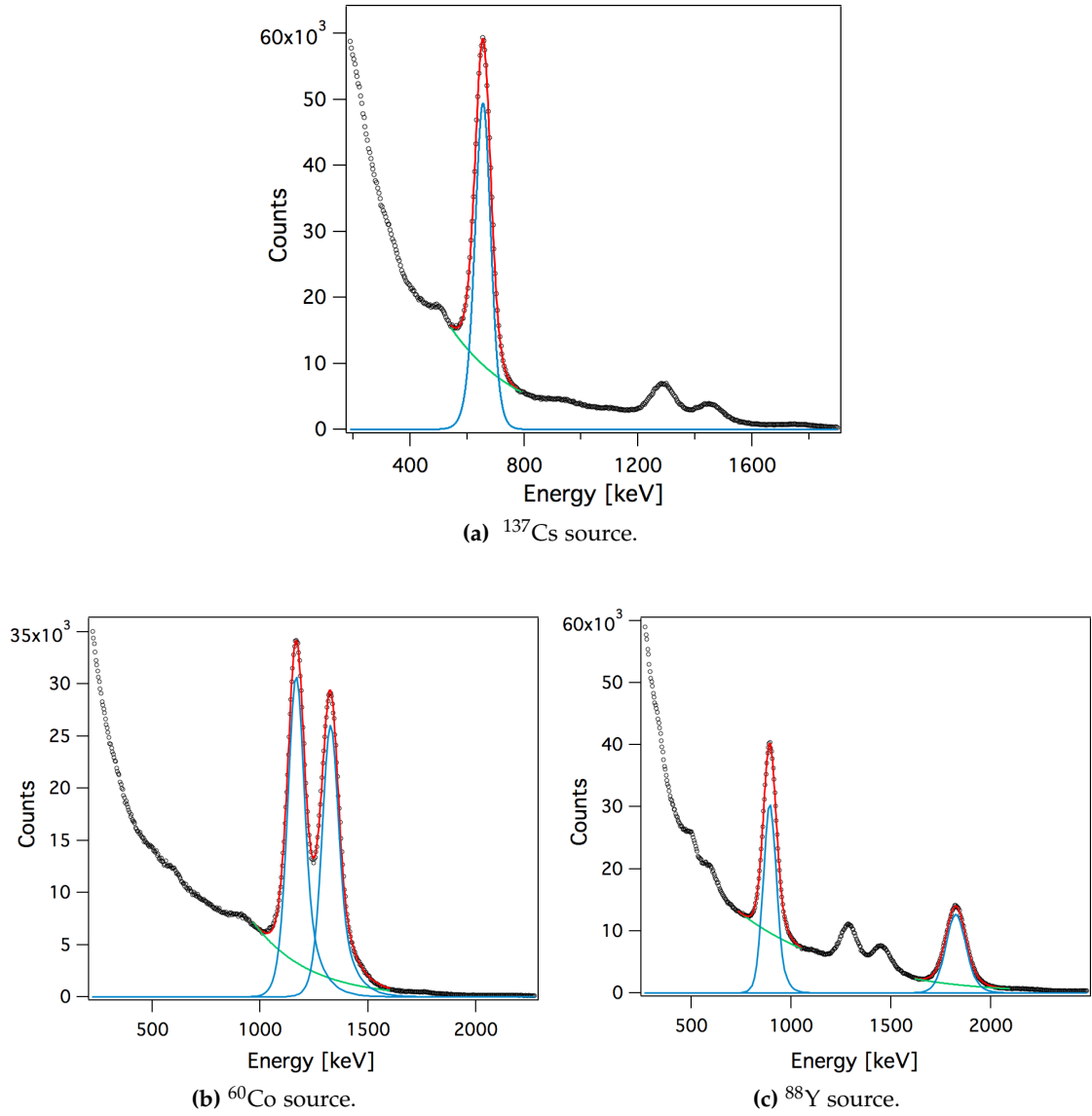


**Figure 4.20:** The energy spectra from different sources with background contributions including all the DALI2 detectors. Applied Gaussian fits are shown in the figures. The red lines correspond to the fit to the peaks, green lines are the fit for the background and blue lines are the final global fit.

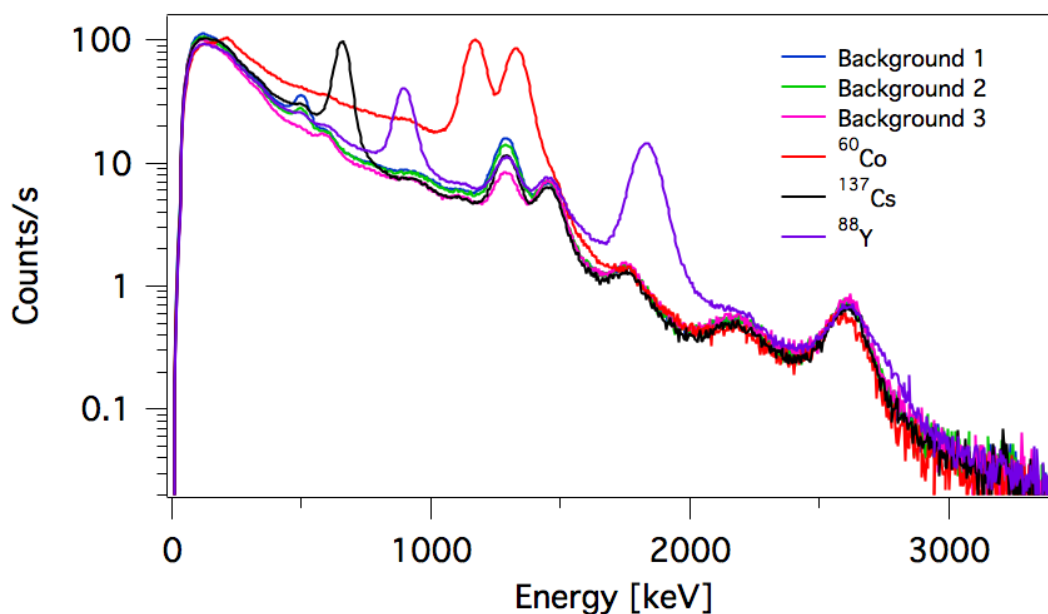
ratio for the emission. The detector can measure the emitted  $\gamma$ -ray depending on the geometry and live time of the data acquisition system. In order to eliminate geometrical detection effects, the sources used to calculate the efficiency  $^{60}\text{Co}$ ,  $^{137}\text{Cs}$  and  $^{88}\text{Y}$  were placed at the target position to measure the efficiency. The efficiency of the DALI2 array is then calculated with the formula:

$$\epsilon_{DALI2} = \frac{\gamma_{\text{measured}}}{\gamma_{\text{emitted}}} = \frac{\gamma_{\text{det}}}{A t \epsilon_{\text{LiveTime}}} \quad (4.15)$$

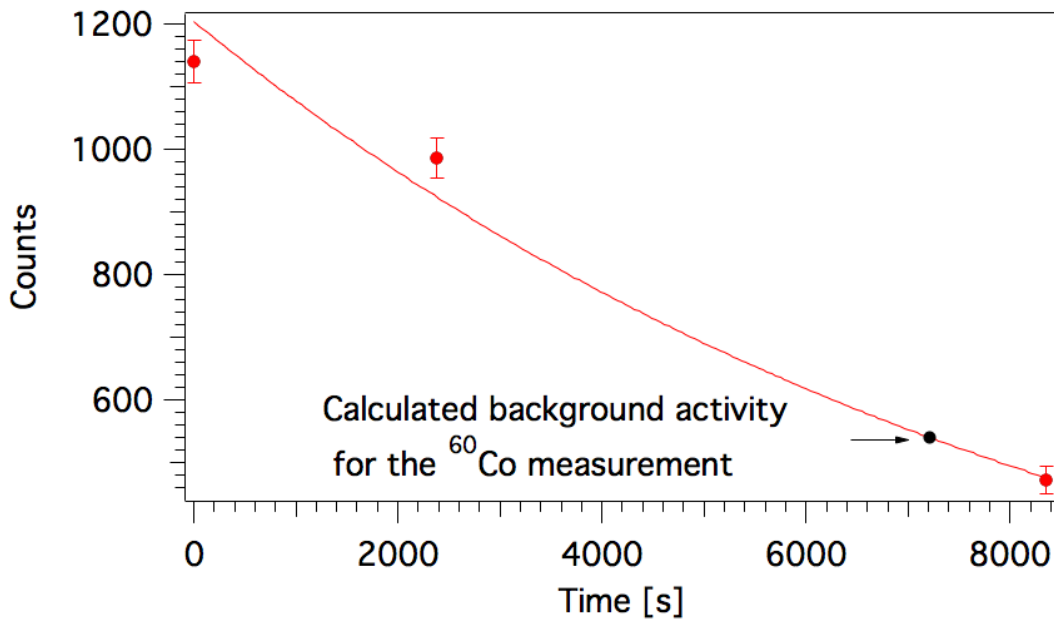
$\epsilon_{\text{LiveTime}}$  is the ratio of the accepted trigger with respect to the free triggers from the acquisition and accounts for the dead time of the DAQ,  $\gamma_{\text{det}}$  is the number of measured  $\gamma$ -rays in the integral of the peak,  $t$  is the measurement time and  $A$  is the activity of the source. All the measurements for the efficiency runs were taken in DALI2 self-trigger

mode. The number of emitted  $\gamma$ -rays can also be identified using another technique called the  $\gamma$ - $\gamma$  coincidence technique. In this method, the calculated efficiency is independent of the dead-time of the data acquisition system, and the activity of the radioactive source. The  $\gamma$ - $\gamma$  technique requires at least two different  $\gamma$ -rays emitted in coincidence, therefore it is applicable only for the  $^{60}\text{Co}$  and  $^{88}\text{Y}$  sources. The  $\gamma$ -rays decaying in coincidence belong to a cascade, and each transition was gated on individually. Then the other member of the cascade is fitted to determine the integral of the  $\gamma$ -ray peak that is in coincidence with the first one. Finally, the ratio of the number of  $\gamma$ -rays in the projected and gated  $\gamma$  peaks is taken. The same procedure can be applied the other way around. In order to identify the efficiency from measurements, both techniques are used and will be presented in this section.

During the measurements, a lot of unwanted background was present which stems from  $^{41}\text{Ar}$  that was produced at the primary beam reaction target. This radiation produces two  $\gamma$ -ray lines at  $491\text{ keV}$  and  $1294\text{ keV}$ . Since the  $1294\text{ keV}$  line is close to the  $^{60}\text{Co}$  lines in the produced spectrum, it is challenging to identify the efficiency in this energy region. Therefore, three background measurements were taken at different times in order to study this effect and subtract it properly. In Figure 4.21 all the source runs and the background runs are shown. For better comparison, the spectrum is given in logarithmic scale in  $y$  axis and all the measurements taken with different sources are time scaled. The decay of  $^{41}\text{Ar}$  into  $^{40}\text{K}$  was studied in order to identify the activity at the moment of the  $^{60}\text{Co}$  measurement. Using the well know activity formulas, the decay curve of the radioactive background was extracted. The value obtained for the  $1294\text{ keV}$  transition was found to be consistent with the  $109\text{ mins}$  value from literatures



**Figure 4.21:** Overlay of the spectra from different sources and the different background measurements taken at different times in order to study the activity of existing background.

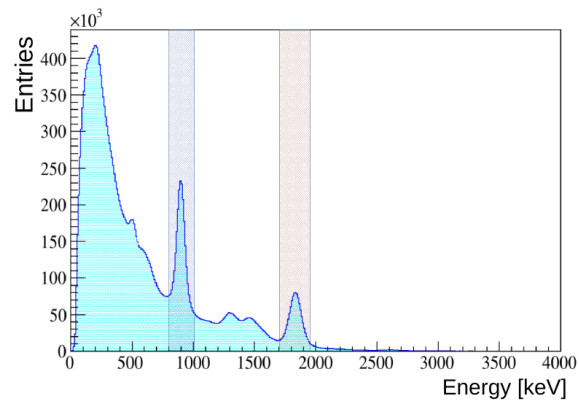
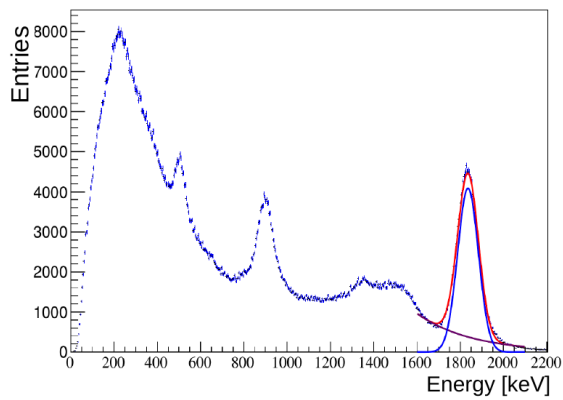


**Figure 4.22:** Decay curve of the radioactive background contaminating the  $^{60}\text{Co}$  transitions. The background at the moment of the source measurements was identified since the background intensity varies due to the decay. Then the background subtractions are applied to each run individually.

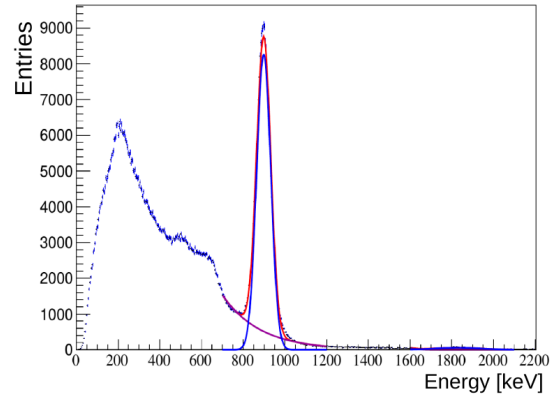
[77]. The activity of this background line was calculated for the time period of the  $^{60}\text{Co}$  measurement. An artificial background peak was then created using the known shape parameters from the background run and intensity from the calculated activity and used for the background subtraction procedure. In Figure 4.22 the decay curve is shown for the  $1294\text{ keV}$  transition, indicating the activity at the moment when the data for  $^{60}\text{Co}$  was being collected. Another high background radioactivity that affects the efficiency measurements appears at  $491\text{ keV}$ , close to the  $622\text{ keV}$  transition from the  $^{137}\text{Cs}$  source. In this case, the Background 2 measurement (see Figure 4.21) was directly subtracted from the  $^{137}\text{Cs}$  source spectrum since no significant change in the activity of the background was observed during these two different measurements. Additionally, all the other background contributions were subtracted from the affected source spectra individually. Finally, the number of detected  $\gamma$ -rays were identified by fitting the source spectrum with a proper fit function. Using equation 4.15, the measured efficiency of the DALI2 detector array was determined.

The  $\gamma$ - $\gamma$  technique was also used in order to determine the efficiency independently from the DAQ system. The applied procedure, as explained above, is shown in Figure 4.23.

The efficiency measurements were simulated to create the same experimental conditions.  $10^6$   $\gamma$ -rays were simulated and the efficiency was extracted by fitting the response function, in the same way it was done for the source measurements. The integral of the counts under the peaks was taken to determine the number of detected  $\gamma$ -rays in the

(a) Full spectrum of  $^{88}\text{Y}$  source

(b) Gated on the 898 keV transition



(c) Gated on the 1836 keV transition

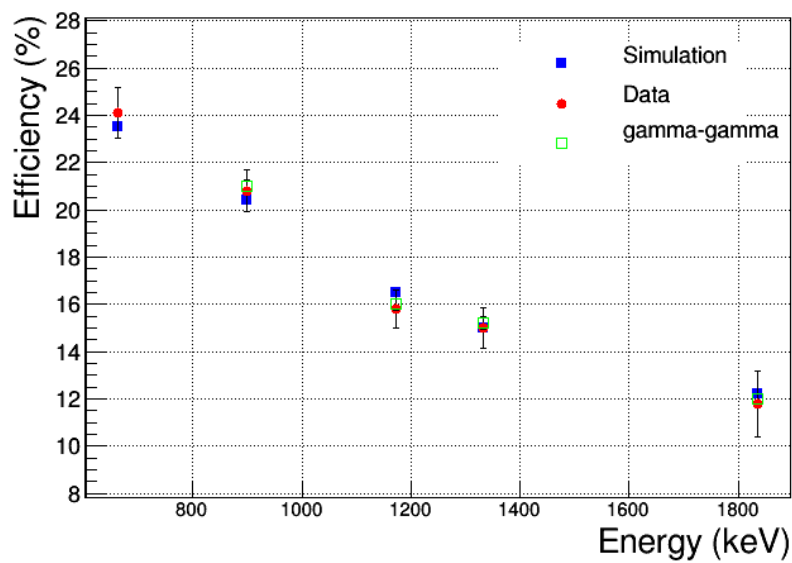
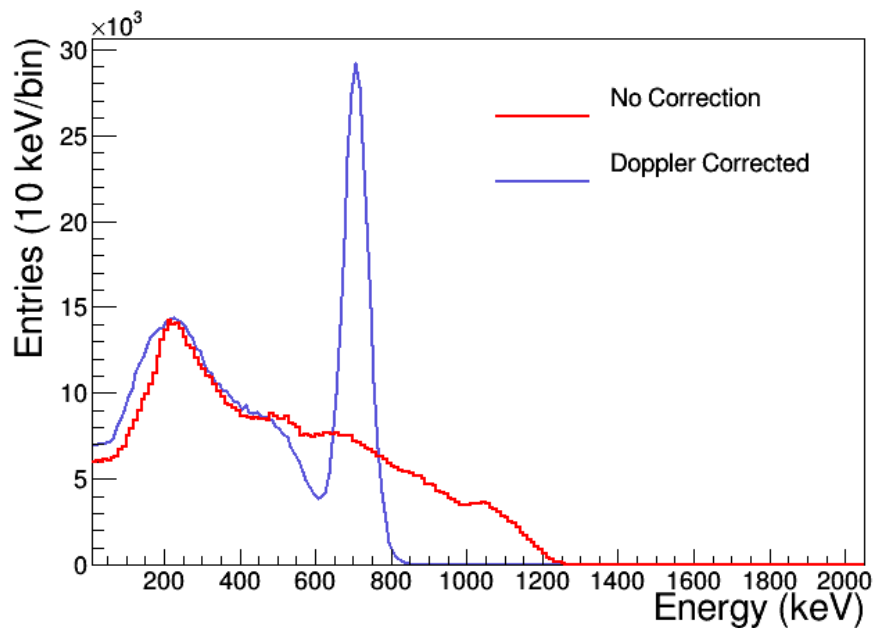
Figure 4.23: The  $\gamma$ - $\gamma$  technique for the  $^{88}\text{Y}$  source.

Figure 4.24: Comparison of the simulated and measured efficiencies from two different methods.

simulation. Comparable results were obtained from each method, within uncertainties, as shown in Figure 4.24. Hence, the simulations are verified and they can be used in order to reliably extract the cross sections of the performed experiments. The error bars indicate the statistical uncertainty of the detected radiation intensity of each source. The deviation of the simulated efficiency from the measured one was calculated for all the sources. The error of the detection efficiency varies between 1 % and 5.6 % among different sources and the largest deviation is obtained for the 1172 keV transition of the  $^{60}\text{Co}$  source.

### 4.5.3 Doppler Shift Correction

In section 3.5, the Doppler effect was introduced as one of the challenges in experiments performed with fast moving beams. A typical result of a Doppler shift correction is shown in Figure 4.25 which represents the photon energy distribution obtained from the simulation of a  $^{72}\text{Kr}$  secondary beam on a Au target. The  $\gamma$ -ray line at 710 keV from the  $2_1^+$  state is spread out over a large range and clearly unresolvable before the Doppler correction, but is clearly seen in the Doppler corrected energy distribution.



**Figure 4.25:** Comparison of Doppler corrected and not corrected spectrum for the simulated  $\gamma$ -ray transition with the energy of 710 keV. After the Doppler correction a peak appears at the correct transition energy.

The angle  $\theta$  can be determined by the geometrical position of the crystal center, where the emitted  $\gamma$ -ray is detected, with respect to the target position where the de-excitation occurs. In this case, the accuracy of  $\theta$  is limited by the large dimensions of the detector. Instead of using the geometrical center of each crystal, first interaction points were determined from Monte Carlo simulations for a more accurate polar angle determina-

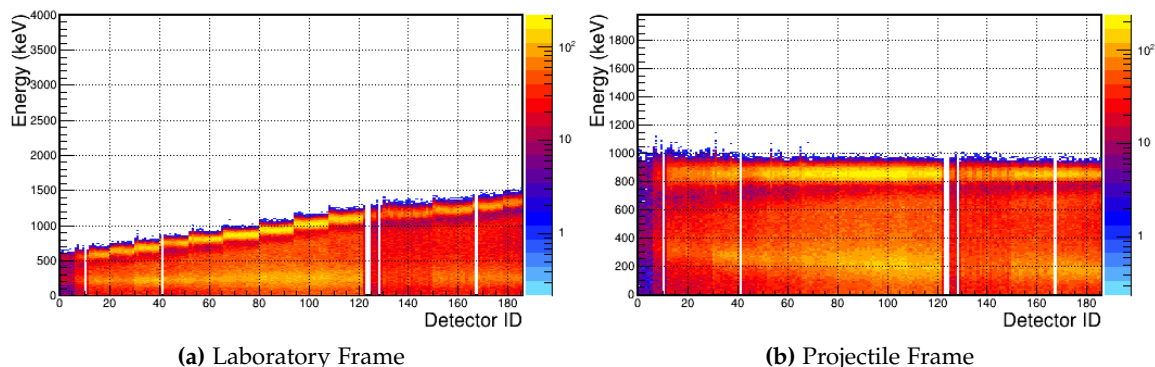


**Figure 4.26:** An energy-angle dependence of the emitted  $\gamma$ -rays (a) before and (b) after Doppler correction, obtained from simulations. No obvious dependence in (b) is seen which confirms the Doppler correction is applied. The empty ID numbers indicate the detectors removed from the analysis due to poor energy resolution or high gain shift.

tion. These average first interaction points are extracted from the simulation and were directly inserted in the data analysis as the coordinates of these interactions.

To test if the Doppler correction has been correctly carried out, the energy of the  $\gamma$ -rays over the array are plotted versus the detection angle, in Figure 4.26, before and after applying the Doppler correction in the simulations. After the correction, the observed  $\gamma$ -rays are shifted to the proper transition energy for all the detectors, irrespective of the angle of the detector. As mentioned before, the resolution and the intensity of the emission peak along the different angles are not constant. Due to the Lorentz boost, most of the  $\gamma$ -rays are emitted at forward angles. In the analysis of the Coulomb excitation, backward angles were discarded in order to maximize the peak to total ratio, and ignore the atomic background. Therefore, in the analysis of the inelastic scattering on the Au target, for  $^{72}\text{Kr}$  setting, detector ID  $< 52$ , and for the  $^{70}\text{Kr}$  setting, detector ID  $< 42$  were neglected. After Doppler correction,  $\sim 10\%$  in-beam energy resolution was obtained for an energy of  $850\text{ keV}$  which is in agreement with the Monte Carlo simulations.

#### 4.5.4 Time Calibration of the DALI2 Array

Radiation detection in the DALI2 array was set with the trigger condition to measure the events that is only in coincidence with the projectile and ejectiles in order to eliminate background events caused by the random coincidences from the environment. Afterward, a timing gate on the detected  $\gamma$ -rays was applied to reduce the random background. Initially, a calibration of the time signals was performed by aligning all the individual time signals of the array. The time signal from each detector was fitted with a Landau distribution and the start of the signals were aligned to the same time value. Figure 4.27 shows the time distribution of each crystal before (left) and after (right) the time calibration. In the off-line analysis procedure, a time window is set around the peak from  $-10\text{ ns}$  to  $10\text{ ns}$  to reject unwanted background. Figure 4.28 and 4.29 show the chosen time window that is considered for the analysis. On the right side of the

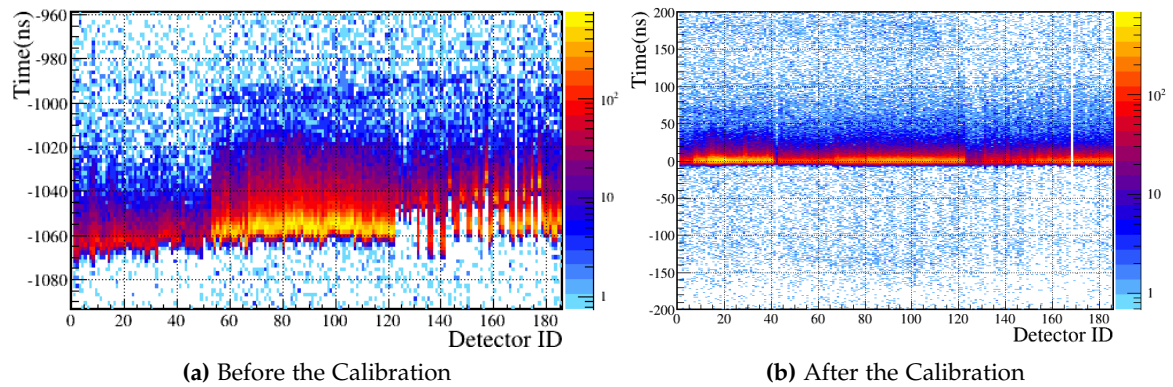


**Figure 4.27:** Time calibration of the 186 NaI(Tl) detectors.

time distribution, one can see a considerable amount of delayed events that are produced mainly by charged particles hitting the crystals and on both sides low energy background events. The time resolution of the system was determined to be 3 ns.

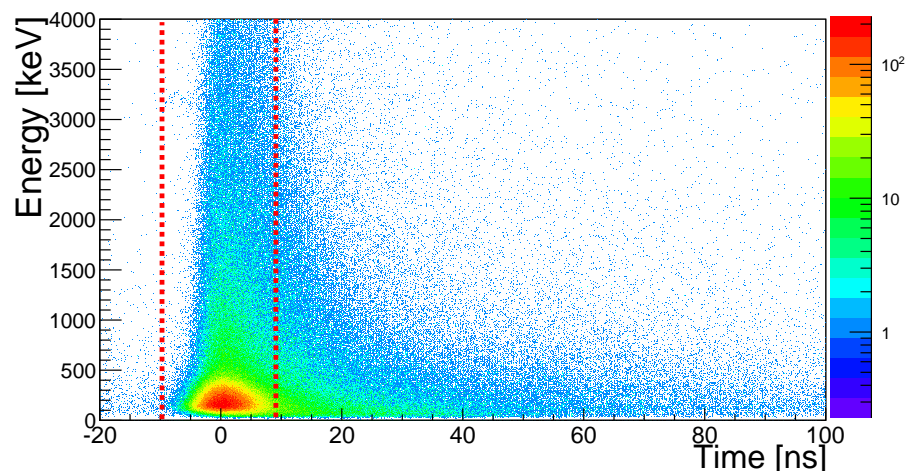


**Figure 4.28:** Energy-Time correlation, showing the selected and rejected events.

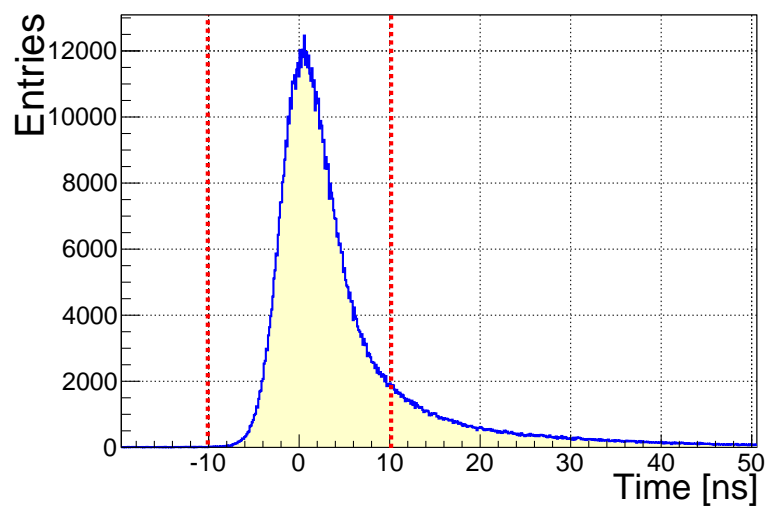


**Figure 4.29:** Time projection of the selected time window for DALI2.

# 5 | Results

In this chapter, the results obtained from the inelastic scattering of selected isotopes around mass 70 on  $^{197}\text{Au}$  and  $^9\text{Be}$  targets are presented. The main goal of the experiment was to determine the  $B(E2)$  value for  $^{70}\text{Kr}$  for the first time through the Coulomb excitation. Neighboring isotopes  $^{72}\text{Kr}$ ,  $^{70}\text{Br}$  and  $^{68}\text{Se}$  were measured simultaneously in order to compare the obtained results with the literature and benchmark the analysis that we performed. This also allowed to check on the validity of the present experiment for the  $^{70}\text{Kr}$  case. For each beam and target combination, the exclusive excitation cross-sections of  $2^+$  states were determined from the number of  $\gamma$ -rays, incoming and outgoing beam particles, the target thickness and several other quantities like transmission of the particles along the spectrometer, detector efficiency etc. The cross-section results from both, the nuclear and electromagnetic interaction between the target and the projectile, were then used in order to determine the  $B(E2)$  values. In the case of scattering off a light target, the nuclear interaction dominates, and the reaction cross-section is used to extract the nuclear deformation length  $\delta_n$  of the isotope of interest in a rotational model. This  $\delta_n$  is then used to determine the Coulomb deformation length  $\delta_c$ , by adjusting it to the measured cross-section value in the scattering from the Au target. From the relation between those deformation lengths for different kinds of excitation and the deformation parameters,  $B(E2)\uparrow$  values are deduced using equation 2.43.

In section 5.1, the  $\gamma$ -ray energy spectra from the excitation in different reaction channels are presented together with the respective level schemes. The  $\gamma$ -ray energy spectra were fitted with the DALI2 response functions obtained from simulations in order to extract the number of emitted  $\gamma$ -rays for each reaction channel. In section 5.2, the cross-sections from the reaction channels are discussed. Exclusive reaction cross-sections for the  $2^+$  states for the inelastic scattering on the Be and Au targets were determined. These excitation cross-sections were used to deduce the deformation lengths of the nuclear and Coulomb contributions of the interaction, from calculations based on the distorted wave theory using the ECIS97 code in section 5.3. The deformation lengths were then used to calculate the  $B(E2)\uparrow$  values that are given in section 5.3.1. finally, the results are compared to previous measurements and to theoretical calculations.

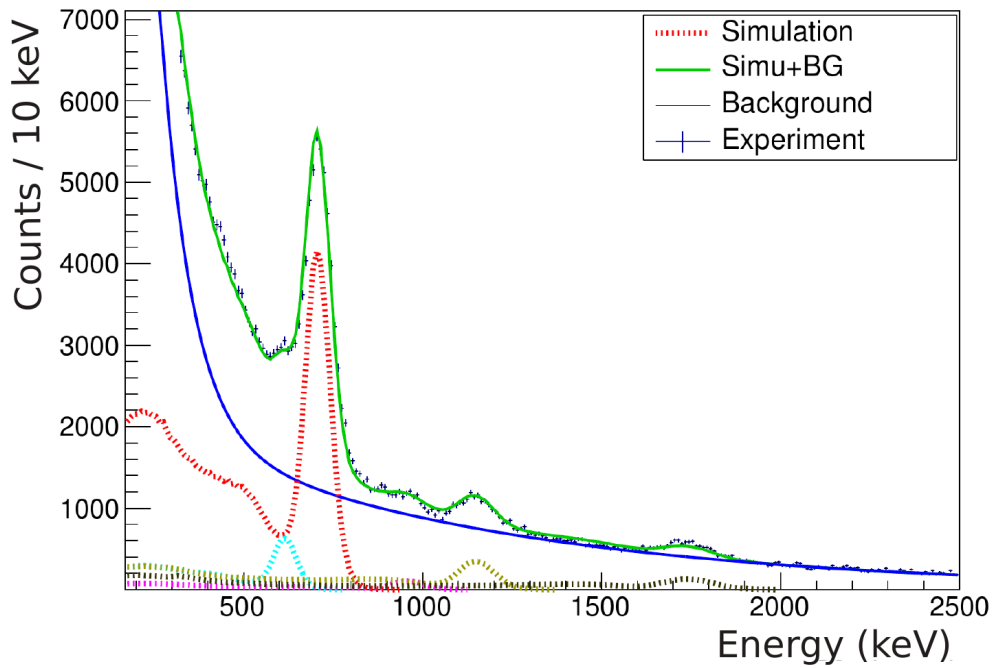
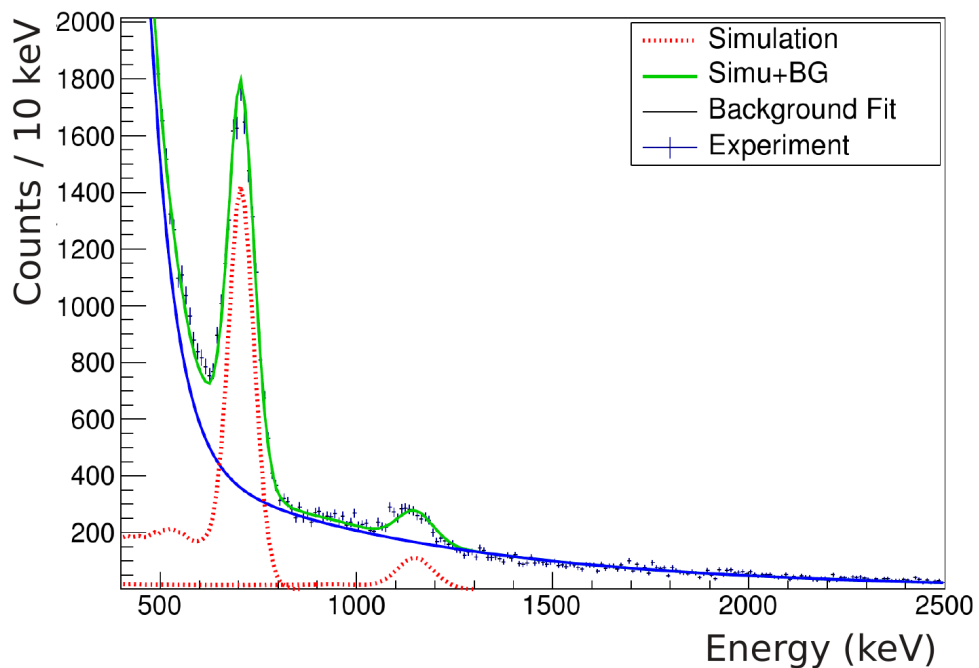
## 5.1 Reaction Channels

In this section, the analysis of the inelastic scattering data is presented, both from a heavy and light target. The usage of a heavy target enabled the study of the intermediate energy Coulomb excitation, while, a light target enabled extraction of the nuclear interaction deformation lengths to deduce the contribution of the nuclear part to the total cross-sections, and also investigate the indirect feedings from higher lying states to the  $2_1^+ \rightarrow 0^+$  transition.

Level schemes were constructed based on  $\gamma$ - $\gamma$  coincidence matrices, intensities of the transitions and comparisons with the neighboring isotopes or isobars, confirmed by available literature. To obtain a better peak to background ratio, an add-back procedure was also applied considering 15 cm of accepted distance with all multiplicity events. The detailed description about the add-back process is given in section 3.5, all multiplicity events are chosen in order to keep consistency with the efficiency determination. For the measured  $\gamma$ -rays, a Doppler correction was applied (see Section 4.5.3) and a prompt time window was set to  $\pm 5$  ns in order to reduce the background events (see Section 4.5.4). Results of the analysis are obtained both, with and without the add-back procedure to check the consistency. The decays that were observed in the experimental data were also replicated by Monte Carlo simulations. The experimental conditions created in the simulations also take into account the known life times of the excited states. For those with unknown lifetimes, it was always considered as  $t_{1/2} = 0$ . Finally, the number of emitted  $\gamma$ -rays was determined by fitting measured spectra with the simulated response function of the DALI2 array, keeping the line shapes and only scaling the amplitude of the peaks. The background was described by two exponential functions, the first one is used to describe the atomic background below 500 keV and the second one is used to model the high energy background stemming from unresolved transitions or secondary reactions up to 4000 keV. These conditions were used in order to simulate the  $\gamma$ -ray transitions for all of the cases. The points with error bars in the figures of the following chapters represent the measured data, the solid blue line is the sum of the two exponential functions that are used to describe the background. Fitted energy spectra are discussed in the following sections. Each transition was simulated separately and the response functions are given in the figures in different colors for each decay and the solid green line represents the final total fit.

### 5.1.1 Observed Excited States of $^{72}\text{Kr}$

Inelastic scattering of  $^{72}\text{Kr}$  on a  $^9\text{Be}$  target leads to the observation of five transitions shown in Figure 5.1.a. This isotope was also studied in intermediate energy Coulomb excitation with a  $^{197}\text{Au}$  target, where only the first and second excited  $2^+$  states were populated (see Figure 5.1.b.). The given spectrum from the inelastic scatterings from  $^9\text{Be}$  was created with add-back condition, while from the  $^{197}\text{Au}$  with no add-back. In order to construct the level scheme, the  $\gamma$ - $\gamma$  coincidence matrix was investigated. Coincidences were analyzed by putting a gate on each transition. Some of the observed coincidences that were used to build the level scheme are shown in Figure 5.3.

(a) Inelastic scattering on the  $^9\text{Be}$  target(b) Inelastic scattering on the  $^{197}\text{Au}$  target

**Figure 5.1:** Doppler shift corrected energy spectra obtained for  $^{72}\text{Kr}$  from inelastic scattering on the  $^9\text{Be}$  target (with add-back) and  $^{197}\text{Au}$  target (without add-back). The response function for each transition is given in the figures in different colors, the blue solid line shows the background and the solid green line represents the final total fit.

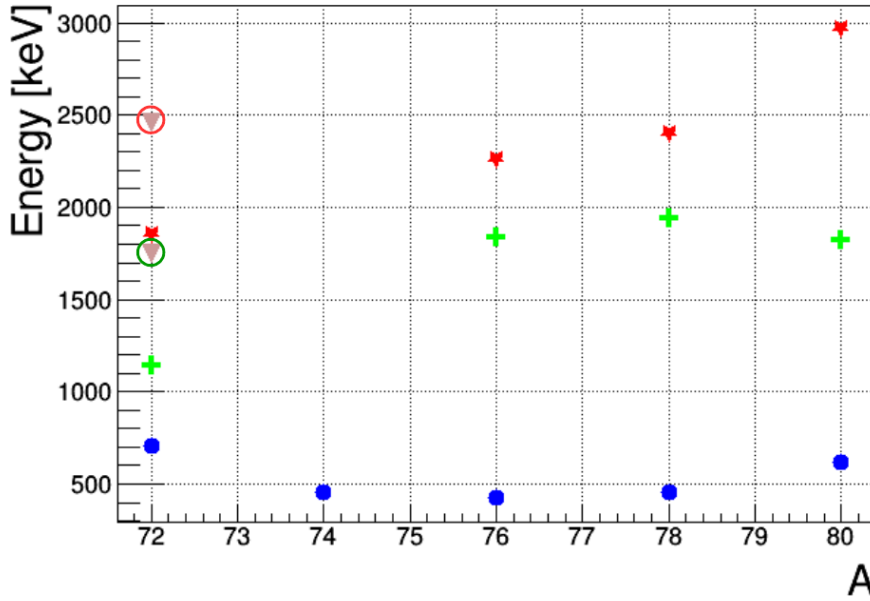
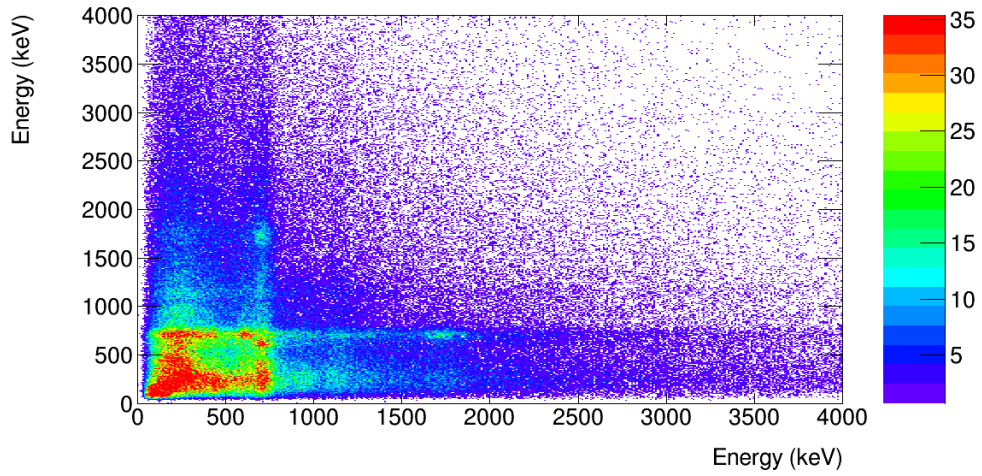


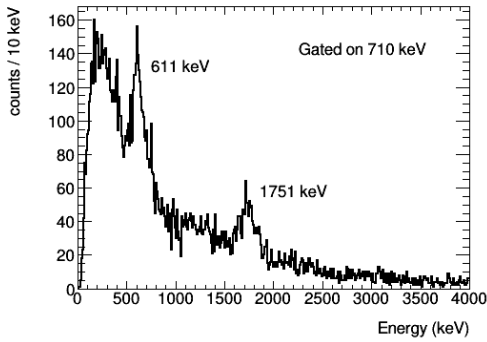
**Figure 5.2:** The figure illustrates the systematics of  $3^-$  and  $2^+$  states and  $3^- \rightarrow 2^+$  transitions for Kr isotopes. The green crosses shows the energies of  $3^- \rightarrow 2^+$  transitions, blue dots shows the energy of  $2^+$  states, while red stars show the energies of  $3^-$  states from literature [79]. The two pink triangles represent the  $3^-$  state assigned in this study, with the red circle referring to the energy of the  $3^-$  state and the green circle to the  $3^- \rightarrow 2^+$  transition respectively.

The strongest  $\gamma$ -ray line at 710(1) keV is the known  $2^+ \rightarrow 0^+_{gs}$  transition. This transition was measured before in several experiments and the energy in literature is given as 709.72(14) keV. In the scattering through the  $^{197}\text{Au}$  target, in addition to the  $2^+$  state, one more transition was observed. From the  $\gamma$ - $\gamma$  coincidence matrix, these two  $\gamma$ -rays were not found to be coincident. This transition was hence established as the  $2^+ \rightarrow 0^+_{gs}$ , giving the  $2^+$  state at an energy of 1155 keV.

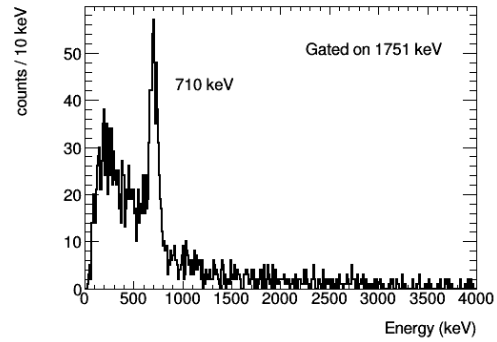
In the inelastic scattering experiment on the  $^9\text{Be}$  target, the  $2^+$  state is fed by two transitions. The first one with an energy of 611(4) keV was previously assigned as the  $4^+ \rightarrow 2^+$  transition [78, 7]. The second transition with an energy of 1751(38) keV was observed in this experiment for the first time. This new transition established a state at 2461 keV as  $3^-$ . Due to the coincidence of the two transitions as shown in Figure 5.3.c, it was assigned as the  $3^- \rightarrow 2^+$  transition. This assignment follows the trend of the known  $3^-$  states for neighboring Kr isotopes. The energies for the  $3^-$  and  $2^+$  states and the transitions between them are plotted for the Kr isotopic chain from  $A = 72$  to  $A = 80$  as shown in Figure 5.2. This finding is in contradiction with the literature values where the  $3^-$  state was placed at 1849.04(24) keV energy with a 1139.3(2) keV transition to the  $2^+$  state [78]. On the other hand, no such a state was observed that is in coincidence with the  $2^+$  state in the experiment performed at NSCL, with a reaction of  $^9\text{Be}(^{74}\text{Kr}, ^{72}\text{Kr}\gamma)$  [7]. The  $2^+$  state was also populated in the inelastic scattering measurement from the  $^9\text{Be}$  target with the transition of the  $2^+ \rightarrow 0^+_{gs}$ . Additionally, a line at 949 keV was observed in coincidence with this 1155 keV transition. Based on intensity ratios, the non-observation



(a)  $\gamma$ - $\gamma$  matrix for the  $^{72}\text{Kr}$  isotope



(b) Coincidence gate on the 710 keV peak



(c) Coincidence gate on the 1751 keV peak

Figure 5.3:  $\gamma$ - $\gamma$  coincidence matrix for the  $^{72}\text{Kr}$ .

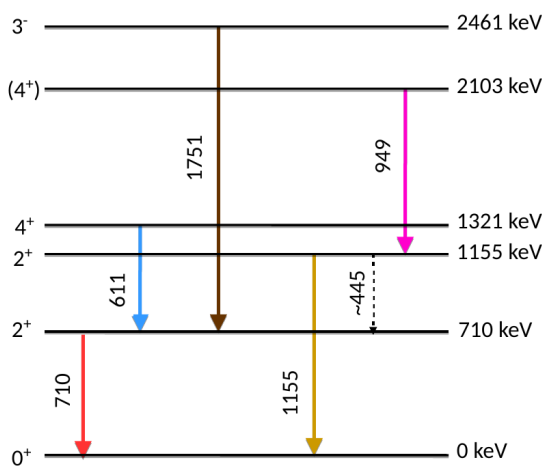


Figure 5.4: Level scheme of  $^{72}\text{Kr}$  obtained through a  $\gamma$ - $\gamma$  coincidence analysis. Each transition is given in different color that corresponds to the simulated response functions of these transition in Figure 5.1.

of a coincidence with the  $2_1^+ \rightarrow 0_{gs}^+$  transitions and the fact that the  $1155\text{ keV}$  transition is also observed in the measurement with the Au target, the  $2_2^+$  state at  $1155\text{ keV}$  was confirmed and the  $4_2^+$  candidate at  $2103\text{ keV}$  is established with the  $4_2^+ \rightarrow 2_2^+$  transition. The new level scheme is given in Figure 5.4. Another  $\gamma$ -ray line with an energy around  $445\text{ keV}$  was observed, which would correspond to the energy difference between the  $2_2^+$  and the  $2_1^+$  states, resulting in the  $2_2^+ \rightarrow 2_1^+$  transition. However, it was not possible to perform a  $\gamma$ - $\gamma$  coincidences, due to the low statistics, high atomic background in the region and random coincidences caused by the Compton edges. Nevertheless, the final cross-sections are calculated by assuming the possible feeding of this transition to the  $2^+$  state and excluding it, in order to consider the effect of this population on the final values. Results are discussed in section 5.2.

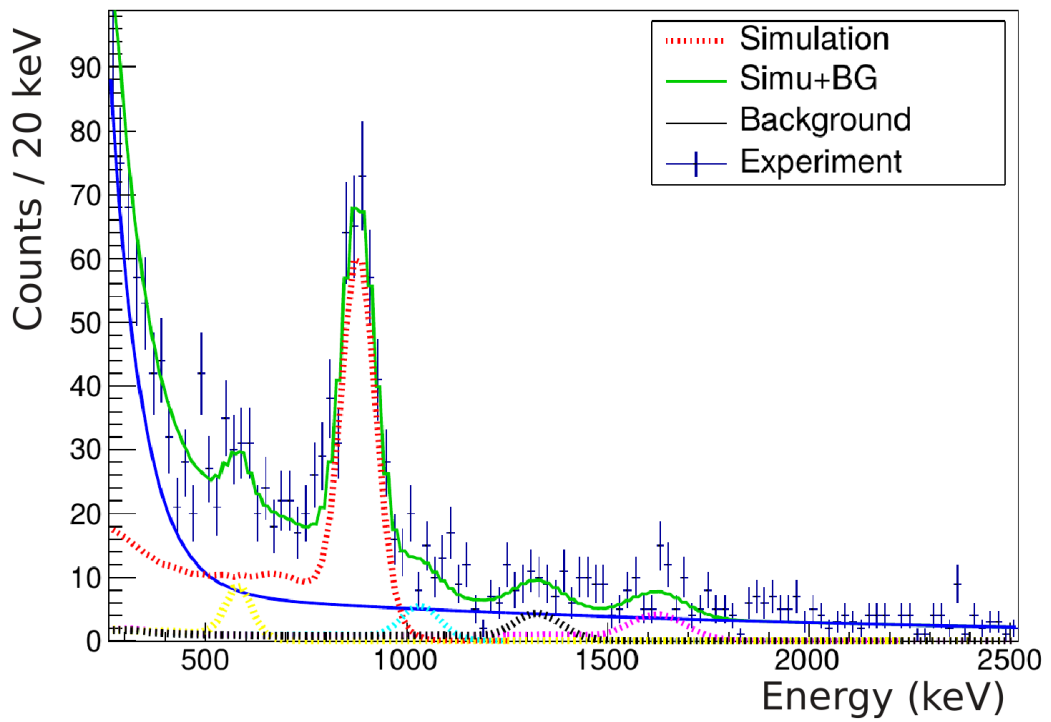
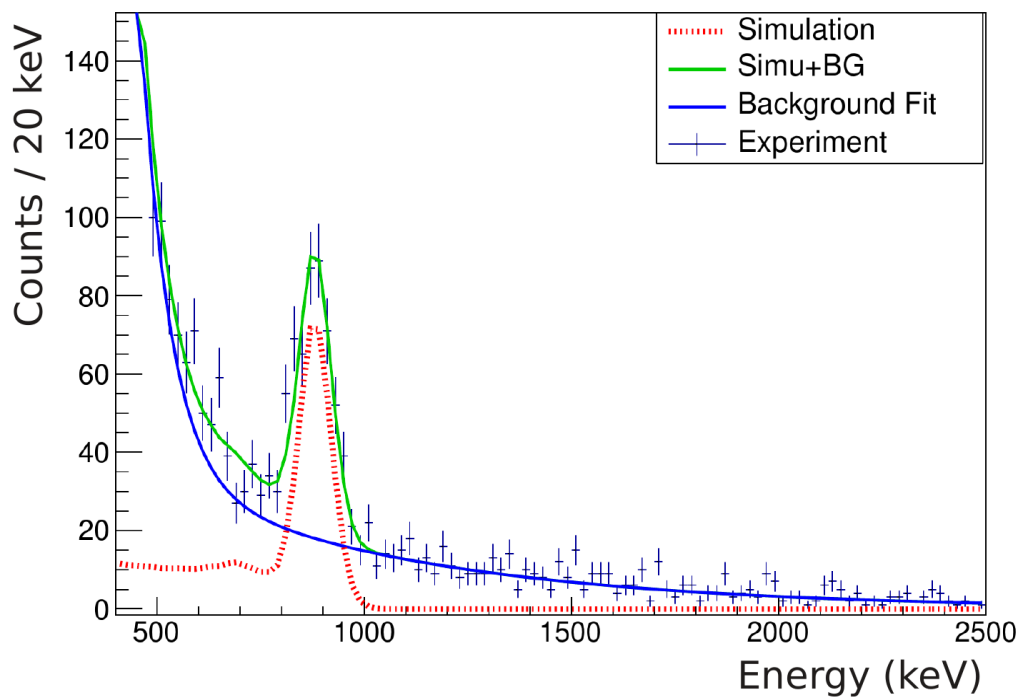
### 5.1.2 Observed Excited States of $^{70}\text{Kr}$

Excited states of  $^{70}\text{Kr}$  were investigated through the inelastic scattering on the  $^9\text{Be}$  and  $^{197}\text{Au}$  targets. The main goal of these experiments was to obtain the first spectroscopic information of  $^{70}\text{Kr}$  and to determine the  $B(E2)$  value of the first excited  $2^+$  state. Doppler shift corrected  $\gamma$ -ray spectra were analyzed as explained in section 5.1 and results are shown in Figure 5.5, with the add-back condition applied. Low statistics required the binning of the spectrum to  $20\text{ keV/bin}$  instead of  $10\text{ keV/bin}$ , typically used for other  $\gamma$ -ray spectra. From the scattering on the  $^9\text{Be}$  target, five transitions were observed, while for Coulomb excitation, only one. Due to the low statistics of the presented data, the analysis of the  $\gamma - \gamma$  coincidences was not possible. Therefore, tentative spin and parity assignments were mainly performed based on comparing the measured similar transition energies with its mirror nucleus  $^{70}\text{Se}$ , the evolution of the transition energies, the excited states along the isotonic chain and the systematics along the Kr isotopes [80, 81, 82].

The strongest transition in both experiments was observed at the energy of  $885(4)\text{ keV}$ . It is assigned as the  $2_1^+ \rightarrow 0_{gs}^+$  transition. The  $1039\text{ keV}$  transition is assigned as the  $4_1^+ \rightarrow 2_1^+$  with the  $4_1^+$  state at an energy of  $1917\text{ keV}$ . The  $1633(9)\text{ keV}$  transition was assigned as the  $3^- \rightarrow 2_1^+$ , thus the  $3^-$  state lies at an energy of  $2517\text{ keV}$ . The  $3^-$  state energy is comparable with its mirror nucleus and it is the second most strongest populated in the inelastic channel. The possible  $2_2^+ \rightarrow 2_1^+$  transition was measured with an energy of  $591(13)\text{ keV}$ , establishing the  $2_2^+$  state at energy of  $1476\text{ keV}$ . A transition that is shown with a black line in Figure 5.6 with an energy around  $1350\text{ keV}$  in the level scheme had very little statistics, nevertheless considering the transitions around this energy in its mirror nuclei, the initial level of this transition was suspected to be the  $4_2^+$  state and populating the  $2_1^+$  state.

### 5.1.3 Observed Excited States in $^{70}\text{Br}$

The Doppler corrected  $\gamma$ -ray energy spectra from inelastic scattering of  $^{70}\text{Br}$  on the  $^9\text{Be}$  and  $^{197}\text{Au}$  target are shown in Figure 5.7 with the no add-back condition applied. From the scattering on the Au target, only the  $2^+$  state was populated, while with the Be tar-

(a) Inelastic scattering on the  $^9\text{Be}$  target(b) Inelastic scattering on the  $^{197}\text{Au}$  target**Figure 5.5:** Energy spectrum obtained for the  $^{70}\text{Kr}$  from inelastic scattering.

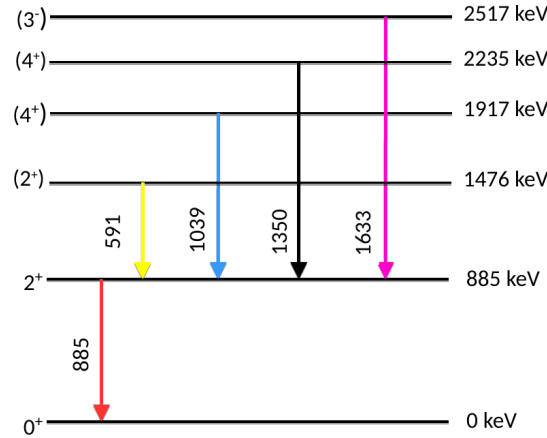


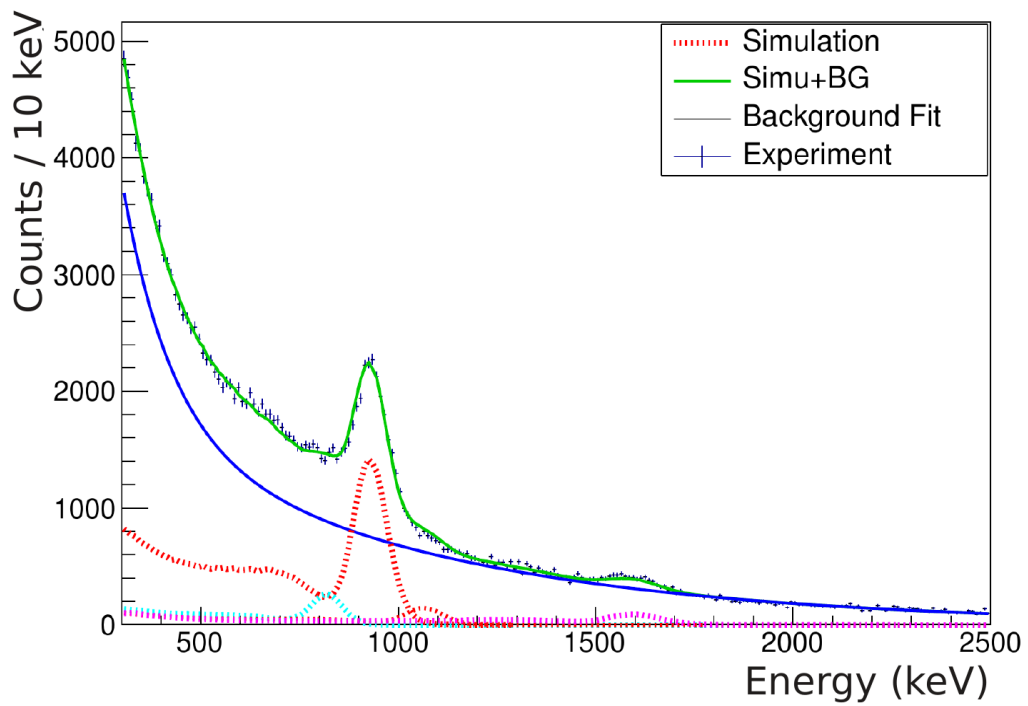
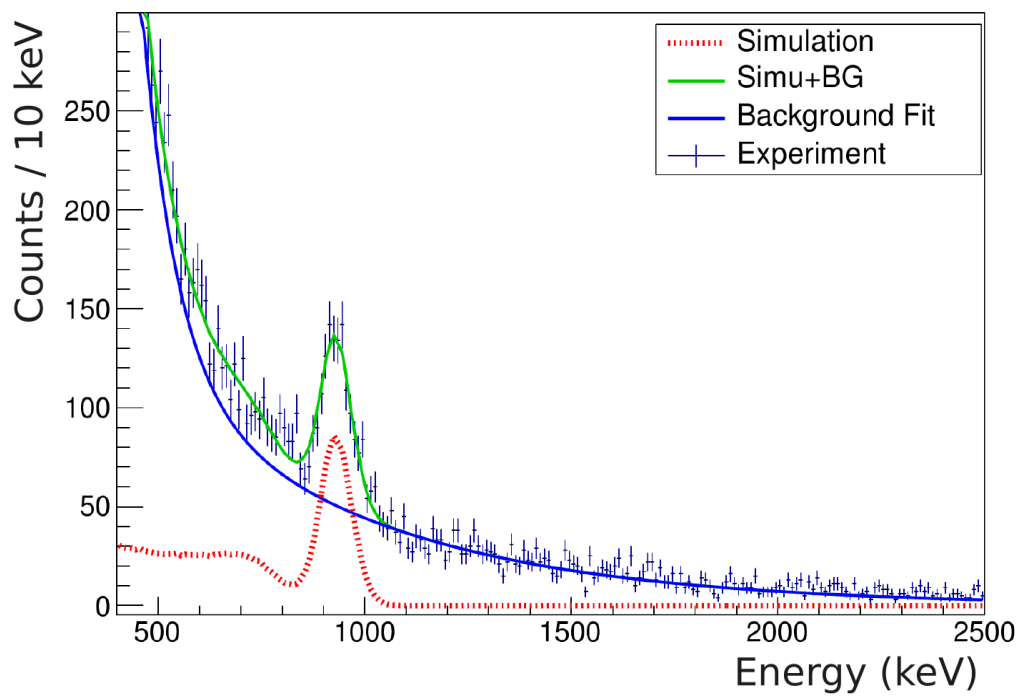
**Figure 5.6:** Level scheme of the  $^{70}\text{Kr}$  isotope.

get, four  $\gamma$ -ray transitions with energies of 809 keV, 933(2) keV, 1609 keV and 1603 keV were also observed. The  $\gamma$ -ray line with 933(2) keV energy belongs to the  $2_1^+ \rightarrow 0_{gs}^+$  transition. This  $2_1^+$  state was measured before in different experiments [83]. The second most strongly populated state is assigned as the  $3^-$ , decaying into  $2_1^+$  state with an energy of 1603 keV feeding the  $2_1^+$  state. This state is observed for the first time at an energy of 2536 keV and confirmed by applying the  $\gamma$ - $\gamma$  coincidence analysis technique. The  $\gamma$ - $\gamma$  coincidence matrix and the gated spectrum are given in Figure 5.8 and the final level scheme is shown in Figure 5.9. The transition with an energy of 1069 keV belongs to the  $4_1^+$  state and is feeding the  $2_1^+$  state. Due to the low energy resolution of the DALI2 array, it is not clearly separated from the 933(2) keV transition. This  $\gamma$ -ray transition was observed before as well in [84].

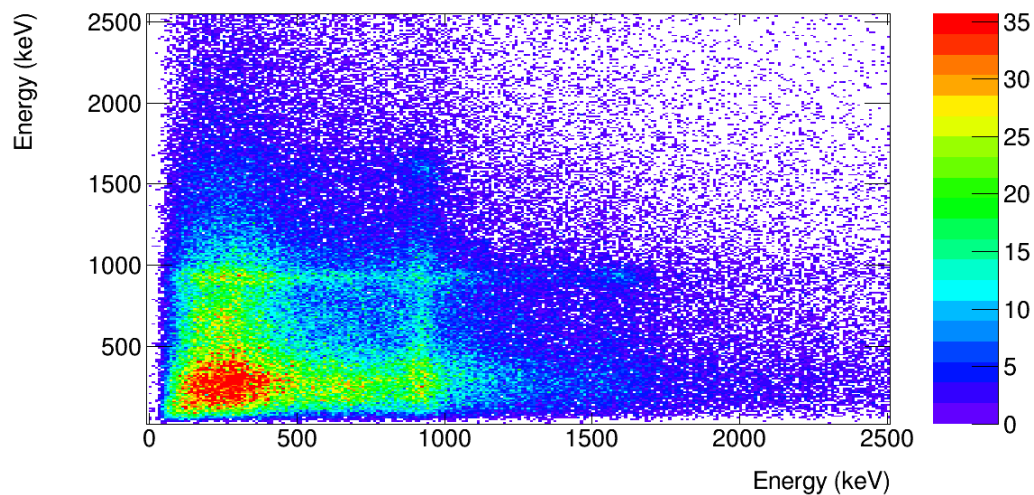
The transition with an energy around 810 keV, that is shown with the light blue dashed line in the Figure 5.7, is also not well separated due to the poor energy resolution of scintillators. However, the transition is added to improve the fit and determine its influence on the extracted number of  $\gamma$ -rays that belongs to the  $2_1^+ \rightarrow 0_{gs}^+$  transition. From the  $\gamma$ - $\gamma$  coincidence matrix, no correlation could be found between the 809 keV line and the other observed transitions. In the literature, a transition with a similar energy was assigned as the  $10^+ \rightarrow 9^+$  transition with a tentative spin-parity assignment of the  $10^+$  state, feeding an isomeric  $9^+$  state [85]. This transition is not included in the built level scheme for  $^{70}\text{Br}$ . Nevertheless, it is added to the analysis and contributed to the final results on the calculated B(E2) value of the  $2_1^+$  state.

#### 5.1.4 Observed Excited States of $^{68}\text{Se}$

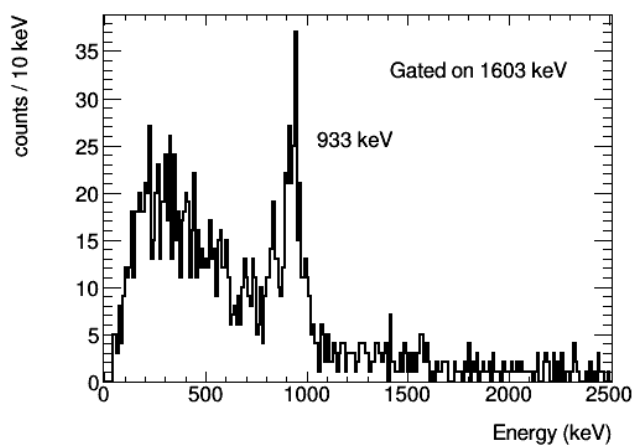
The observed transitions from the scattering of a  $^{197}\text{Au}$  target are as follows: the  $2_2^+ \rightarrow 2_1^+$  with an energy of 740 keV, the  $2_1^+ \rightarrow 0_{gs}^+$  with 854(1) keV and the  $2_2^+ \rightarrow 0_{gs}^+$  with 1594 keV. Since the transition with an energy of 1594 keV was populated as the second strongest state in the Coulomb excitation experiment, it was assigned to decay from the  $2_2^+$  state. The spectrum is shown with an inset around for this energy range in order to make it

(a) Inelastic scattering on the  $^9\text{Be}$  target(b) Inelastic scattering on the  $^{197}\text{Au}$  target

**Figure 5.7:** The  $\gamma$ -ray energy spectrum obtained for  $^{70}\text{Br}$  from inelastic scattering on a  $^9\text{Be}$  and  $^{197}\text{Au}$  target, respectively.

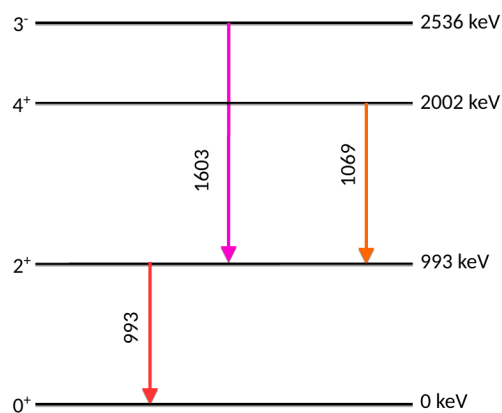


(a)  $\gamma$ - $\gamma$  matrix for the  $^{70}\text{Br}$  isotope

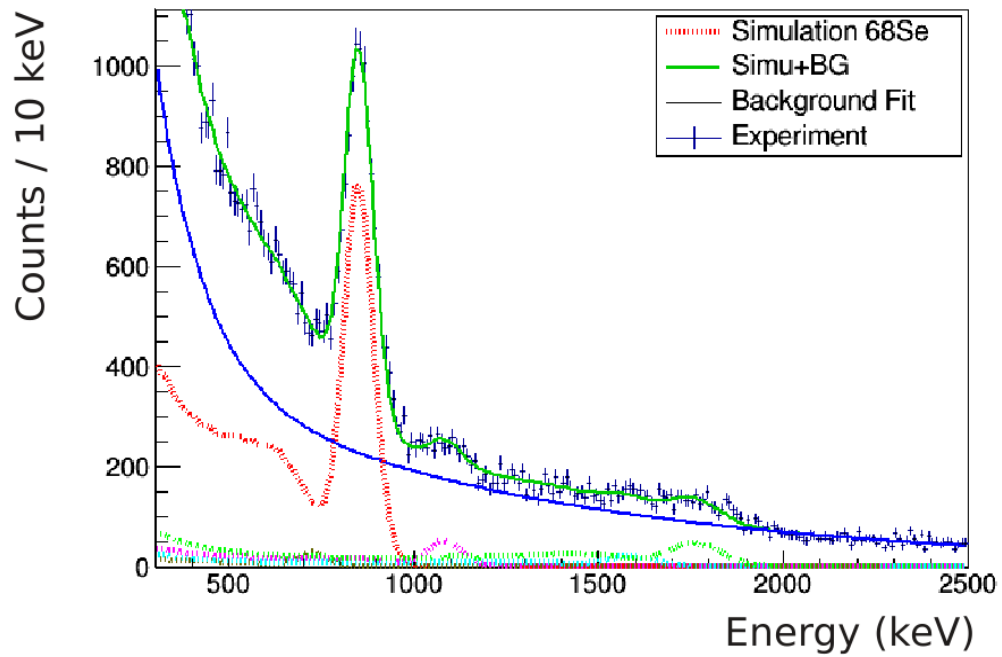
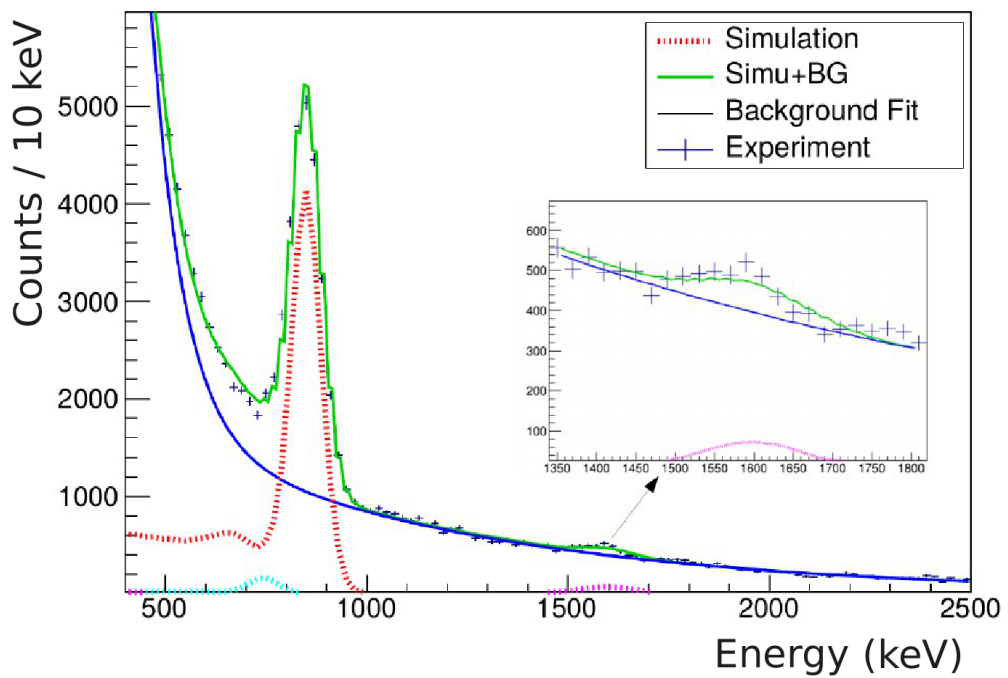


(b) Coincidence gate on the 1063 keV peak.

**Figure 5.8:**  $\gamma$ - $\gamma$  coincidence matrix for the  $^{70}\text{Br}$  and the gated spectrum.

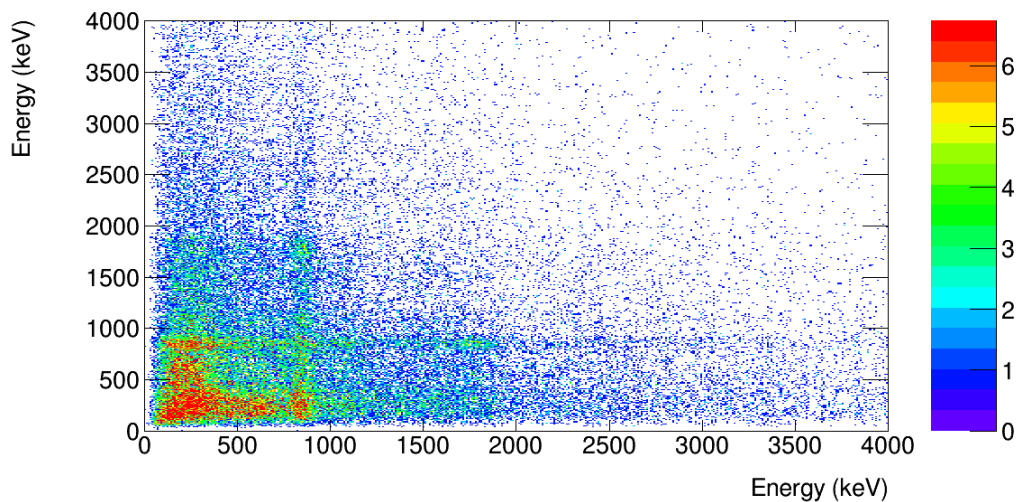


**Figure 5.9:** Level scheme of the  $^{70}\text{Br}$  isotope obtained by analyzing the  $\gamma$ - $\gamma$  coincidence matrix and the gated spectrum.

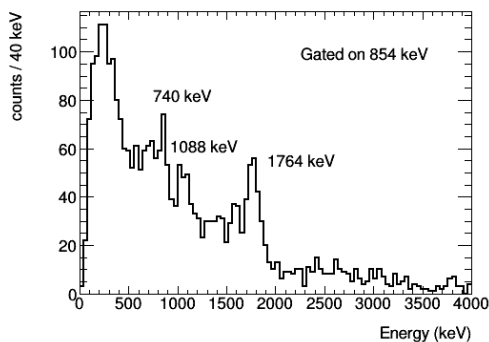
(a) Inelastic scattering on the  ${}^9\text{Be}$  target(b) Inelastic scattering on the  ${}^{197}\text{Au}$  target

**Figure 5.10:** The  $\gamma$ -ray energy spectrum obtained for the  ${}^{68}\text{Se}$  from inelastic scattering on a the  ${}^9\text{Be}$  and  ${}^{197}\text{Au}$  target.

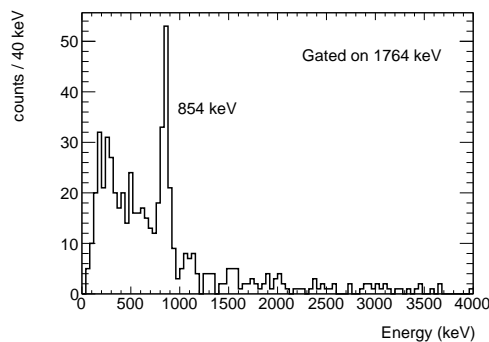
more visible in Figure 5.10(b).



(a)  $\gamma$ - $\gamma$  coincidence matrix for the  $^{68}\text{Se}$  isotope



(b) Coincidence gate on the 885 keV line.



(c) Coincidence gate on the 1764 keV line.

Figure 5.11:  $\gamma$ - $\gamma$  coincidences for the  $^{68}\text{Se}$  isotope and the gated spectra.

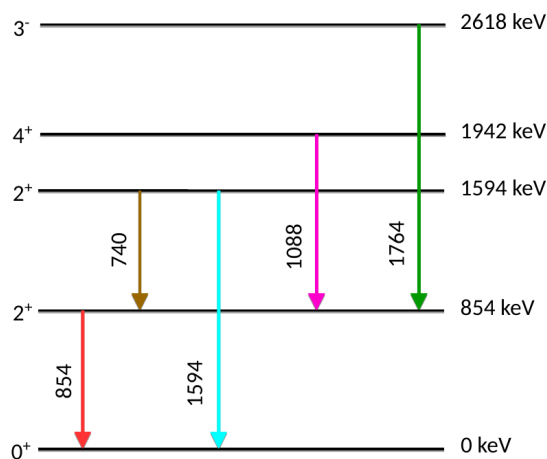


Figure 5.12: Level scheme of  $^{68}\text{Se}$  isotope obtained by analyzing the  $\gamma$ - $\gamma$  coincidence matrix

Five  $\gamma$ -ray transitions were observed from the inelastic scattering of  $^{68}\text{Se}$  on the  $^9\text{Be}$  target. They are shown in Figure 5.10(a) with no add-back condition applied, together with the scattering off a  $^{197}\text{Au}$  target with add-back applied below. The  $2_1^+ \rightarrow 0_{gs}^+$  transition to the ground state was measured before within several experiments. The  $2_2^+$  level with an energy of  $1594\text{ keV}$  is known to decay via two transitions, with  $1594\text{ keV}$  energy to the ground state and with  $740\text{ keV}$  to the  $2_1^+$  state. Even though this second transition is very weak, it is added in the simulations and used to fit the experimental data taking into account the known branching ratio [86].

In order to construct the level scheme from observed  $\gamma$ -rays, the  $\gamma$ - $\gamma$  coincidence matrix of the excitations was studied. When a coincidence gate is applied to the  $1764\text{ keV}$  transition, it leads to a strong coincidence with only the  $2_1^+$  state. This transition is assigned as the  $3_1^- \rightarrow 2_1^+$  decaying from the  $3_1^-$  state at  $2618\text{ keV}$ . A decay of similar energy was recorded in the literature as the  $6_2^+$  state decaying to the  $4_1^+$  state, however, such a coincidence is not observed in the present data [87]. When gating on the  $854\text{ keV}$  line, coincidences are observed with  $740\text{ keV}$ ,  $1088\text{ keV}$  and  $1764\text{ keV}$  transitions feeding the  $2_1^+$  state. These coincidences from the cascade are shown in Figure 5.11. Correlations are clearly seen between the emitted  $\gamma$ -rays from the same cascade. The new level scheme constructed from this analysis is given in Figure 5.12.

## 5.2 Measured Cross-Sections

The cross-section of a reaction is a measure for the probability of the excitation when projectile and target nuclei interact. In order to extract the  $B(E2)$  values, the electromagnetic excitation cross-section has to be determined. This pure Coulomb excitation cross-section can be calculated by identifying the contributions from the nuclear excitations, which appear at relativistic energies. Therefore, the inelastic nuclear scattering of the same isotopes with the same beam settings on a  $^9\text{Be}$  target was performed and the interaction cross-sections measured separately. Interference between the two excitations was studied via the calculated deformation lengths of each reaction type, reproducing the measured cross-sections. This procedure is given later in section 5.3.

In order to determine the exclusive cross-sections for each state, the number of emitted  $\gamma$ -rays has to be determined by adjusting the simulation to the experimental data, with a normalization factor  $k$ . Multiplying this factor with the number of simulated particles  $N_{\text{sim}}$ , the number of emitted  $\gamma$ -rays can be obtained. The intensity of each state has to be studied carefully, such that if there is feeding from higher states of the cascade, subtractions have to be taken into account with an additional statistical error on the number of final  $\gamma$ -rays. These values are divided by the number of incident particles on the target  $N_{BR}$ , which are obtained by requiring the F7DS trigger condition. Correcting  $N_{BR}$  with the transmission factor,  $T$  (section 4.3), and considering the number of atoms within the target  $N_{\text{Target}}$ , the exclusive cross-sections are calculated with the following

formula:

$$\sigma_{\text{exclusive}} = \frac{k N_{\text{sim}}}{T N_{\text{Target}} N_{\text{BR}}} \quad (5.1)$$

The results for the exclusive cross-sections are given in Table 5.1 for the  $2^+$  states of each isotope for all of the settings. All values are obtained from spectra with no add-back condition. The results with the add-back are equivalent within errors. The uncertainties shown in the table are only the contribution from the statistical error. Systematic errors are discussed in the following sections.

The observation of a tentative  $445 \text{ keV}$  line was outlined in section 5.1.1. An additional simulated peak was placed in the region to see the difference on the shape of final fit. The cross-sections were calculated by including and excluding this transition in order to study its influence on the final result. By including this transition, the cross-section of the  $2_1^+$  state is determined as  $25.9(8)\text{mb}$ , while  $26.0(10)\text{mb}$  is obtained when it was excluded. Since the deviation is within the error and would have a negligible effect on the final  $B(E2)$  value, it was not considered for the rest of the analysis.

**Table 5.1:** *The exclusive cross-sections for different channels. The uncertainties show only the statistical contribution.*

	$^{70}\text{Kr}$	$^{68}\text{Se}$	$^{70}\text{Br}$	$^{72}\text{Kr}$
Au target				
$\sigma_{2_1^+} [\text{mb}]$	281(28)	231(3)	157(9)	339(5)
$\sigma_{2_2^+} [\text{mb}]$		20(2)		41(3)
Be target				
$\sigma_{2_1^+} [\text{mb}]$	18(3)	22(1)	17(1)	26.0(10)
$\sigma_{2_2^+} [\text{mb}]$		4.4(4)		4.5(3)

### 5.3 Deformation Lengths for Nuclear and Electromagnetic Contributions

The deformation lengths for inelastic scattering including both nuclear and electromagnetic interactions were determined using the ECIS-97 code [3]. The rotational model is considered for the calculations. The code needs an input parametrization to describe the process such as beam energy, spin and parity of projectile and target ground state, the excitation energy, observed excited states etc. The nuclear interaction is described through the optical model, using the Wood-Saxon (WS) potential, which is parametrized by the potential depths, radii and the diffuseness. The optical potential is calculated separately for each isotope considering the energy and the velocity in the front, in the middle and behind the target by using the method explained in Furumoto *et.al* [88]. This method is called Global Optical Potential (GOP) and can be used for nucleus-nucleus

systems in the energy range of 50-400  $MeV/u$ . In order to determine the parameters for the WS potential, that was used in the ECIS input, the real and imaginary parts were fitted using volume and surface terms. The real part describes the refraction of the incoming beam and the imaginary part describes the inelastic process through the absorption. The Coulomb potential part is fitted by considering it as an electrostatic

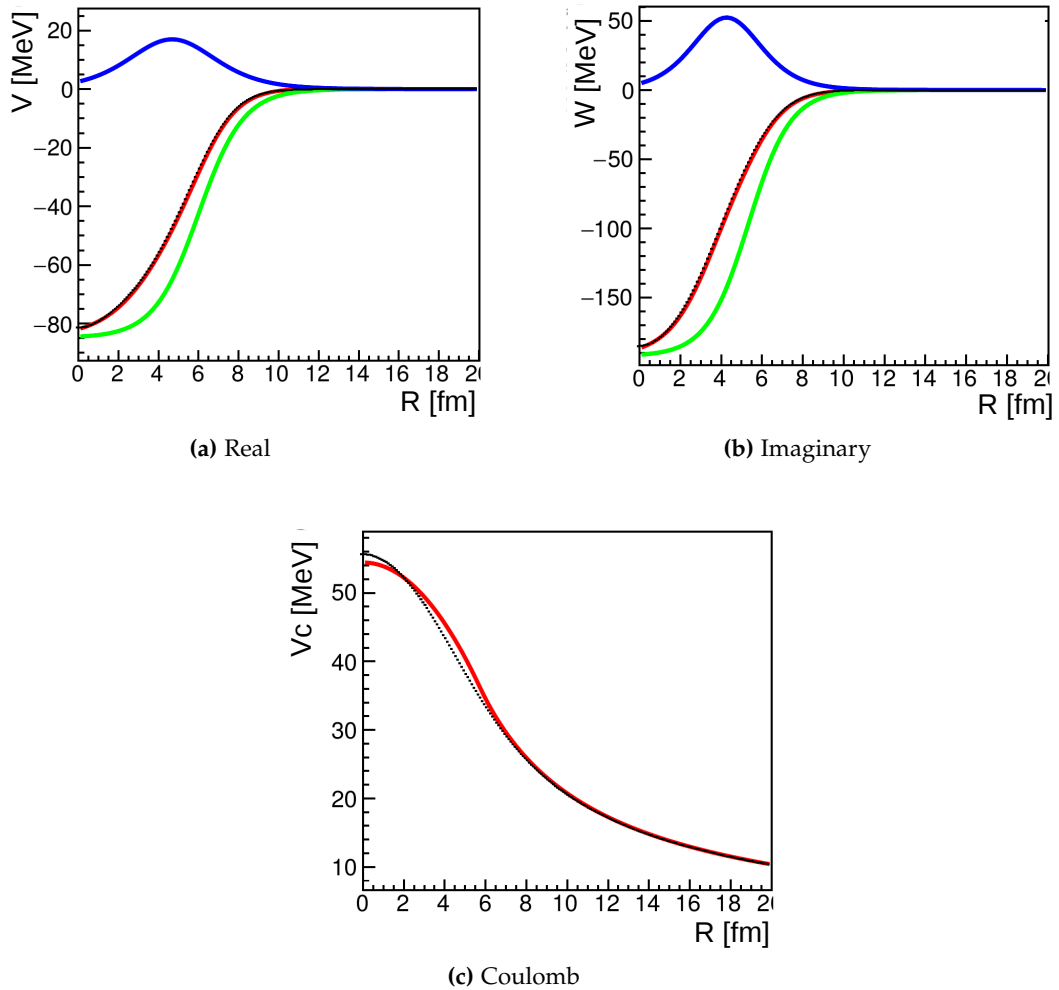


**Figure 5.13:** Example of the calculated optical potentials for the  $^{70}\text{Kr}$  isotope on the  $^9\text{Be}$  target at a beam energy of 144  $MeV/u$ . Fits were performed using a Wood-Saxon form for the real and imaginary potentials (red) with the volume (green) and surface term (blue) in a and b. The Coulomb potential is fitted by considering it as an electrostatic potential of a uniformly charged sphere (red) in c.

potential of a uniformly charged sphere as defined in equation 5.3. In Figure 5.13, the fits to the different components of the optical potential are shown. These fit parameters were then used as input in the ECIS-97 code.

The deformation lengths were determined as follows. A region of values were scanned that correspond to different cross-section values, and the resulting distribution is fitted with a quadratic function. The deformation length that corresponds to the measured cross-section value is then extracted with the errors that covers the uncertainty on the

relative cross-section value, as it is shown in Figure 5.14. The blue solid line shows relation between the deformation length and the measured excitation cross-section value, while the dashed blue lines indicate the uncertainty on this determination. Firstly, the

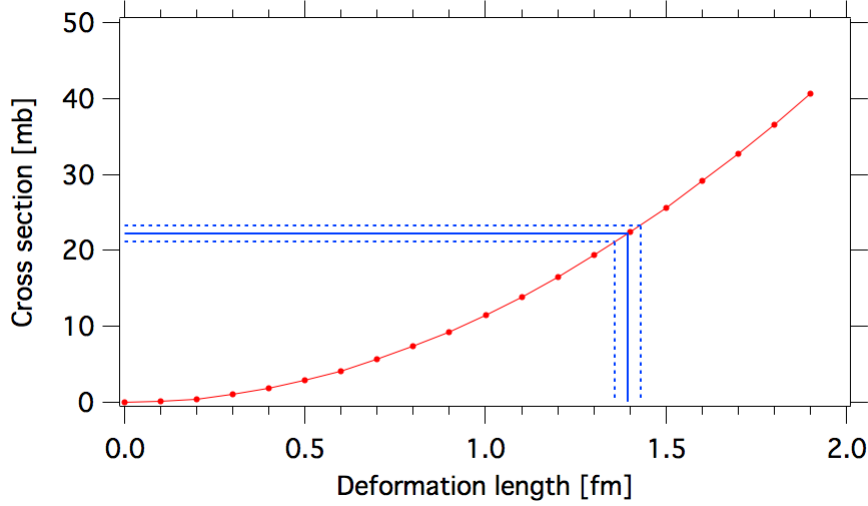


**Figure 5.14:** Nuclear deformation length,  $\delta_n$  corresponding to the experimentally measured cross-section for  $^{68}\text{Se}$  scattering off the  $^9\text{Be}$  target. The red dots connected with the line shows that dependence between the measured cross-section and calculated deformation length, the blue solid line indicates  $\delta_n$  value that gives the measured cross-section, while the blue dashed lines gives the error on this identification.

nuclear deformation length  $\delta_n$  is determined from the cross-section of inelastic scattering off a  $^9\text{Be}$  target. From this, in order to define the deformation length of the electromagnetic excitation, the  $\delta_n$  value is kept the same for the interaction of each isotope regardless from the type of the target. When the measured cross-sections are reproduced, the corresponding value is taken as  $\delta_c$ , the Coulomb excitation deformation length. The uncertainty on the deformation length is determined from the corresponding uncertainty on the cross-section. Table 5.2 represents the obtained  $\delta_n$  and  $\delta_c$  values with the uncertainties for each isotope.

**Table 5.2:** The obtained deformation lengths for inelastic and Coulomb excitations.

Excitation	$^{72}\text{Kr}$	$^{72}\text{Kr}$	$^{70}\text{Kr}$	$^{70}\text{Br}$	$^{68}\text{Se}$	$^{68}\text{Se}$
	$0_{gs}^+ \rightarrow 2_1^+$	$0_{gs}^+ \rightarrow 2_2^+$	$0_{gs}^+ \rightarrow 2_1^+$	$0_{gs}^+ \rightarrow 2_1^+$	$0_{gs}^+ \rightarrow 2_1^+$	$0_{gs}^+ \rightarrow 2_2^+$
$\delta_n$ [fm]	1.53(1)	0.63(1)	1.2(1)	1.19(1)	1.39(1)	0.62(2)
$\delta_c$ [fm]	1.17(1)	0.41(3)	0.97(7)	0.61(3)	0.90(1)	0.12(4)

These deformation lengths are then used to calculate the deformation parameter, which can be subsequently used to extract the  $B(E2)$  values from the relation in between.

### 5.3.1 B(E2) Value Determination

In order to deduce the reduced transition probability  $B(E2)\uparrow$ , the deformation parameters,  $\beta_c$  are determined from the deformation lengths.  $\beta_c$  can be expressed as:

$$\beta_c = \frac{\delta_c}{R_c} \quad (5.2)$$

where  $R_c$  is the nuclear radius in fm and is calculated from the following formula where  $A$  is the atomic number of the nucleus:

$$R_c = 1.2A^{1/3} \quad (5.3)$$

The radius of each projectile is calculated from equation 5.3 and the deformation parameters are extracted from equation 5.2. Calculated  $R_c$  values are given in Table 5.3.

**Table 5.3:** Calculated  $R_c$  and  $\beta_c$  values for the interested states of studied isotopes.

	$^{70}\text{Kr}$	$^{68}\text{Se}$	$^{70}\text{Br}$	$^{72}\text{Kr}$
	$(2_1^+)$	$(2_1^+), (2_2^+)$	$(2_1^+)$	$(2_1^+), (2_2^+)$
$R_c$ [fm]	4.94	4.89	4.94	4.99
$\beta_c$	0.27(1)	0.259(2)	0.17(1)	0.327(2)
		0.03(1)		0.113(5)

The  $B(E2)\uparrow$  values are then determined by considering the following relation with the deformation parameter:

$$B(E2)\uparrow = \left( \frac{3zeR_c^2}{4\pi} \right)^2 \beta_c^2 \quad (5.4)$$

**Table 5.4:** Extracted  $B(E2)\uparrow$  values for  $^{70}\text{Kr}$ ,  $^{68}\text{Se}$ ,  $^{70}\text{Br}$  and  $^{72}\text{Kr}$  isotopes.

	$^{70}\text{Kr}$	$^{68}\text{Se}$	$^{70}\text{Br}$	$^{72}\text{Kr}$
	$(2_1^+)$	$(2_1^+), (2_2^+)$	$(2_1^+)$	$(2_1^+), (2_2^+)$
$B(E2)\uparrow$ [ $e^2\text{b}^2$ ]	0.34(5)	0.255(4)	0.14(2)	0.491(7)
		<0.02		0.06(1)

The errors on the measured and calculated values originate from the systematic and statistical uncertainties. These variations from the identified value were determined separately by using error propagation. Error propagation of the cross-sections are performed by considering each component that is used in order to calculate the final value. One of the components is the error on the number of incident particles on the target which depends on the gated isotope. The number of emitted  $\gamma$ -rays are excluded by scaling the data with the simulation and the error is deduced from the final fit and

therefore includes the uncertainty in the background as well as the uncertainty in the peak. Feeding subtractions were also considered independently and error propagation was performed. The additional 5.6% systematic error arises due to the efficiency simulation of the DALI2 array. The error on the transmission is also considered since it was used to correct these numbers and was included in the error propagation. The uncertainty on the target thickness contributed 0.012 mm for the Be target, 0.004 mm for the Au target that is used for the  $^{72}\text{Kr}$  setting and 0.008 mm for the  $^{70}\text{Kr}$  setting. The systematic and statistical errors are independent and therefore were added separately in quadrature.

The  $B(E2)\uparrow$  values for  $^{70}\text{Br}$ ,  $^{72}\text{Kr}$  and  $^{68}\text{Se}$  are given in Table 5.4, indicating only statistical errors. The uncertainty on the  $B(E2)$  value of the  $^{70}\text{Kr}$  is largely caused by the low statistics. All values were deduced without the add-back condition and similar results were obtained with the add-back. The values given on the table are the upper limits for all the cases. Further investigation should be performed in order to ensure the amount of the contribution to the  $B(E2)$  value of these  $2^+$  states from not observed but existing feedings.

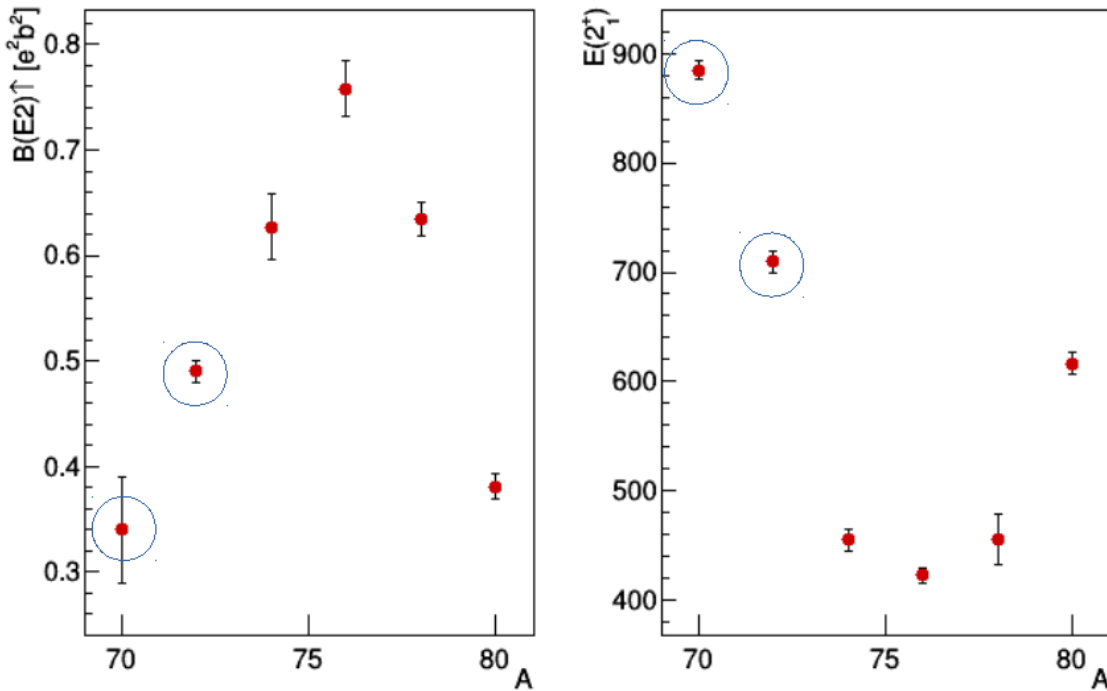


**Figure 5.15:** The left graph shows the  $B(E2)\uparrow$  values and the right graph shows the measured  $E(2^+)$  energies over the Kr isotopes as a function of the mass number  $A$ . The circles show the new values measured within this work.

The measured  $B(E2; 0_{gs}^+ \rightarrow 2_1^+)$  values and  $E(2^+)$  energies for  $^{70}\text{Kr}$  and  $^{72}\text{Kr}$  compared to the other Kr isotopes are shown in Figure 5.15. According to the distribution, the deduced values in this work fits to the generalized seniority scheme of the region. A plotted comparison is shown in Figure 5.15.

Additionally, the measured  $B(E2; 0_{gs}^+ \rightarrow 2_1^+)$  values for  $^{70}\text{Br}$  and  $^{68}\text{Se}$  are in agreement with the literature values. The consistency of the obtained  $B(E2)\uparrow$  values with the literature supports the validity of the  $B(E2)\uparrow$  value for  $^{70}\text{Kr}$ . The overall  $B(E2)\uparrow$  values that

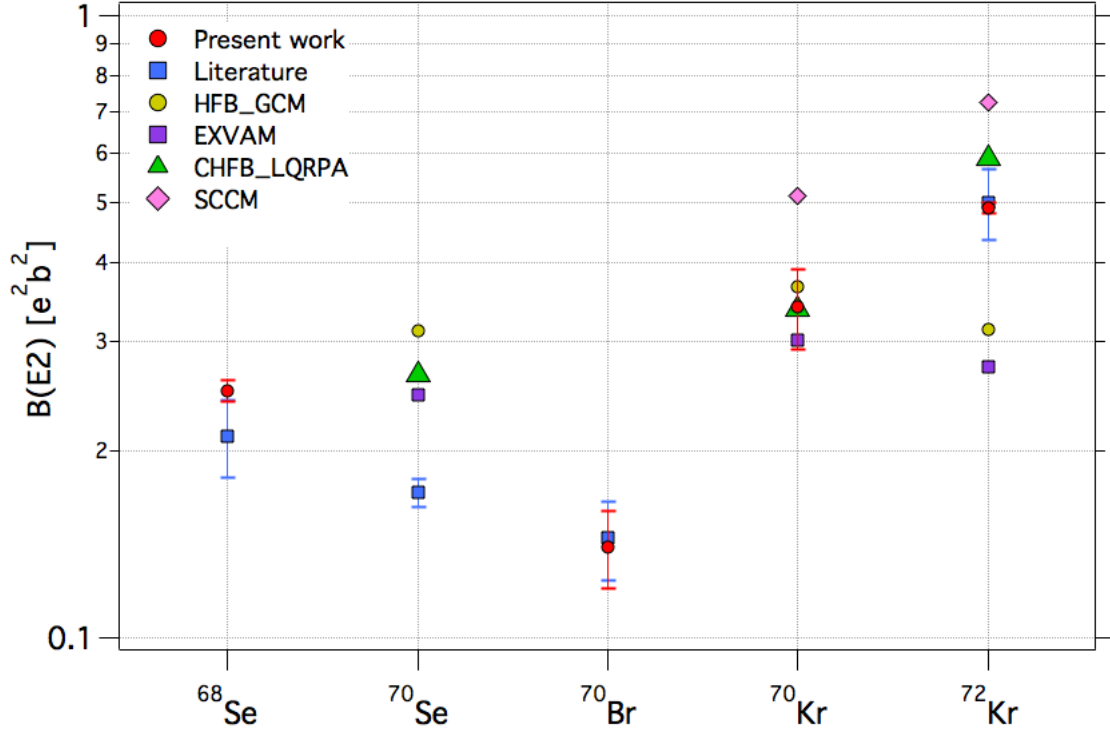


**Figure 5.16:** Determined  $B(E2)\uparrow$  values from the presented work is compared with the predictions from different theories and the previously obtained values from the literature.

were determined in the presented work is compared with the predictions from different theories and the previously obtained values from the literature. This comparison is shown in Figure 5.16 and discussed in detail within the next section.

## 5.4 Discussion

In this section, the experimentally obtained results and the predictions by different theories for  $^{70}\text{Kr}$  are discussed and compared to the neighboring isotopes. This comparison is done in two different frames, first as member of the Kr isotopic chain and then as member of the  $A = 70$   $T = 1$  isobaric multiplet.

### 5.4.1 Theoretical Predictions for the Kr Isotopes

Nuclei at or near the  $N = Z$  line, around  $A = 70$  mass are of particular interest due to the rapid increase in collectivity, see Figure 6.1. Several theoretical approaches, such as shell model methods, self consistent triaxial mean field models or beyond mean field models predict shape coexistence at low excitation energy in the light krypton isotopes. For instance, a shape transition from a prolate ground state shape in  $^{76}\text{Kr}$  and  $^{74}\text{Kr}$  to

oblate shape in  $^{72}\text{Kr}$  has been predicted by EXcited VAMpir (EXVAM) approach [10]. A Complex EXVAM predicts a strong oblate and prolate mixing, hence, large  $B(E2)$  values for the transitions connecting states of the same spin and parity [25]. For  $^{72}\text{Kr}$ , coexisting oblate ground state and low-lying prolate deformed excited states were also predicted by Möller [18] using a microscopic-macroscopic approach.

Further theoretical results came from the Symmetry Conserving Configuration Mixing (SCCM) method [19], HFB+GCM(GOA) calculations with the Gogny D1S interaction [20], the HFB+GCM calculations with the Skyrme interaction [89] and the constrained HFB with local quasi random phase approximation (CHFB+LQRPA) calculations [13]. The predictions of these calculations are listed in Table 5.5 and 5.6, and compared to the measured values. The  $B(E2)$  and  $E(2^+)$  values are compared for the  $T=1$  mirror nuclei  $^{70}\text{Se}$ ,  $^{70}\text{Kr}$  and the  $N=Z$  nucleus  $^{72}\text{Kr}$ . Theoretically, the best agreement for the  $B(E2)$  values is obtained by the CHFB+LQRPA method. Both the HFB-GCM and the EXVAM approaches underestimate the collectivity, while the SCCM calculations strongly overestimate the collectivity. Similar conclusions can be obtained for  $2^+$  energies, where the HFB-GCM approach comes closest to the experimental value.

**Table 5.5:** Experimentally obtained  $B(E2) \uparrow [e^2b^2]$  values compared to predictions. Listed experimental values are obtained from this study with the exception of  $^{70}\text{Se}$ , which is taken from reference [90].

	HFB-GCM	EXVAM	CHFB+LQRPA	SCCM	Experiment
$^{72}\text{Kr}$	0.313	0.272	0.590	0.725	0.491(7)
$^{70}\text{Kr}$	0.367	0.301	0.338	0.512	0.34(5)
$^{70}\text{Se}$	0.311	0.246	0.265		0.171(4)

**Table 5.6:** Experimentally obtained  $E(2_1^+) [keV]$  values compared to the predictions. Listed experimental values are obtained with the exception of  $^{70}\text{Se}$  [79].

	HFB-GCM	EXVAM	CHFB+LQRPA	SCCM	Experiment
$^{72}\text{Kr}$	746	658	542	395	710(1)
$^{70}\text{Kr}$	741	850	513	510	885(4)
$^{70}\text{Se}$	776	812	671		945(6)

All the calculations overestimate the collectivity for  $^{70}\text{Se}$  with low energy and a large  $B(E2)$  value. For  $^{70}\text{Kr}$ , all calculations predict a further increase in collectivity. This trend is confirmed by the presented experimental result, despite a large error in the  $B(E2)$  value. No agreement is, however, obtained for the  $2^+$  energy in  $^{70}\text{Kr}$  which is too low in all calculations.

### 5.4.2 Collectivity in the $A = 70$ Isobaric Triplet

The  $T = 1$  triplet at  $A = 70$  is important due to the anomalies described in section 1.1.2. Therefore, it attracted many attempts to explain this unusual behavior. The first experiment performed in order to measure the shape in this triplet was the study of  $^{70}\text{Se}$ . This was measured at REX-ISOLDE via Coulomb excitation and a prolate shape was reported for the ground state as a result of a large negative diagonal  $E2$  matrix element for the  $2_1^+$  state [6]. However, lifetime measurements gave different interpretation compared to the Coulomb excitation experiment, which indicated an oblate ground state for  $^{70}\text{Se}$  [8]. Due to the isospin symmetry, a similar shape is expected in the mirror nucleus  $^{70}\text{Kr}$ .

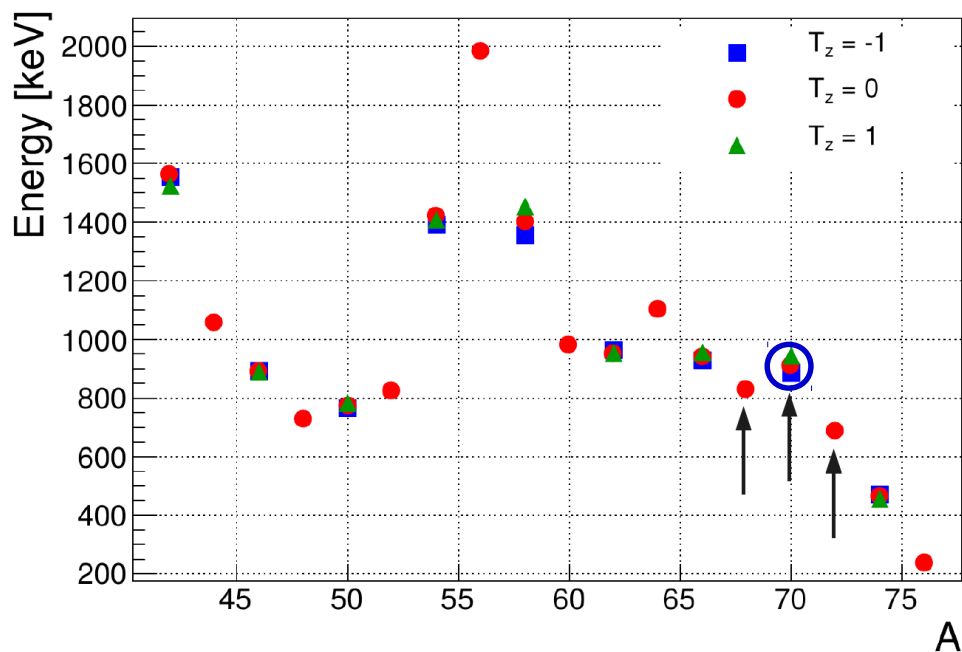
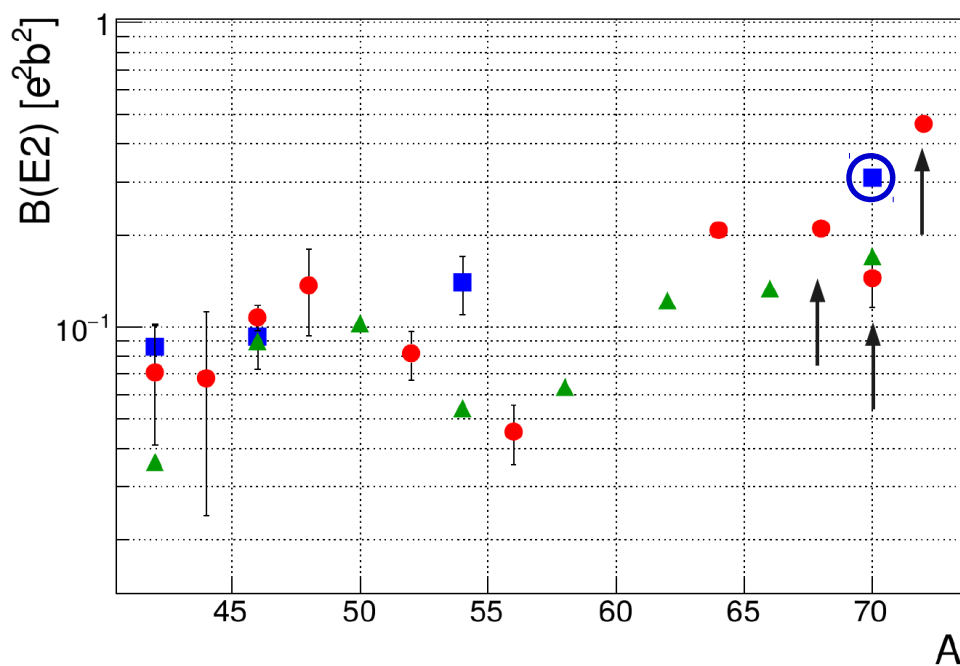
The other member of this triplet,  $^{70}\text{Br}$ , was also experimentally studied via lifetime measurements before the presented work. The deduced value for  $B(E2)\uparrow$  was found to be similar to  $^{70}\text{Se}$ , indicating similar collectivity. This result means that there is no shape change between these two nuclei [91]. In this thesis the value obtained for  $^{70}\text{Br}$  is in agreement with the previous measurement, confirming no change in the collectivity and the comparison is given in table 5.7.

The  $B(E2)$  value for the  $2_1^+ \rightarrow 0_1^+$  transition of the  $T_z = -1$  member of this triplet,  $^{70}\text{Kr}$ , was determined for the first time with this study. Despite a relatively large error, these result establishes a considerable increase in the collectivity of  $^{70}\text{Kr}$  as compared to the other members of the triplet. Additionally, the  $E(2_1^+)$  value of  $^{70}\text{Kr}$  is substantially different from the analogue states in  $^{70}\text{Br}$  and  $^{70}\text{Se}$ . The  $T_z = 0$  and  $T_z = 1$  members have a similar and higher energy for the  $2_1^+$  state while in the  $T_z = -1$  member this value decreases by more than  $50\text{ keV}$ .

**Table 5.7:** Experimentally obtained  $B(E2)\uparrow$  and  $E(2_1^+)$  values of the present work are compared to the literature [8, 91].

$B(E2)\uparrow$ [ $e^2b^2$ ]	$^{70}\text{Kr}$	$^{70}\text{Br}$	$^{70}\text{Se}$
$E(2_1^+)$ [ $\text{keV}$ ]	$(2_1^+)$	$(2_1^+)$	$(2_1^+)$
Present work	0.34(5)	0.141(31)	-
	885(4)	933(2)	-
References	-	0.145(21)	0.171(9)
	-	933(3)	944.5(5)

These values are listed in Table 5.7 and are compared with the literature. Figure 5.17 shows the experimentally measured  $2_1^+$  excitation energies and  $B(E2)\uparrow$  values for all of the  $N = Z$  nuclei  $T = 1$  triplets in the region, comparing the isobaric analogue states. The observation of a rapid variation in the  $2_1^+$  energy values and the collectivity, hence the increasing deformation between IAS, is a fingerprint of shape coexistence [92].

(a)  $2_1^+ \rightarrow 0_1^+$  transition energies(b)  $B(E2; 0_1^+ \rightarrow 2_1^+)$  values

**Figure 5.17:** Measured  $2_1^+$  state energies and deduced  $B(E2)\uparrow$  values for  $T=1$  triplets and  $N=Z$  nuclei [79, 31]. The values obtained from this work are indicated with arrows. The blue circle in the plots highlights the values for  $^{70}\text{Kr}$ , which was measured and calculated for the first time within this study.

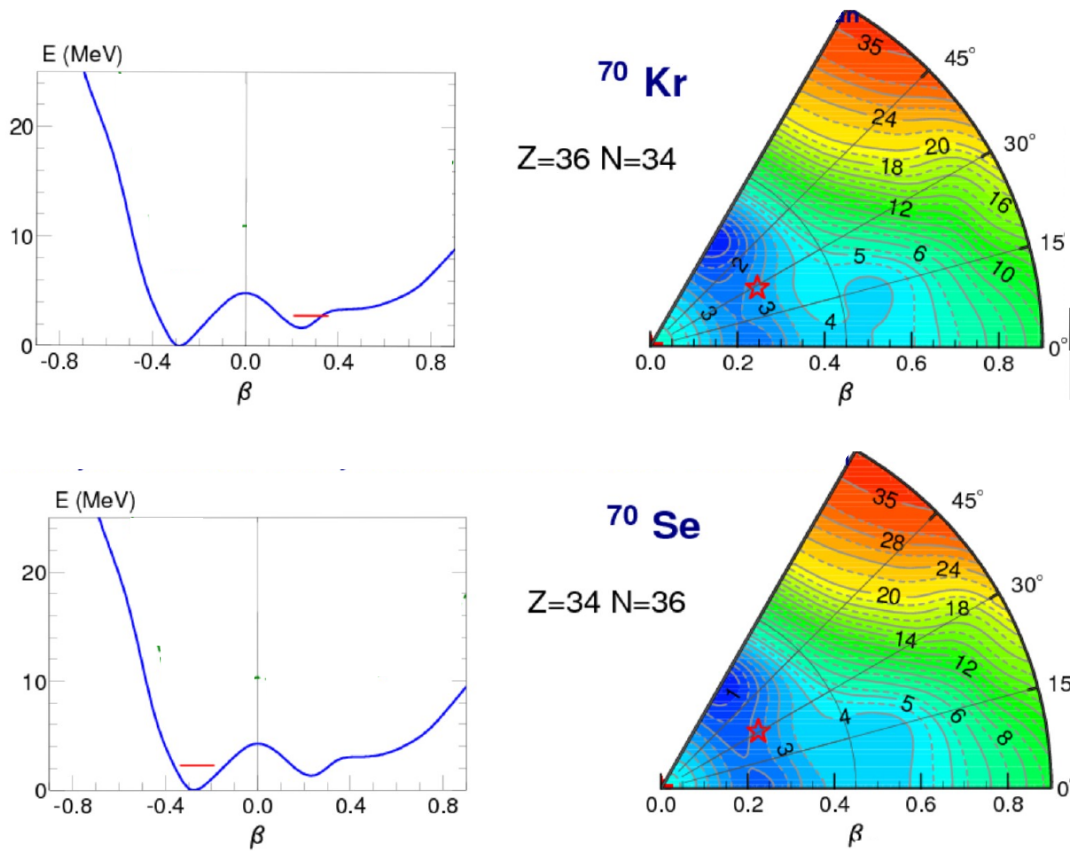


**Figure 5.18:** Potential energy surface (left) calculated with the HFB approach using the Gogny-D1S interaction. It illustrates the very similar features for the  $A=70$  mirror nuclei  $^{70}\text{Se}$  and  $^{70}\text{Kr}$  on the mean-field level [20, 93].

Due to these unique aspects, rapid shape changes and the mixing of different shapes, leads to a great challenge from a theoretical point of view when it comes to giving an adequate description of the region. As one example, the potential energy surface calculated with the HFB approach using the Gogny-D1S interaction, is shown in Figure 5.18 illustrating very similar features for  $^{70}\text{Kr}$  and its mirror,  $^{70}\text{Se}$ . On the left side of this figure, energy surface calculations are shown, indicating that oblate configurations are lower in energy. These pure mean-field calculations predict an oblate ground state deformation for both nuclei, which is extremely rare along the nuclear chart. The experimental and theoretical level schemes for  $^{70}\text{Kr}$  are shown in Figure 5.19 as obtained from several different theoretical models.

SCCM calculations suggest for  $^{70}\text{Se}$ , an oblate deformed ground state band and a less deformed and more prolate band on the top of the  $0_2^+$  state. A well deformed triaxial band is built on the top of the  $0_3^+$  state in  $^{70}\text{Se}$  with a  $\beta_2 \approx 0.55$  at  $\gamma = 20$  [94]. This method includes GCM with triaxial angular momentum projection of intrinsic states obtained with a particle number projection, using Gogny D1S parametrization.

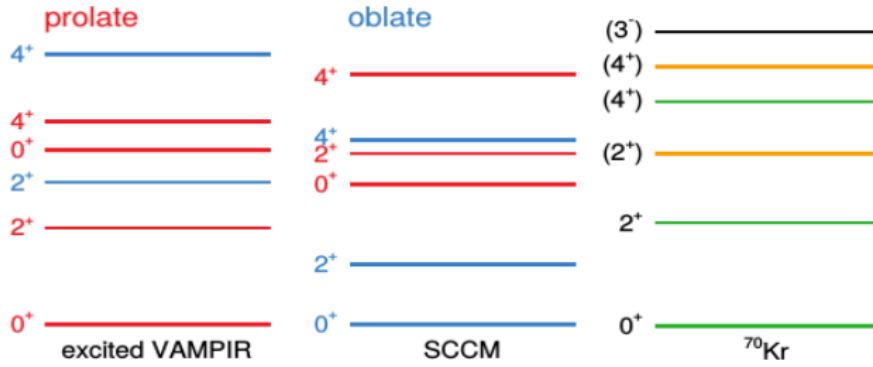


**Figure 5.19:** Level schemes for  $^{70}\text{Kr}$  predicted by different models compared to the experimentally measured values. Different colors indicate the different shapes that are expected to dominate. Red color shows the prolate deformation and the blue is the oblate deformation. For the  $^{70}\text{Kr}$  isotope, different bands are indicated in different colors but the type of the shape is not specified as it is not known experimentally.

Another theoretical study performed for this triplet was based on the beyond mean field complex excited VAMPIR model. Detailed information of the approach is given in reference [25]. This model predicts a strong mixing of prolate and oblate deformed configurations in the wave functions that is decreasing with increasing spin. For the ground state of  $^{70}\text{Se}$ , very high mixing is expected with a predominant oblate shape, while for  $^{70}\text{Kr}$ , mixing is dominant for the prolate contribution. For the  $T_z = 0$  member  $^{70}\text{Br}$ , the same amount of shape mixing as in  $^{70}\text{Kr}$  is expected with a slightly more prominent prolate ground shape. Moreover, the trend from the complex Excited VAMPIR predictions on mirror energy differences and triplet energy differences for the  $A = 70$  isovector triplet agrees with the experimentally observed distributions. Figure 5.20 represents the predictions and the measured values for MED and TED of the  $A = 70$  isovector triplet, together with the predictions from Shell Model calculations taking into account the isospin non-conserving nuclear forces (INC) [41]. This model, JUN45 + INC, shows even better agreement than the EXVAM model by reproducing the MED and TED values for the  $A = 70$  triplet. It suggests that the INC interaction enhances the MED and TED significantly and is responsible for the isospin symmetry breaking in the upper  $fp$  shell. The negative MED values are due to the spin-orbit contribution in  $A = 70$  mirror nuclei and are also attributed to the INC interaction together with the same mechanism leading to the anomalous CED between the isospin  $T = 1$  states in the odd-odd  $N = Z$  nucleus  $^{70}\text{Br}$  and the analogue states in its even-even partner  $^{70}\text{Se}$ . Negative TED values are due to the larger excitation energy of the odd-odd member with proton-neutron pairing compared to  $^{70}\text{Se}$  and  $^{70}\text{Kr}$ . Now that the experimental results are obtained for this member of the triplet, further investigations should be done with this theory comparing both results.

Another way of testing the isospin symmetry breaking is by extracting the isoscalar multipole matrix elements which is the part of the effective potential that does not distinguish the proton and neutron. As the protons are charged particles and sensitive to

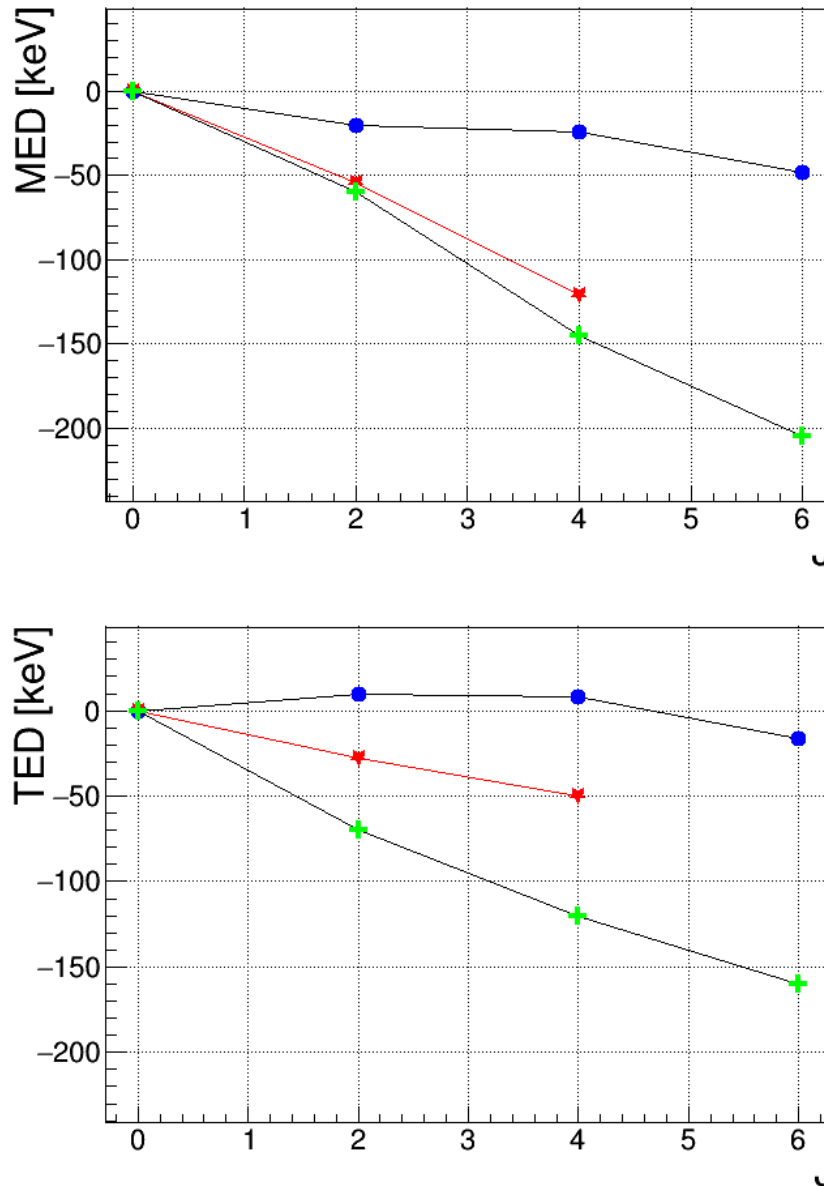


**Figure 5.20:** Comparison between the measured and predicted values is represented in this figure. The green crosses show the numbers from the JUN45+INC model, blue circles are for the complex EXVAM model and the red stars shows the experimentally measured values. MED and TED are represented for  $A = 70$  isobaric analogue states

the electromagnetic interaction, relative matrix element is directly related to the reduced electric quadrupole transition probability  $B(E2)$  values via Equation 2.45. Assuming the isospin conservation and including the measurements that we performed for the  $^{70}\text{Kr}$ , equation 2.48 can be used to examine the isospin symmetry purity of the mass system and compare the evolution from many aspects. This approach is well established for light nuclei. The comparison for the available data is given in Figure 5.21 including the  $A = 70$  triplet and the lighter nuclei region. The panel shows the isoscalar matrix element extracted from the measured  $B(E2)$  values by using the referred equations. One notices

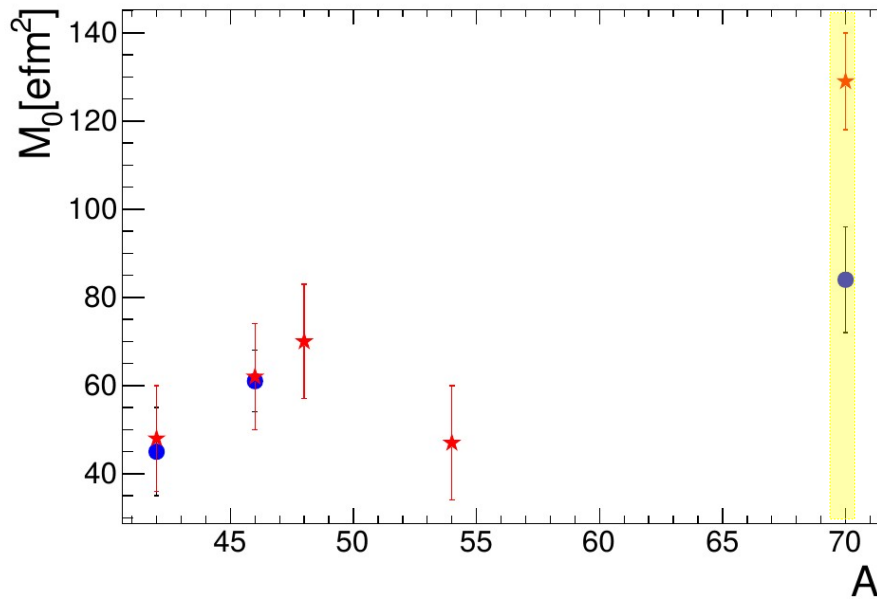


**Figure 5.21:** The panel shows the isoscalar matrix element extracted from the measured  $B(E2)$  values. The red stars indicate the  $T_z = \pm 1$  and blue dots shows  $T_z = 0$  isotopes. The yellow region contains the values obtained from the present work.

the very large difference in  $M_0$  values for the  $A=70$  case, indicating a large isospin symmetry break or a shape change between these mirror nuclei.

# 6

## Summary and Outlook

The electromagnetic excitation of the beam isotopes around  $A = 70$  sheds light on the collectivity for the  $2^+ \rightarrow 0^+$  transition in nuclei far from stability. By measuring the  $2^+$  states and corresponding  $B(E2)$  values, collectivity can be studied in a unique way. Within the work of this thesis, intermediate beam energy Coulomb and nuclear inelastic scattering has been used as a spectroscopic tool. In this framework, the inelastic scattering of  $^{72}\text{Kr}$ ,  $^{70}\text{Kr}$ ,  $^{70}\text{Br}$  and  $^{68}\text{Se}$  isotopes on  $^9\text{Be}$  and  $^{197}\text{Au}$  target at energy around 170 MeV/u has been studied. Production of these isotopes as a beam is possible at the Radioactive Isotope Beam Factory (RIBF) in RIKEN, where the experiments were performed. A  $^{78}\text{Kr}$  primary beam with an energy of 345 MeV/u was impinged on a  $^9\text{Be}$  target to produce the ions of interest as a secondary beam. The BigRIPS fragment separator was used in order to deliver the secondary beam isotopes,  $^{72}\text{Kr}$  and  $^{70}\text{Kr}$  to the secondary target for the inelastic scattering measurements. The reaction products were identified in the ZeroDegree Spectrometer employing the  $B\rho - \Delta E$ -TOF method and  $\gamma$ -rays emitted due to the de-excitation were measured in coincidence by an array of  $\gamma$ -ray detector DALI2 that was placed around the secondary target for highly efficient  $\gamma$ -ray detection. A beam tracking detectors were placed before and after the secondary reaction target in order to reconstruct the trajectory of the scattered particles. From the  $^{70}\text{Kr}$  beam cocktail,  $^{70}\text{Br}$  and  $^{68}\text{Se}$  were also used as a secondary beam, even though they were not centered in the spectrometer.

The experimental conditions were simulated to obtain the response functions of the transitions. Experimental results were then fitted to these response functions from the simulations and the interaction cross sections were determined for all the cases. Measured cross section values were used to determine the nuclear and Coulomb deformation lengths by using the ECIS-97 code. Global optical potentials and isotopes are introduced to the ECIS-97 code separately for each isotope considering the rotational model. For inelastic scattering on  $^9\text{Be}$  and  $^{197}\text{Au}$  targets, deformation lengths and the deformation parameters were determined. These parameters were then used to deduce the  $B(E2; 0_1^+ \rightarrow 2_1^+)$  transition probabilities. Results were compared to theoretical predictions.

The main goal of the experiment was to measure the first excited  $2^+$  state and deduce the  $B(E2; 0_1^+ \rightarrow 2_1^+)$  electromagnetic transition probability for the isotope  $^{70}\text{Kr}$  for the first

time. For the other isotopes, these values were measured before and during this study and verified by reproducing them in different experimental conditions. In addition, they were used in order to verify the accuracy of our measurement and the analysis for the  $^{70}\text{Kr}$  case. Finally, the  $B(E2; 0^+ \rightarrow 2_1^+)$  values of  $^{72}\text{Kr}$ ,  $^{70}\text{Kr}$ ,  $^{70}\text{Br}$  and  $^{68}\text{Se}$  were obtained. Results foresee a shape change for  $^{70}\text{Kr}$  due to the significant difference in electromagnetic decay properties.

The isotopes  $^{72}\text{Kr}$ ,  $^{70}\text{Br}$  and  $^{68}\text{Se}$  are the  $N=Z$  nuclei and have a great sensitivity to the effect of the proton-neutron correlations on the structure of the nuclei. Several studies were performed to measure the  $B(E2; 0^+ \rightarrow 2_1^+)$  values of even-even and odd-odd  $N=Z$  nuclei in the past along the nuclear chart. Figure 6.1 shows the  $2_1^+$  energies and  $B(E2)\uparrow$  values for these nuclei in  $A=70$  region. The left plot shows the  $B(E2)\uparrow$  and the right plot shows the  $E(2^+)$  values for  $^{64}\text{Ge}$ ,  $^{66}\text{As}$ ,  $^{68}\text{Se}$ ,  $^{70}\text{Br}$ ,  $^{72}\text{Kr}$ ,  $^{74}\text{Rb}$  and  $^{76}\text{Sr}$  isotopes, all  $N=Z$ . Systematic behavior of these two observables has been studied by Grodzins for a wide range of even-even nuclei and the general trend is explained as: increasing  $E(2^+)$  is accompanied by a decreasing transition strength  $B(E2)$  [95]. A rapid increase in  $B(E2)\uparrow$  values and decrease of  $2_1^+$  energies fits this Grodzins rule and due to the equation 1.1, indicates an increase in collectivity at  $A=72$ . The trend suggests rapid increase in

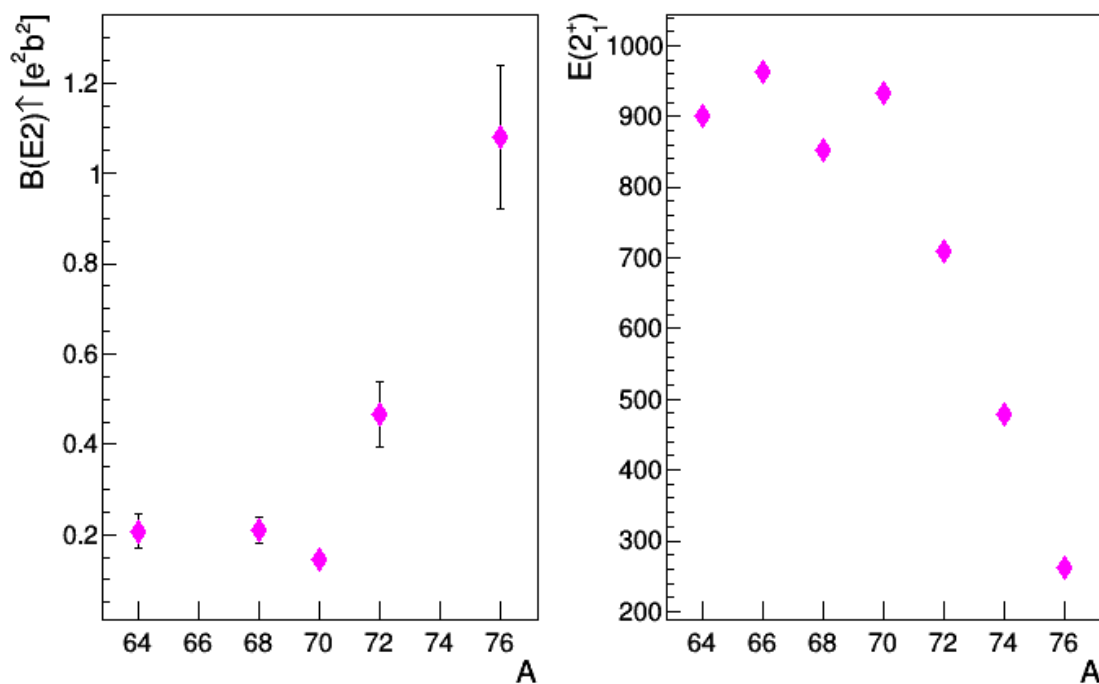


**Figure 6.1:**  $B(E2; 0^+ \rightarrow 2_1^+)$  values and  $E(2^+)$  energies for  $N=Z$  nuclei around mass 70 region are shown. Experimentally measured values are adopted from literature [79].

deformation from mass 70 to mass 72 and no significant difference is seen between  $^{68}\text{Se}$  and  $^{70}\text{Br}$  that could arise from the unpaired, single proton and neutron in the  $^{70}\text{Br}$ . In

fact, a relative decrease in collectivity is observed for the  $^{70}\text{Br}$  isotope. In the right plot,  $E(2^+)$  values show a decreasing trend that fits with the expectations according to the  $B(E2)\uparrow$  values since the excitation energy would decrease with the increasing deformation.

Due to the rapid shape changes and the expected strong mixing of oblate and prolate shapes, it is found to be an interesting territory to study the isospin breaking effects for  $T=1$  triplets. The  $^{70}\text{Se}$  and  $^{70}\text{Br}$  isotopes are the other two members of a triplet with  $^{70}\text{Kr}$ . By measuring the third member of this triplet we enabled the study of Mirror Energy Differences (MED) and Triple Energy Differences (TED) that can provide information about charge and isospin symmetry breaking. Negative tendency with the increasing spin was observed for both cases and experimental values were compared to the theoretical predictions. The isoscalar matrix element was determined and results showed largest isospin symmetry breaking among the tested isotopes up to date.

The fingerprint of shape coexistence, low lying  $0^+$  excited states is seen in all the Kr isotopes around this mass region. They form shape isomers expected to also exist in  $^{70}\text{Kr}$ . For future studies, these low-lying isomeric states can be measured using conversion electron spectroscopy. From this, clear assumptions can be drawn for shape coexistence and the systematics of low lying  $0^+$  states in the Kr isotopes, extending the information to the mass  $A=70$  region and within the triplet.



# A | Appendix

**Table A.1:** *Efficiencies of PPACs along the focal planes placed at BigRIPS and ZDS.*

PPAC BigRIPS	Efficiency [%]	PPAC BigRIPS	Efficiency [%]	PPAC BigRIPS	Efficiency [%]
F3/1A/X	0	F5/1A/X	91.6	F7/1A/X	96.5
F3/1A/Y	0	F5/1A/Y	94.1	F7/1A/Y	95.7
F3/1B/X	89.9	F5/1B/X	94.9	F7/1B/X	97.5
F3/1B/Y	93.3	F5/1B/Y	94.8	F7/1B/Y	99
F3/2A/X	92.3	F5/2A/X	83.8	F7/2A/X	97.1
F3/2A/Y	91.5	F5/2A/Y	86.9	F7/2A/Y	95.7
F3/2B/X	88.7	F5/2B/X	96.3	F7/2B/X	95.3
F3/2B/Y	89.4	F5/2B/Y	97.4	F7/2B/Y	94.5

PPAC ZDS	Efficiency [%]	PPAC ZDS	Efficiency [%]	PPAC ZDS	Efficiency [%]
F8/1A/X	99.2	F9/1A/X	99.3	F11/1A/X	99.8
F8/1A/Y	99.6	F9/1A/Y	99.4	F11/1A/Y	99.5
F8/1B/X	98.6	F9/1B/X	98.7	F11/1B/X	99.4
F8/1B/Y	99.4	F9/1B/Y	99.7	F11/1B/Y	99.7
F8/2A/X	99.1	F9/2A/X	99.7	F11/2A/X	99.6
F8/2A/Y	99.1	F9/2A/Y	100	F11/2A/Y	99.2
F8/2B/X	98.9	F9/2B/X	97.7	F11/2B/X	99.6
F8/2B/Y	99	F9/2B/Y	99.9	F11/2B/Y	99.3
F8/3A/X	99.8				
F8/3A/Y	99.9				
F8/3B/X	93.1				
F8/3B/Y	96.9				



# List of Figures

1.1	Systematics on Kr isotopes . . . . .	5
1.2	Potential Energy Surface diagrams of Kr isotopes . . . . .	6
1.3	CED plot for $^{70}\text{Br}$ and $^{70}\text{Se}$ . . . . .	7
2.1	Shell Model Diagram . . . . .	12
2.2	Nuclear shapes depending on the $\beta_2$ value. . . . .	13
2.3	The Nillson Diagram . . . . .	15
2.4	Excitation and de-excitation process . . . . .	19
2.5	A schematic view of Coulomb excitation . . . . .	20
2.6	Interference of Coulomb and Nuclear excitations . . . . .	22
3.1	Primary beam generation. . . . .	31
3.2	A schematic view of BigRIPS and ZeroDegree Spectrometers . . . . .	32
3.3	PPAC. . . . .	34
3.4	TEGIC . . . . .	35
3.5	Simulated energy spectrum of $^{72}\text{Kr}$ . . . . .	37
3.6	Schematic view of DALI2 . . . . .	38
3.7	Simulated energy spectrum for different energies. . . . .	43
3.8	Addback . . . . .	44
4.1	Schematic view of the Spectrometer with used apparatus. . . . .	46
4.2	TsumX spectrum with the applied gate. . . . .	47
4.3	Beam Profile at different focal planes . . . . .	48
4.4	Correlation between ToF and Z . . . . .	49
4.5	A/q position dependence at before and after the correction. . . . .	50
4.6	A/q projection for Z = 36 isotopes. . . . .	51
4.7	The gain drift in Z and A/q. . . . .	52
4.8	PID plots for Coulomb excitations. . . . .	53
4.9	PID plots for inelastic reactions. . . . .	54
4.10	A schematic view of the scattering angle reconstruction. . . . .	56
4.11	Scattering angle Resolution . . . . .	57
4.12	Convolution of the nuclear and electromagnetic cross-sections with experimental resolution . . . . .	58

4.13	Transmission comparision . . . . .	59
4.14	Position Dependent Transmission comparision . . . . .	60
4.15	The angular acceptance of ZeroDegree Spectrometer . . . . .	61
4.16	Simulated $\beta$ distributions . . . . .	63
4.17	DALI2 array after the calibration . . . . .	64
4.18	Energy deviation among the crytals . . . . .	65
4.19	The dependence of the resolution on the energy. . . . .	66
4.20	Fitted energy spectra from different sources. . . . .	67
4.21	Source runs and the background . . . . .	68
4.22	Decay curve of the background . . . . .	69
4.23	Gamma-Gamma technique for FEP . . . . .	70
4.24	Efficiency Comparision . . . . .	70
4.25	Comparison of Doppler corrected and not corrected spectrum. . . . .	71
4.27	Time calibration of 186 NaI(Tl) detectors. . . . .	73
4.28	Energy - Time correlation, showing the selected and rejected events. . . . .	73
4.29	Time projection of the selected time window for DALI2. . . . .	74
5.1	$\gamma$ -ray energy spectrum of $^{72}\text{Kr}$ . . . . .	77
5.2	$^{72}\text{Kr}$ isotopic chain . . . . .	78
5.3	$\gamma$ - $\gamma$ matrix of the $^{72}\text{Kr}$ isotope. . . . .	79
5.4	Level Scheme of $^{72}\text{Kr}$ isotope . . . . .	79
5.5	$\gamma$ -ray energy spectrum of the $^{70}\text{Kr}$ . . . . .	81
5.6	Level Scheme of $^{70}\text{Kr}$ isotope . . . . .	82
5.7	The $\gamma$ -ray energy spectra of $^{70}\text{Br}$ . . . . .	83
5.8	$\gamma$ - $\gamma$ coincidence matrix for the $^{70}\text{Br}$ isotope. . . . .	84
5.9	Level Scheme of the $^{70}\text{Br}$ isotope . . . . .	84
5.10	The Doppler shift corrected $\gamma$ -ray energy spectra of the $^{68}\text{Se}$ . . . . .	85
5.11	$\gamma$ - $\gamma$ coincidence matrix of the $^{68}\text{Se}$ isotope. . . . .	86
5.12	Level Scheme of $^{68}\text{Se}$ isotope . . . . .	86
5.13	Optical potential fits . . . . .	89
5.14	Nuclear Deformation length . . . . .	90
5.15	B(E2) $\uparrow$ and E(2 $^+$ ) energies for diffrent Kr isotopes . . . . .	92
5.16	Comparison of the B(E2) $\uparrow$ values from this work with the predictions and the literarure. . . . .	93
5.17	Isobaric Analogue States . . . . .	96
5.18	PES for the A = 70 mirror nuclei $^{70}\text{Se}$ and $^{70}\text{Kr}$ . . . . .	97
5.19	Predicted and measured level construction for $^{70}\text{Kr}$ isotope. . . . .	98
5.20	TED and MED comparision for predicted and measured values. . . . .	99
5.21	Isoscaler multipole element . . . . .	100
6.1	B(E2) evolution in N=Z nuclei around mass 70 region . . . . .	102

# List of Tables

1.1	The measured spectroscopic quadrupole moments ( $Q_s$ ) and the $B(E2)\uparrow$ values for $^{72,74,76,78}\text{Kr}$ . . . . .	4
2.1	The existing forces in nature with their effective ranges and interaction types. . . . .	9
3.1	Type of the scintillators used for DALI2. . . . .	38
3.2	Settings of the performed experiments. . . . .	40
3.3	List of targets used in different settings. . . . .	40
4.1	The $A/q$ and $Z$ resolutions for the particle identification of $^{70}\text{Kr}$ . . . . .	53
4.2	The number of selected isotopes of an incoming beam on the secondary target $N_{BR}$ and the number of outgoing particles $N_{ZD}$ . . . . .	55
4.3	The measured angular spread with target $\sigma_S$ are obtained by ATIMA calculation while the $\sigma_R$ values are the scattering angle resolution with the empty target case. . . . .	58
4.4	Total transmission for selected isotopes in different settings, including all contributions to losses along the spectrometer. . . . .	61
4.5	The energy of corresponding isotopes in front of the target and obtained $\beta$ values. . . . .	63
4.6	Deviations between the calibrated energies and reference energies measured with the DALI2 $\gamma$ -ray detection array. . . . .	65
5.1	Cross-section values. . . . .	88
5.2	The obtained deformation lengths. . . . .	90
5.3	Calculated $R_c$ and $\beta_c$ values for the interested states of studied isotopes. . . . .	91
5.4	Extracted $B(E2)\uparrow$ values for $^{70}\text{Kr}$ , $^{68}\text{Se}$ , $^{70}\text{Br}$ and $^{72}\text{Kr}$ isotopes. . . . .	91
5.5	Experimentally obtained $B(E2)\uparrow$ values compared to predictions. . . . .	94
5.6	Experimentally obtained $E(2_1^+)$ values compared to the predictions. . . . .	94
5.7	Experimentally obtained $B(E2)\uparrow$ and $E(2_1^+)$ values of the present work are compared to the literature [8, 91]. . . . .	95
A.1	Efficiencies of PPACs along the focal planes placed at BigRIPS and ZDS. . . . .	105



# References

- [1] RIKEN. RI Beam Factory – basic science RIKEN accelerator research facility. <http://www.rarf.riken.go.jp/ribf/doc/ribf94e/>.
- [2] S. Takeuchi, T. Motobayashi, Y. Togano, M. Matsushita, N. Aoi, K. Demichi, H. Hasegawa, and H. Murakami. DALI2: A NaI(Tl) detector array for measurements of  $\gamma$  rays from fast nuclei. *Nuclear Instruments and Methods in Physics Research*, A763:596–603, 2014.
- [3] J. Raynal. ECIS-97. *Unpublished*, 1997.
- [4] M Hasegawa, K Kaneko, T Mizusaki, and Y Sun. Phase transition in exotic nuclei along the  $n=z$  line. *Physics Letters B*, 656(1):51–55, 2007.
- [5] Gade, A and Bazin, D and Becerril, A and Campbell, CM and Cook, JM and Dean, DJ and Dinca, D-C and Glasmacher, T and Hitt, GW and Howard, ME and others. Quadrupole Deformation of the Self-Conjugate Nucleus  $^{72}\text{Kr}$ . *Physical Review Letters*, 95:022502, 2005. [Erratum: *Physical Review Letters*96,189901(2006)].
- [6] A. M. Hurst, P. A. R. Butler, N. Warr, D. Weisshaar, and M. et al. Zielińska. Measurement of the sign of the spectroscopic quadrupole moment for the  $2_1^+$  state in  $^{70}\text{Se}$ : No evidence for oblate shape. *Physical Review Letters*, 98:072501, Feb 2007.
- [7] H. Iwasaki, A. Lemasson, C. Morse, K. Dewald, and et Wimmer K. Evolution of collectivity in  $^{72}\text{Kr}$ : Evidence for rapid shape transition. *Physical Review Letters*, 112:142502, Apr 2014.
- [8] J. Ljungvall, A. Gørgen, M. Girod, J. P. Delaroche, A. Dewald, C. Dossat, E. Farnea, W. Korten, B. Melon, R. Menegazzo, A. Obertelli, R. Orlandi, P. Petkov, T. Pissulla, S. Siem, R. P. Singh, J. Srebrny, Ch. Theisen, C. A. Ur, J. J. Valiente-Dobón, K. O. Zell, and M. Zielińska. Shape coexistence in light Se isotopes: Evidence for oblate shapes. *Physical Review Letters*, 100:102502, Mar 2008.
- [9] B Castel, DJ Rowe, and L Zamick. Why are deformed nuclei prolate? *Physics Letters B*, 236(2):121–124, 1990.
- [10] A. Petrovici, K. W. Schmid, and Amand Faessler. Microscopic aspects of shape coexistence in Kr-72 and Kr-74. *Nuclear Physics*, A665:333–350, 2000.
- [11] E Bouchez, I Matea, W Korten, F Becker, B Blank, C Borcea, A Buta, A Emsallem, G De France, J Genevey, et al. New Shape Isomer in the Self-Conjugate Nucleus Kr-72. *Physical Review Letters*, 90:082502, 2003.

- [12] RB Piercey, JH Hamilton, R Soundranayagam, AV Ramayya, CF Maguire, X-J Sun, ZZ Zhao, RL Robinson, HJ Kim, S Frauendorf, et al. Evidence for Deformed Ground States in Light Kr Isotopes. *Physical Review Letters*, 47:1514–1517, 1981.
- [13] Hinohara Nobuo et al. Sato, Koichi. Shape mixing dynamics in the low-lying states of proton-rich Kr isotopes. *Nuclear Physics A*, 849(1):53–71, 2011.
- [14] E Clément, A Gørgen, W Korten, E Bouchez, A Chatillon, J-P Delaroche, M Girod, H Goutte, A Hürstel, Y Le Coz, et al. Shape coexistence in neutron-deficient krypton isotopes. *Physical Review*, C75:054313, 2007.
- [15] A Gørgen, E Clément, A Chatillon, A Dewald, W Korten, Y Le Coz, N Mărginean, B Melon, R Menegazzo, O Möller, et al. Lifetime measurement in  $^{74}\text{Kr}$  and  $^{76}\text{Kr}$ . *The European Physical Journal A-Hadrons and Nuclei*, 26(2):153–157, 2005.
- [16] E Clément, G De France, JM Casandjian, A Gørgen, W Korten, E Bouchez, A Chatillon, A Huerstel, Y Le Coz, A Obertelli, et al. Experimental measurement of the deformation through the electromagnetic probe: shape coexistence in exotic Kr and Sr isotopes. *International Journal of Modern Physics E*, 20(02):415–421, 2011.
- [17] A. Goergen. Lecture notes. <https://web-docs.gsi.de/~wolle/TELEKOLLEG/KERN/PDF/Goergen/Goergen-Chester4.pdf>.
- [18] Peter Moller, Arnold J. Sierk, Ragnar Bengtsson, Hiroyuki Sagawa, and Takatoshi Ichikawa. Global Calculation of Nuclear Shape Isomers. *Physical Review Letters*, 103:212501, 2009.
- [19] Tomas R. Rodriguez. Structure of Krypton isotopes calculated with symmetry conserving configuration mixing methods. *Physical Review*, C90(3):034306, 2014.
- [20] M. Girod, J. P. Delaroche, A. Gorgen, and A. Obertelli. The role of triaxiality for the coexistence and evolution of shapes in light krypton isotopes. *Physics Letters*, B676:39–43, 2009.
- [21] A Petrovici, KW Schmid, and Amand Faessler. Microscopic description of the mirror nuclei  $^{70}\text{Se}$  and  $^{70}\text{Kr}$ . *Nuclear Physics A*, 728(3-4):396–414, 2003.
- [22] BS Nara Singh, AN Steer, DG Jenkins, R Wadsworth, MA Bentley, PJ Davies, R Glover, NS Pattabiraman, CJ Lister, T Grahn, et al. Coulomb shifts and shape changes in the mass 70 region. *Physical Review*, C75(6):061301, 2007.
- [23] G De Angelis, T Martinez, A Gadea, N Marginean, E Farnea, E Maglione, S Lenzi, W Gelletly, CA Ur, DR Napoli, et al. Coulomb energy differences between isobaric analogue states in  $^{70}\text{Br}$  and  $^{70}\text{Se}$ . *The European Physical Journal A-Hadrons and Nuclei*, 12(1):51–55, 2001.
- [24] K. Kaneko, T. Mizusaki, Y. Sun, S. Tazaki, and G. de Angelis. Coulomb energy difference as a probe of isospin-symmetry breaking in the upper  $fp$ -shell nuclei. *Physical Review Letters*, 109:092504, Aug 2012.
- [25] A. Petrovici. Isospin-symmetry breaking and shape coexistence in  $A=70$  analogs. *Journal of Physics: Conference Series*, 724(1):012038, 2016.
- [26] Peter Möller and J Rayford Nix. Atomic masses and nuclear ground-state deformations calculated with a new macroscopic-microscopic model. *Atomic Data and Nuclear Data Tables*, 26(2):165–196, 1981.
- [27] Aage Bohr and Ben R Mottelson. *Nuclear Structure:(In 2 Volumes) Volume I: Single-Particle Motion Volume II: Nuclear Deformations*. World Scientific, 1998.

- [28] Kenneth S Krane and David Halliday. *Introductory nuclear physics*, volume 465. Wiley New York, 1988.
- [29] Apolodor Aristotel Raduta. Pear shaped nuclei. In *Nuclear Structure with Coherent States*, pages 235–253. Springer, 2015.
- [30] Liam Paul Gaffney, Peter A Butler, Marcus Scheck, Adam B Hayes, Frederik Wewander, Michael Albers, Beyhan Bastin, Christopher Bauer, Andrey Blazhev, Sabine Bönig, et al. Studies of pear-shaped nuclei using accelerated radioactive beams. *Nature*, 497(7448):199–204, 2013.
- [31] Wimmer K. Shape coexistence at  $n=z$  spectroscopy of the  $t_z = -1$  nucleus  $^{70}\text{Kr}$ . *International Nuclear Physics Conference*, 2016.
- [32] Aurel Bulgac. Hartree–fock–bogoliubov approximation for finite systems. *arXiv preprint nucl-th/9907088*, 1999.
- [33] M Anguiano, AM Lallena, V De Donno, et al. A study of self-consistent Hartree–Fock plus Bardeen–Cooper–Schrieffer calculations with finite-range interactions. *Journal of Physics G: Nuclear and Particle Physics*, 41(2):025102, 2014.
- [34] J Rikowska Stone and P-G Reinhard. The skyrme interaction in finite nuclei and nuclear matter. *Progress in Particle and Nuclear Physics*, 58(2):587–657, 2007.
- [35] F Chappert, N Pillet, M Girod, and J-F Berger. Gogny force with a finite-range density dependence. *Physical Review*, C91(3):034312, 2015.
- [36] W. Heisenberg. Über den Bau der Atomkerne. I. *Zeitschrift für Physik*, 77:1–11, January 1932.
- [37] R. Machleidt and H. Muther. Charge Symmetry Breaking of the nucleon–nucleon Interaction:  $\rho$ - $\omega$  Mixing Versus nucleon Mass Splitting. *Physical Review*, C63:034005, 2001.
- [38] G. H. Bordbar. Breaking of charge independence of nucleon nucleon interaction and bulk properties of nuclear matter. *International Journal of Modern Physics*, A18:3629–3636, 2003.
- [39] Aron M. Bernstein, V. R. Brown, and V. A. Madsen. Isospin Decomposition of Nuclear Multipole Matrix Elements from gamma Decay Rates of Mirror Transitions: Test of Values Obtained with Hadronic Probes. *Physical Review Letters*, 42:425–428, 1979.
- [40] S. M. Lenzi and R. Lau. A systematic study of mirror and triplet energy differences. *Journal of Physics: Conference Series*, 580(1):012028, 2015.
- [41] K. Kaneko, Y. Sun, T. Mizusaki, and S. Tazaki. Isospin nonconserving interaction in the  $T = 1$  analogue states of the mass-70 region. *Physical Review*, C89(3):031302, 2014.
- [42] H. J Wollersheim, D. Appelbe, A Banu, R Bassini, T Beck, Frank Becker, P Bednarczyk, K-H Behr, MA Bentley, G Benzoni, et al. Rare isotopes investigation at gsi (rising) using gamma-ray spectroscopy at relativistic energies. *Nuclear Instruments and Methods in Physics Research*, A537(3):637–657, 2005.
- [43] ANF Aleixo and CA Bertulani. Coulomb excitation in intermediate-energy collisions. *Nuclear Physics A*, 505(2):448–470, 1989.
- [44] Aage Winther and Kurt Alder. Relativistic coulomb excitation. *Nuclear Physics A*, 319(3):518–532, 1979.

- [45] R Huby and JR Mines. Distorted-wave born approximation for stripping to virtual levels. *Reviews of Modern Physics*, 37(3):406, 1965.
- [46] E Rost. Coupled-channel calculations for nuclear bound states. *Physical Review*, 154(4):994, 1967.
- [47] CA Bertulani, G Baur, and MS Hussein. Two-neutron removal cross sections of  $^{11}\text{Li}$  projectiles. *Nuclear Physics A*, 526(3-4):751–761, 1991.
- [48] Aage Bohr and Ben R Mottelson. Nuclear structure, vol. II, 1975.
- [49] AM Bernstein, VR Brown, and VA Madsen. Neutron and proton transition matrix elements and inelastic hadron scattering. *Physics Letters B*, 103(4-5):255–258, 1981.
- [50] Reinhard Stock. *Encyclopedia of nuclear physics and its applications*. John Wiley & Sons, 2013.
- [51] HL Ravn. Radioactive ion-beam projects based on the two-accelerator or isol principle. *PHILOSOPHICAL TRANSACTIONS-ROYAL SOCIETY OF LONDON SERIES A MATHEMATICAL PHYSICAL AND ENGINEERING SCIENCES*, pages 1955–1984, 1998.
- [52] Georg Bollen, Bjorn Jonson, H L Ravn, and Manfred Deicher. Physics at ISOLDE. page Transparencies ; 1 DVD video ; 1 VHS video, Geneva, 1999. CERN, CERN. CERN, Geneva, 8 - 12 Mar 1999.
- [53] S. Gales. SPIRAL2 at GANIL: Next Generation of ISOL Facility for Intense Secondary Radioactive Ion Beams. *Nuclear Physics*, A834:717c–723c, 2010.
- [54] Giacomo de Angelis and Gianni Fiorentini. The Legnaro National Laboratories and the SPES facility: nuclear structure and reactions today and tomorrow. *Physica Scripta*, 91(11):113001, 2016.
- [55] M Trinczek, F Ames, R Baartman, PG Bricault, M Dombisky, K Jayamanna, J Lassen, RE Laxdal, M Marchetto, L Merminga, et al. Beam Delivery and Future Initiatives at the ISAC Radioactive Ion Beam Facility. In *Particle accelerator. Proceedings, 23rd Conference, PAC'09, Vancouver, Canada, May 4-8, 2009*, page FR5REP124, 2010.
- [56] A Fijałkowska, M Karny, KP Rykaczewski, M Wolińska-Cichočka, R Grzywacz, CJ Gross, JW Johnson, BC Rasco, EF Zganjar, DW Stracener, et al. First Results from the Modular Total Absorption Spectrometer at the HRIBF. *Acta Phys. Polon.*, B45(2):545, 2014.
- [57] Sam M. Austin and Lou Anna K. Simon. *Up from Nothing: The Michigan State University Cyclotron Laboratory*. Michigan State University Press, 2015.
- [58] Hans Geissel, P Armbruster, K Hetal Behr, A Brünle, K Burkard, M Chen, H Folger, B Franczak, H Keller, O Klepper, et al. The GSI projectile fragment separator (FRS): A Versatile magnetic system for relativistic heavy ions. *Nuclear Instruments and Methods in Physics Research*, B70:286–297, 1992.
- [59] JP Dufour, R Del Moral, H Emmermann, F Hubert, D Jean, C Poinot, MS Pravikoff, Agnès Fleury, H Delagrangé, and K-H Schmidt. Projectile fragments isotopic separation: Application to the lise spectrometer at ganil. *Nuclear Instruments and Methods in Physics Research*, A248(2):267–281, 1986.
- [60] Toshiyuki Kubo, Daisuke Kameda, Hiroshi Suzuki, Naoki Fukuda, Hiroyuki Takeda, Yoshiyuki Yanagisawa, Masao Ohtake, Kensuke Kusaka, Koichi Yoshida, Naohito Inabe, et al. BigRIPS separator and ZeroDegree spectrometer at RIKEN RI beam factory. *PTEP*, 2012:03C003, 2012.

- [61] H Okuno, N Fukunishi, and O Kamigaito. Progress of RIBF accelerators. *Progress of Theoretical and Experimental Physics*, 2012(1):03C002, 2012.
- [62] A Goto, H Okuno, J Ohnishi, N Fukunishi, T Mitsumoto, S Fujishima, T Tominaka, K Ikegami, Y Miyazawa, Y Yano, et al. Progress on the sector magnets for the RIKEN SRC. In *AIP Conference Proceedings*, volume 600, pages 319–423. AIP, 2001.
- [63] RIBF heavy-ion acceleration system. <http://www.nishina.riken.jp/RIBF/accelerator/concept.html>.
- [64] N Kobayashi, T Nakamura, Jeffrey Allan Tostevin, Y Kondo, N Aoi, H Baba, S Deguchi, J Gibelin, M Ishihara, Y Kawada, et al. One-and two-neutron removal reactions from the most neutron-rich carbon isotopes. *Physical Review*, C86(5):054604, 2012.
- [65] H. Kumagai, T. Ohnishi, N. Fukuda, H. Takeda, D. Kameda, N. Inabe, K. Yoshida, and T. Kubo. Development of Parallel Plate Avalanche Counter (PPAC) for BigRIPS fragment separator. *Nuclear Instruments and Methods in Physics Research*, B317:717–727, 2013.
- [66] R. K Oyama Et Al K. Kimura, T. Zumikawa. High-rate particle identification of high-energy heavy ions using a tilted electrode gas ionization chamber. . *Nuclear Instruments and Methods in Physics Research*, A538:608–614, 2005.
- [67] H. J. Wollersheim. Lecture notes. <https://web-docs.gsi.de/~wolle/TELEKOLLEG/KERN/vorlesungen.html>.
- [68] S Akkoyun, Alejandro Algora, B Alikhani, F Ameil, G De Angelis, L Arnold, A Astier, Ayşe Ataç, Y Aubert, C Aufranc, et al. Agata - advanced gamma tracking array. *Nuclear Instruments and Methods in Physics Research*, A668:26–58, 2012.
- [69] I-Yang Lee. Gamma-ray energy tracking array: Gretina. *Journal of Physics: Conference Series*, 420(1):012156, 2013.
- [70] D Weisshaar, A Gade, T Glasmacher, GF Grinyer, D Bazin, P Adrich, T Baugher, JM Cook, C Aa Diget, S McDaniel, et al. Caesar a high-efficiency CsI (Na) scintillator array for in-beam  $\gamma$ -ray spectroscopy with fast rare-isotope beams. *Nuclear Instruments and Methods in Physics Research*, A624(3):615–623, 2010.
- [71] C Ghosh, V Nanal, RG Pillay, KV Anoop, N Dokania, Sanjoy Pal, MS Pose, G Mishra, PC Rout, Suresh Kumar, et al. *Journal of Instrumentation*, 11(05):P05023, 2016.
- [72] S. Agostinelli and J. Allison et al. Geant4 simulation toolkit. *Nuclear Instruments and Methods in Physics Research*, A506(3):250 – 303, 2003.
- [73] P.Doornenbal. Manual of a GEANT4 Simulation Code for Gamma Ray Detectors used in the RIKEN-RIBF Facility. 2011.
- [74] P. Malzacher J. Kunzendorf H. Weick H. Geissel, C. Scheidenberger. ATIMA.
- [75] N Fukuda, T Kubo, T Ohnishi, N Inabe, H Takeda, D Kameda, and H Suzuki. Identification and separation of radioactive isotope beams by the bigrips separator at the RIKEN RI Beam Factory. *Nuclear Instruments and Methods in Physics Research*, B317:323–332, 2013.
- [76] S. Purushothaman et. al. Hyper-EMG: A new probability distribution function composed of Exponentially Modified Gaussian distributions to analyze asymmetric peak shapes in high-resolution time-of-flight mass spectrometry. *International Journal of Mass Spectrometry*, Submitted.

- [77] D. C. Radford, J. R. Southon, and A. R. Poletti. Lifetime measurements in  $^{41}\text{Ar}$  and  $^{41}\text{K}$ . *Nuclear Physics A*, 303(1):134–144, 1978.
- [78] NS Kelsall, R Wadsworth, AN Wilson, P Fallon, AO Macchiavelli, RM Clark, DG Sarantites, D Seweryniak, CE Svensson, SM Vincent, et al. Consequences of neutron-proton pairing correlations for the rotational motion of the  $N=Z$  nucleus  $^{72}\text{Kr}$ . *Physical Review*, C64(2):024309, 2001.
- [79] National Nuclear Data Center, Brookhaven National Laboratory. <http://www.nndc.bnl.gov/ensdf>.
- [80] J Heese, KP Lieb, L Lühmann, F Raether, B Wörmann, D Alber, H Grawe, J Eberth, and T Mylaeus. Lifetime measurements in  $^{70}\text{Se}$  and  $^{72}\text{Se}$ . *Zeitschrift für Physik A Hadrons and Nuclei*, 325(1):45–53, 1986.
- [81] G Rainovski, H Schnare, R Schwengner, C Plettner, L Käubler, F Dönau, Ingemar Ragnarsson, J Eberth, T Steinhardt, O Thelen, et al. Shape coexistence at high spin in the  $N=Z+2$  nucleus  $^{70}\text{Se}$ . *Journal of Physics G: Nuclear and Particle Physics*, 28(10):2617, 2002.
- [82] R Wadsworth, LP Ekstrom, GD Jones, F Kearns, TP Morrison, PJ Twin, and NJ Ward. Gamma-ray studies on the neutron-deficient isotope  $^{70}\text{Se}$ . *Journal of Physics G: Nuclear Physics*, 6(11):1403, 1980.
- [83] G de Angelis, T Martinez, and A Gadea. Coulomb energy differences between isobaric analogue states in  $^{70}\text{Br}$  and  $^{70}\text{Se}$ . identification of excited states of the  $t_z = 0$  nucleus  $^{70}\text{Br}$ . *European Physical Journal*, A12(1):51–55, 2001.
- [84] G Gürdal and EA McCutchan. Nuclear data sheets for  $A = 70$ . *Nuclear Data Sheets*, 136:1–162, 2016.
- [85] DG Jenkins, NS Kelsall, CJ Lister, DP Balamuth, MP Carpenter, TA Sienko, SM Fischer, RM Clark, P Fallon, A Görden, et al.  $T=0$  and  $T=1$  states in the odd-odd  $N=Z$  nucleus,  $^{70}\text{Br}$ . *Physical Review*, C65(6):064307, 2002.
- [86] SM Fischer, DP Balamuth, PA Hausladen, CJ Lister, MP Carpenter, D Seweryniak, and J Schwartz. Evidence for collective oblate rotation in  $N = Z$   $^{68}\text{Se}$ . *Physical review letters*, 84(18):4064, 2000.
- [87] SM Fischer, CJ Lister, and DP Balamuth. Unravelling the band crossings in  $^{68}\text{Se}$  and  $^{72}\text{Kr}$ : The quest for  $T = 0$  pairing. *Physical Review*, C67(6):064318, 2003.
- [88] T Furumoto, W Horiuchi, M Takashina, Y Yamamoto, and Y Sakuragi. Global optical potential for nucleus-nucleus systems from 50 MeV/u to 400 MeV/u. *Physical Review*, C85(4):044607, 2012.
- [89] M. Bender, P. Bonche, and P.-H. Heenen. Shape coexistence in neutron-deficient Kr isotopes: Constraints on the single-particle spectrum of self-consistent mean-field models from collective excitations. *Physical Review*, C74:024312, Aug 2006.
- [90] S Raman, CW Nestor, and P Tikkanen. Transition probability from the ground to the first-excited  $2^+$  state of even–even nuclides. *Atomic Data and Nuclear Data Tables*, 78(1):1–128, 2001.
- [91] AJ Nichols, R Wadsworth, H Iwasaki, Kaoru Kaneko, A Lemasson, G De Angelis, VM Bader, T Baugher, Dominique Bazin, MA Bentley, et al. Collectivity in  $A \approx 70$  nuclei studied via lifetime measurements in  $^{70}\text{Br}$  and  $^{68,70}\text{Se}$ . *Physics Letters*, B733:52–57, 2014.

- 
- [92] Kris Heyde and John L Wood. Shape coexistence in atomic nuclei. *Reviews of Modern Physics*, 83(4):1467, 2011.
- [93] J. P. Delaroche. CEA - DAM Ile-de-France, France.
- [94] T. Rodrigez. Universidad Autonoma de Madrid, Departamento de Fisica Teorica, Spain. *Privat Communication*.
- [95] L Grodzins. The uniform behaviour of electric quadrupole transition probabilities from first  $2^+$  states in even-even nuclei. *Physics Letters*, 2(2):88–91, 1962.